

Synthesis and Applications  
Of Titania Nanotubes:  
Drug Delivery and Ionomer Composites

HARSHA PRABHAKAR KULKARNI

A dissertation submitted to the faculty of the University of North Carolina at Chapel Hill in  
partial fulfillment of the requirements for the degree of Doctor of Philosophy in the  
Curriculum in Applied and Materials Sciences

Chapel Hill  
2008

Approved by  
Advisor: Professor Yue Wu

Reader: Professor Rihe Liu

Reader: Professor Wenbin Lin

Reader: Professor Horst Kessemeier

Reader: Professor Lu Chang Qin

Reader: Professor Alfred Kleinhammes

© 2008  
HARSHA KULKARNI  
**ALL RIGHTS RESERVED**

## ABSTRACT

### “Synthesis and Applications of Titania Nanotubes: Drug Delivery and Ionomer Composites”

(Under the direction of Professor Yue Wu)

In this dissertation, the potential of a tubular form of titania (titanium dioxide) has been explored for two diverse applications, in the field of targeted drug delivery for medical applications and in the field of composite materials for structural applications.

We introduce the tubular form of titania, a material well known for its catalytic properties. The tubes are synthesized by hydrothermal procedure and are nanometers in dimension, with an inside diameter of 5-6 nm, outside diameter of 10-12, and an aspect ratio of ~100:1 (l:d), structures both chemically and thermally stable.

Biocompatible titania nanotubes with large catalytic surface area are used as vehicles for carrying Doxorubicin, an anticancer chemotherapeutic drug, to explore its potential in targeted drug delivery. Optical properties of Doxorubicin are used to study adsorption and release of the drug molecule from the nanotube surface. Pilot experiments show strong adsorption of 4 wt% of doxorubicin on the nanotube surface characterized by the quenching of its absorption centered at 490 nm. Quinone and protonated amino groups on the drug molecule, involved in protonation and deprotonation with the surface hydroxyls and molecular water on the nanotube surface, are responsible for adsorption. Doxorubicin adsorbed on the nanotube surface show pH specific release, with 40% release at a

physiological pH of 7.4 as compared to 4% and 10% at pH values of 3.4 and 5.7 respectively under sink conditions. In vitro cytotoxicity experiments, used to characterize the anticancer potential of the nanotube-drug conjugate, shows comparable toxicity for the conjugates as the free drug. Nanotubes with strong adsorption of doxorubicin, large surface area, pH controlled release, and effective toxicity, demonstrate its potential as a vehicle for targeted drug delivery.

If nanotube-drug conjugates with reversible bonds between them, and a pH controlled release in an aqueous solution are promising for medical applications, nanotube-polymer conjugates with nanotubes as reinforcing structures in a polymer matrix with improved mechanical properties are equally promising for structural applications.

Nanotubes are used as reinforcing structures in Surlyn, a polyethylene-co-methacrylic acid polymer containing ions. When cooled from the melt, Surlyn shows strong aging effects on mechanical properties over periods of several days to months. Structures in the matrix of the polymer which form with time are responsible for these aging effects on mechanical properties. Aging at short times after cooling from the melt reveal subtle contributions from these structures not fully formed and mechanical properties not fully recovered. Nanotubes are used as reinforcing structures to improve the mechanical properties at short aging times, a property desired for high temperature applications demanding a quick recovery of mechanical properties. A unique Atomic Force Microscope (AFM) based Local Thermal Analysis (LTA) probe is used to study the mechanical properties of Surlyn and Nanotube-Surlyn composite. Nanotube-Surlyn composites show superior mechanical properties at both short and long aging times after cooling from the melt, as the structures in the matrix continue to form at long aging times.

## ACKNOWLEDGEMENTS

I would like to express my sincere gratitude to my advisor, Prof. Yue Wu. It was his guidance, encouragement and support that led me through the most demanding and rewarding years of my life. His enthusiasm for and insight into science have greatly stimulated me. It has always been a refreshing experience discussing with him. I also want to extend my special gratitude to Dr. Alfred Kleinhammes. I am thankful for his kindness and patience. It would be have been much harder for me without his discussion and encouragement. I am deeply grateful for all the generous help and support from other group members, past and present: Professor Horst Kessemmer, Dr. Lilong Li, Dr. Shenghua Mao, Dr. Yuanyuan Jia, Dr. Qiang Chen, Dr. XueKui Xi, Gregory Mogilevsky, BJ Anderson, and particularly Professor Alfred Kleinhammes. I would like to thank Dr. William M. Mullins for helping me with the simulations and fruitful discussions. I would like to make a special mention of Dr. Rihe Liu and his lab members. I would like to thank Dr. Alex Valencia for all his support in collaborating on this work. I would also like to thank other group members from Dr. Rihe Liu's lab, past and present: Dr. Jim Aloor, Dr. Biao Dong, Dr. Alex Valencia and Steve Cotten.

I would also like to thank all my former and current committee members, Prof. Yue Wu, Dr. Alfred Kleinhammes, Dr. Rihe Liu, Prof. Horst Kessemmer, Prof. Lu Chang Qin, Prof. Wenbin Lin, for their enlightening advice and warm-hearted help. I would like to thank Carolyn for all her love and support. It wouldn't have been possible without her.

Finally, I am very grateful to my parents and my sister. They have been a very strong support throughout my life and helped me achieve my goals.

## CONTENTS

LIST OF FIGURES.....	ix
LIST OF TABLES.....	xii
1) INTRODUCTION.....	1
2) INTRODUCTION TO TITANIA NANOTUBES.....	6
2.1 Tubes Vs Particles.....	6
2.2 Synthesis of Titania Nanotubes.....	9
2.3 Morphology of Titania Nanotubes.....	11
2.4 Structure of Titania Nanotubes.....	14
2.5 Surface Chemistry of Titania Nanotubes.....	19
2.6 References.....	22
3) INTRODUCTION TO DRUG DELIVERY SCIENCE.....	24
3.1 Motivation for Targeted Delivery.....	26
3.2 Nanoparticles for Drug Delivery.....	28
3.3 References.....	40
4) TITANIA NANOTUBE- AS A DRUG DELIVERY DEVICE FOR DOXORUBICIN-AN ANTICANCER DRUG.....	41
4.1 Why Nanotubes?.....	41
4.2 Knowing the Drug.....	43
4.2.1 Optical Properties.....	45
4.2.1.1 Absorption.....	45

4.2.1.2 Fluorescence.....	47
4.3 Testing the Device.....	48
4.3.1 Filling the Nanotube Container - Loading the Drug.....	48
4.3.1.1 Loading Mechanism.....	50
4.3.2 Emptying the Nanotube Container - Releasing the Drug.....	54
4.3.2.1 Release Mechanism.....	59
4.4 Using the Device – In Vitro Cytotoxicity Experiments.....	64
4.4.1 Cell Culture.....	64
4.4.2 Cytotoxicity – Background.....	64
4.4.3 MTS Assay – A Technique for Cytotoxicity Measurement.....	65
4.4.4 Results & Discussion.....	67
4.5 Conclusion.....	72
4.6 References.....	74
5) INTRODUCTION TO SURLYN <sup>®</sup> - AN IONOMER.....	75
5.1 Surlyn – An Intriguing Material.....	75
5.2 Structure of Surlyn <sup>®</sup> .....	76
5.2.1 Composition.....	76
5.2.2 Morphology of Surlyn - Crystallites and Ionic Aggregates.....	77
5.2.3 Structure Formation – A Dynamic Process.....	79
5.2.4 Ionic Aggregates - A Key Component of Ionomers.....	81
5.2.4.1 Formation of Ionic Aggregates.....	81
5.2.4.2 Morphology of Ionic Aggregates.....	82
5.2.4.3 Influence on Crystallites.....	86

5.3 Mechanical properties and Aging effects in Surlyn <sup>®</sup> : As Detected by Macroscopic Techniques.....	88
5.4 References.....	93
6) MECHANICAL PROPERTIES OF SURLYN: AS DETECTED BY A MICROSCOPIC TECHNIQUE.....	94
6.1 Background and Motivation.....	94
6.2 Introduction to Local Thermal Analysis Technique.....	96
6.2.1 A Micron-sized Probe for Creep Measurement.....	97
6.2.2 Choosing the Probe Tip Temperature.....	97
6.2.3 Experimental Procedure for Creep Measurement.....	99
6.2.4 Burger Model: Modeling Creep in Surlyn.....	102
6.3 Results & Discussion.....	106
6.4 References.....	112
7) SURLYN <sup>®</sup> -TITANIA NANOTUBE COMPOSITE: SYNTHESIS, CHARACTERIZATION & MECHANICAL PROPERTIES.....	113
7.1 Background & Motivation.....	113
7.2 Synthesis of Surlyn-Titania Composite.....	116
7.3 Characterization.....	119
7.4 Mechanical Properties.....	120
7.4.1 Materials & Technique.....	120
7.4.2 Results & Discussion.....	122
7.5 Conclusion.....	126
APPENDIX I.....	127
References.....	129

## LIST OF FIGURES

**Figure 2.1** Unit cell of Rutile and Anatase form of titania

**Figure 2.2** Transmission Electron Microscopy image (left) and Scanning Electron Microscopy image (right) of titania nanotubes synthesized by hydrothermal procedure

**Figure 2.3** Synthesis of Short nanotube, nanosheet and nanoribbon form of titania.

**Figure 2.4** Anatase unit cell

**Figure 2.5** Delaminated anatase structure

**Figure 2.6** XRD patterns of anatase, nanosheets, nanotubes, and simulation based on delaminated anatase structure.

**Figure 2.7** Three different schemes of dissociative adsorption of H<sub>2</sub>O on anatase (001) surface.

**Figure 3.1** Large porous micro-particle made of nanoparticles

**Figure 3.2** Microchip based transdermal drug delivery device.

**Figure 3.3** Micelles for drug delivery: a hydrophilic surface and hydrophobic core.

**Figure 3.4** Nanoparticle conjugated to drug through enzyme cleavable linkage.

**Figure 3.5** Carbon nanotube surface modified with different functional groups

**Figure 3.6** Block-co-polymer for DNA and drug delivery

**Figure 3.7** pH dependent release of doxorubicin from polymer-doxorubicin conjugates

**Figure 3.8** SEM pictures of spray-dried (Poly-lactic: glycolic acid) PLGA microparticles

**Figure 4.1** Doxorubicin molecule

**Figure 4.2** Visible absorption (left) and fluorescence (right) spectra of doxorubicin

**Figure 4.3** Molecular orbital model representation of the absorption phenomena

**Figure 4.4** (left) Doxorubicin solution in distilled water.

**Figure 4.5** Absorption intensity of supernatant solution containing free doxorubicin separated from nanotube adsorbed doxorubicin during the adsorption process.

**Figure 4.6** Fluorescence spectra of free doxorubicin in solution (top) and Doxorubicin adsorbed on the nanotube surface (bottom).

**Figure 4.7** Calibration curves of Doxorubicin in Glycine, Acetate and PBS buffers.

**Figure 4.8** Free doxorubicin concentrations released from nanotube-doxorubicin conjugates

**Figure 4.9** Degradation products of Doxorubicin

**Figure 4.10** MTS assay template for cytotoxicity study

**Figure 4.11** cytotoxic effects of a) doxorubicin, b) nanotube-doxorubicin conjugates and c) pure nanotubes on HeLa cells

**Figure 4.12** Cross-section of HeLa cells treated with pure nanotubes.

**Figure 5.1** Schematic representation of Surlyn<sup>®</sup> 8920

**Figure 5.2** Structure of Surlyn

**Figure 5.3** DSC spectra of Surlyn

**Figure 5.4** Region of restricted mobility surrounding a multiplet in a poly(styrene-co-sodium methacrylate) Ionomer

**Figure 5.5** Schematic representation of chain mobility: (A) in the vicinity of an isolated multiplet; (B) in the region of clustered multiplets

**Figure 5.6** Effect of neutralization on primary and secondary crystallites

**Figure 5.7** Temperature dependence of dynamic modulus ( $E'$ ) and the loss ( $E''$ ) for the sheet of EMMA-0.6Zn-0.4BAC aged at 23°C in nitrogen.

**Figure 5.8** Frequency-dependent DMTA data for ionomer 22-48Na, aged at room temperature for 6 days after molding

**Figure 6.1** Scanning electron microscopy image of the Local Thermal Analysis probe.

**Figure 6.2** DSC spectra of Surlyn<sup>®</sup> as a function of relaxation (aging) time.

**Figure 6.3** Experimental procedure for creep measurement.

**Figure 6.4** Creep curves measured at (a) 30°C and at (b) 70°C after aging at room temperature for various aging (relaxation) times.

**Figure 6.5** (a) Burger model with the Maxwell and Voigt elements in series. (b) Characteristic solution of the Burger model for creep under constant stress.

**Figure 6.6** Extracted values based on the Burger model fits of the creep curves.

**Figure 6.7** Illustration of structural relaxation at RT after cooling from the melt.

**Figure 7.1** Titania nanotubes synthesized by hydrothermal process.

**Figure 7.2** a) Composite of Surlyn and titania nanotubes. b) Surlyn prepared from neutralization of acid polymer using same procedure as the composite without the titania nanotubes

**Figure 7.3** a) A fractured surface of the composite as observed by SEM (scale bar 1 $\mu$ )  
b) Tube like structures observed on of the cross-sections coated with polymer c) EDAX analysis shows the presence of titanium atoms as distributed in (b).

**Figure 7.4** Comparison of the Maxwell viscosity and Voigt modulus values for Surlyn and composite as a function of aging time at two temperatures 30°C and 70°C.

## LIST OF TABLES

**Table I.** Total quantity of free doxorubicin released from the nanotube-doxorubicin conjugates under sink conditions

**Table II.** Effect of neutralization on primary crystallite and secondary crystallite melting temperature, bulk modulus of ionomer and crystallinity

# CHAPTER 1

## Introduction

Oxide based nanostructures are a special class of materials used in a variety of industrial applications like photovoltaics, catalysis, filtration, sensors etc. The surface of these nanostructures is crucial for these applications. Metal oxides excel in catalytic applications due to the presence of surface defects which are adsorption sites for reactant molecules<sup>1</sup>. These defects also play an important role in the semiconductor industry and piezoelectric applications. Lots of research has been done in trying to understand the surface of metal oxides, particularly titania (titanium dioxide), resulting in major scientific breakthroughs such as the use of titania in the photocatalytic splitting of H<sub>2</sub>O<sup>2</sup>. Better understanding of the surface of titania generated interest in manipulating of the surface to modulate optical and catalytic properties<sup>3</sup>.

Surface modifiable properties of titania could be extended to other unexplored areas of science. In most applications the nanoparticle form of titania are used, and surface modification of these nanoparticles has shown improved catalytic properties. However, to further improve the properties of nanoparticles which have structural limitations, other morphological forms such as nanotubes should be investigated. Nanotubes have a large

surface area compared to the nanoparticles due to their large aspect ratio and accessible inside/outside surface.

In this dissertation we introduce titania in the form of a nanotube, and evaluate its potential in two different applications. These are titania nanotubes as drug delivery vehicles, and as reinforcing structures in a self healing polymer, Surlyn. Before discussing on these applications, more information of titania nanotubes is needed. In chapter 2, the structural details and surface properties of titania nanotubes which make it a good candidate for the chosen applications is presented. The first application is using titania nanotubes as drug delivery vehicles.

Background information for the drug delivery application is provided in chapter 3. Conventional therapeutic procedures for diseases like cancer, arthritis, and others involve administration of drugs through systemic circulation. These procedures pose a risk to the patient due to non-specific activity of the drug molecules resulting in side effects. Several strategies have been implemented to avoid these side effects by delivering the drug molecules to the specific site<sup>4</sup>. Material science offers an interesting perspective for protected drug delivery. In this chapter we discuss various polymeric and inorganic materials, nanometers in size, used as capsules and protective structures for drug delivery. It is surprising that most of these materials are nanoparticles, while other forms, such as nanotubes, with larger surface areas have not been investigated as drug carriers.

In chapter 4 we explore the potential of the nanotube form of titania as a vehicle for a chemotherapeutic drug, Doxorubicin. Experiments were performed under aqueous conditions to understand the interaction of the nanotube and the drug molecules. Results show efficient

adsorption of drug molecules on the surface of nanotubes and a pH controlled release. In vitro experiments confirm the potential of nanotube as a drug carrier.

Latter parts of the dissertation involve the application of titania nanotubes as reinforcing structures for the synthesis of functional composite material of Surlyn. Background information about Surlyn is provided in chapter 5. Surlyn is a sodium (Na) neutralized polyethylene-co-methacrylic acid polymer, that is semicrystalline in nature. It is a heterogeneous material with strong aging effects on its mechanical properties. These effects are associated with structure-property relations. In chapter 5 structure-property relations and mechanical properties of Surlyn are presented. Conventional techniques such as Differential Scanning Calorimetry (DSC), Dynamic Mechanical Thermal Analyzer (DMTA), which are used to measure these properties, are briefly discussed. They are macroscopic methods of measurement, and have limitations which shall be discussed at the end of this chapter.

Chapter 6 introduces a novel microscopic method to measure the aging effects on mechanical properties. A special Atomic Force Microscope based Local Thermal Analysis (LTA) technique to study the structure-property relations and mechanical property of Surlyn is explained. This technique offers a microscopic characterization procedure, which reveals subtle structural contributions to aging effects on mechanical properties not observed by conventional techniques. The technique is further used to characterize the mechanical properties of the composite of Surlyn. Titania nanotubes are used as reinforcing structures for Surlyn to synthesize a composite with improved mechanical properties.

Chapter 7 presents the synthesis and characterization of Surlyn/titania composite material. The LTA technique is used to compare the mechanical properties of composite with that of Surlyn. Titania nanotubes used as reinforcements improve the properties of Surlyn

significantly. These composites could have potential applications in polymer based photovoltaic materials, solar panels and UV-protective materials for space applications.

## References:

1. Gong, X.Q., Selloni, A., Batzill, M. & Diebold, U. Steps on anatase TiO<sub>2</sub>(101). *Nature Materials* **5**, 665-670 (2006).
2. Hadjiivanov, K.I. & Klissurski, D.G. Surface Chemistry of Titania (Anatase) and Titania-supported Catalysts. *Chemical Society Reviews* **25**, 61-69 (1996).
3. Rajh, T. *et al.* Surface restructuring of nanoparticles: An efficient route for ligand-metal oxide crosstalk. *Journal of Physical Chemistry B* **106**, 10543-10552 (2002).
4. Nie, S., Xing, Y., Kim, G.J. & Simons, J.W. Nanotechnology Applications in Cancer. *Annu. Rev. Biomed. Engg.* **9**, 257-288 (2007).

## CHAPTER 2

### Introduction to Titania Nanotubes

#### 2.1 Tubes vs. Particles:

Titania is naturally found in three crystal structure forms; anatase, rutile and brookite. Of the three structures, brookite is the least stable. Anatase and rutile structures, as shown in Figure 2.1, offer interesting material applications. Titania is a well known oxide material used for photo catalysis in solar cells, fuel cells, bone implant materials, pigment for paints, and so forth. Catalytic properties of titania play an important role in all of these applications. It offers a physically and chemically stable platform for catalytic processes. It is interesting to note that in spite of a larger band gap, the anatase form of titania shows greater photocatalytic efficiency as compared to the rutile form, and is widely used for catalytic applications<sup>1</sup>. Anatase nanoparticles can be fabricated into various device forms for solar cell and fuel cell applications.

Surface modified titania nanoparticles are used to cover the broad spectrum of wavelength otherwise restricted by inherent optical properties of titania nanoparticles, and thus tailor their photo catalytic properties. Dye molecules or charge-transfer ligands are used for modification<sup>2</sup>. Immobilization of these molecules onto the surface of nanoparticles is

possible because of a reactive titania surface. A large surface area is desired for better surface coverage of molecules which yield better optical properties.

Titania (Anatase) nanoparticles of 32 nm in size have a surface area of approximately 45m<sup>2</sup>/g. Surface area of nanoparticles is one of the limiting factors for efficient use in catalysis. Successful attempts were made at synthesizing different forms of titania based nanostructures with increased surface areas<sup>3</sup>. These include one dimensional nanotubes, nanorods, and two dimensional nanosheets. Nanotubes are one of the widely studied forms of titania and have shown promising results over the past few years<sup>4-6</sup>.

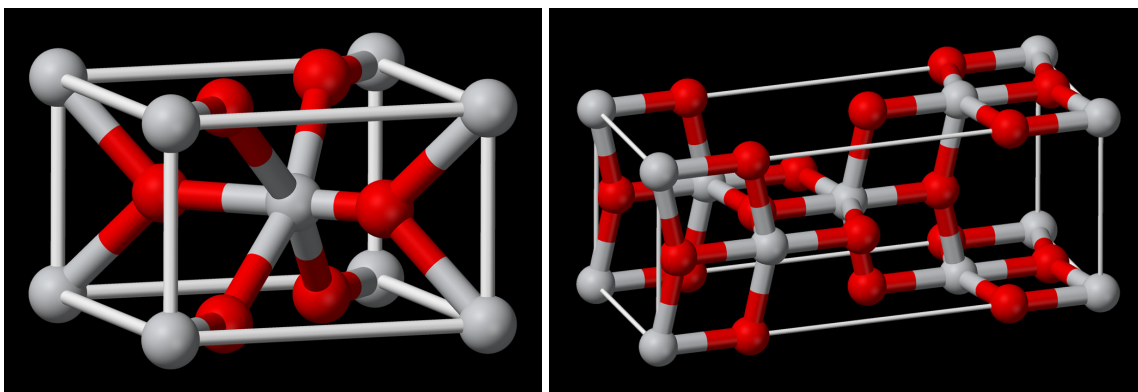


**Figure 2.1** Unit cell of Rutile (left) and Anatase (right) form of titania (Gray: Ti atoms, Red: O atoms)

Synthesis of a nanotubular form of titania was first reported by Kasuga et al. in the year 1998<sup>7</sup>. The tubular form of titania, as shown in Figure 2.2, has a surface area of 250 m<sup>2</sup>/g, about five times that of the nanoparticle. Large quantities of dye molecules and charge-transfer ligands have been immobilized on the surface of titania nanotubes for photocatalytic applications<sup>8-10</sup>. The nanotubes have an inside diameter of 5-6 nm. A tube with this diameter is ideal for containing large biological molecules such as proteins and materials with therapeutic value. Large surface area and a unique inside/outside geometry also offer room for selective surface modification to make a multifunctional device.

Understanding the structure of the nanotubes would certainly prove to be valuable in making such devices. In this chapter a brief review of the synthesis of nanotubes, other forms of titania, structure, and surface chemistry are discussed.

## 2.2 Synthesis of Titania Nanotubes:

Different procedures exist for the synthesis of titania nanotubes. Two principle methods are used; one being a sequential process of synthesis of titania nanoparticles from precursor titanium alkoxide compounds which are then converted to nanotubes by alkaline treatment, and the other which is a more direct hydrothermal synthesis process involving raw material anatase nanoparticles to form nanotubes<sup>7,11</sup>. We follow the latter process as it is simple and direct.

The procedure involves heating 4g of anatase nanoparticles in an alkaline solution of 12M sodium hydroxide at 130°C for 72 hours. Heating is carried out in a teflon autoclave enclosed in a stainless steel cylinder. After the sample is cooled to room temperature, product in the form of a thick sheet with excess sodium ions is obtained. The product is then sonicated for 30 minutes to break up the large chunks of the material. After sonication, the aqueous solution of the intermediate product is distributed into several centrifuge tubes. The tubes are then centrifuged and the precipitate sits at the bottom, and the supernatant solution at the top is discarded. A simple washing procedure is employed to get rid of the excess sodium ions. The washing solution is poured into the centrifuge tube and is mixed well by using a vortexer. The tubes are then centrifuged and pH of the top solution is measured before it is discarded. 0.1 M HCl followed by deionized water are used as washing solutions until the pH of the top solution reaches 5-6. The precipitate is then dried overnight in an oven at 50°C producing a white powder. Scanning Electron Microscopy of the white powder (figure 2.2) shows elongated tube like structures. The synthesis process is simple and scalable.

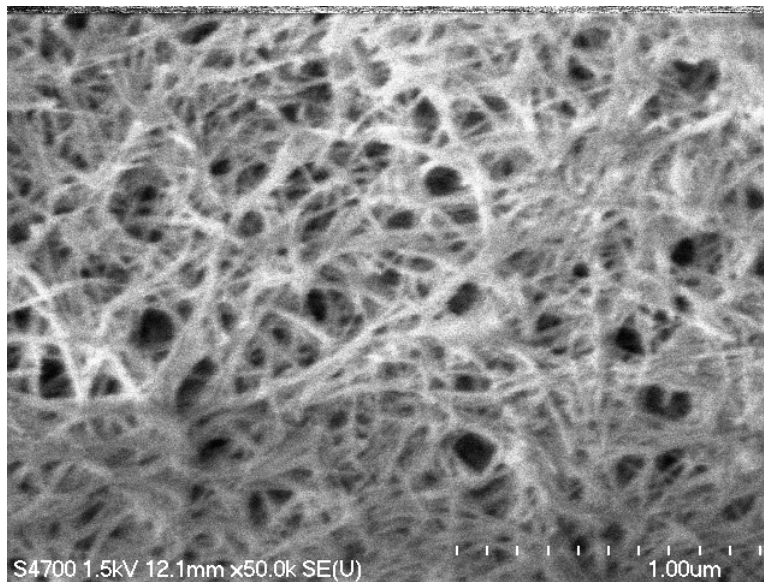
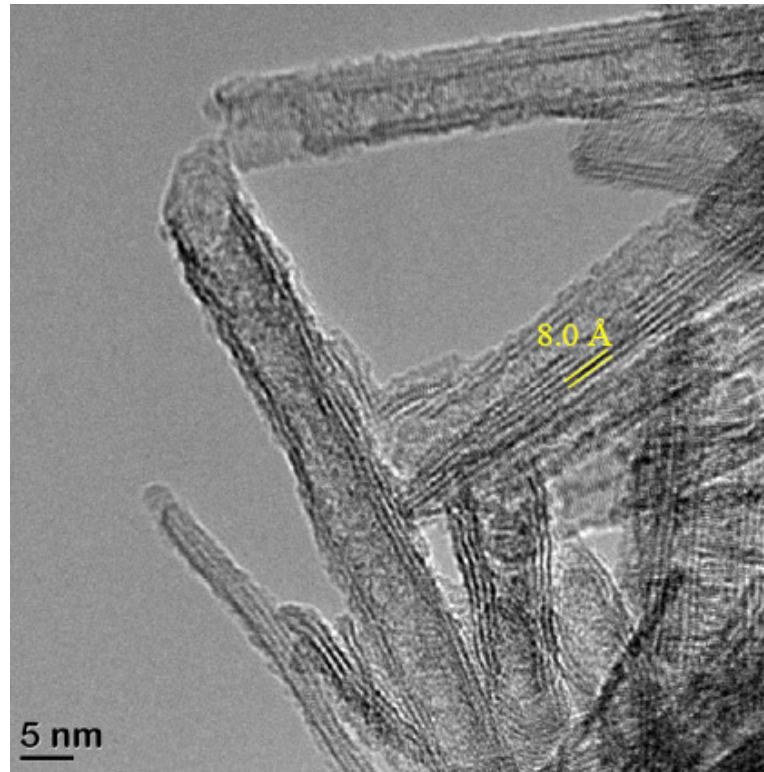


**Figure 2.2** Transmission Electron Microscopy image (left) and Scanning Electron Microscopy image (right) of titania nanotubes synthesized by hydrothermal procedure

### 2.3 Morphology of Titania Nanotubes & Other Structural Forms:

As synthesized nanotubes are elongated structures with high aspect ratios. Individual nanotubes can range from a few hundreds of nanometers to a micron in length. Transmission Electron Micrographs (figure 2.2) show that the nanotubes have an inside diameter of ~5nm and outside diameter of ~10nm. Imaging of nanotubes at various tilt angles has shown that the structure is tubular and not planar. Amorphous particles and crystalline sheet like structures are also observed along with the tubular structures.

As synthesized nanotubes can be modified into other forms such as short nanotubes, nanosheets and nanoribbons.

#### Short Nanotubes:

Grinding and sonication procedures are commonly used for segmentation of inorganic nanotubes<sup>12-14</sup>. Aqueous solution of as synthesized titania nanotubes was prepared for grinding. 0.1 $\mu$ m ZrO<sub>2</sub> beads in water are used as the grinding media and an ice jacket is surrounds the grinding media to control the temperature and to avoid overheating caused by friction. The solution is ground for 30 minutes, and once the grinding is stopped the ZrO<sub>2</sub> beads sink to the bottom of the solution as these are denser than the suspended nanotubes. The suspension is then separated and characterized. TEM of the suspension (figure 2.3) show nanotubes ranging from 50-200 nm in length.

#### Nanosheets:

The above procedure when repeated without the ice jacket and using 0.1 $\mu$ m ZrO<sub>2</sub> beads in boiling water as the grinding solution yields surprising results. TEM of the suspension (figure 2.3) reveals a mixture of amorphous and sheet like material. However, high resolution TEM shows lattice fringes across the nanosheet matching the lattice spacing

in the (001) plane of the anatase<sup>15</sup>. Selected Area Electron Diffraction (SAED) shows diffraction spots suggesting crystalline nature of the nanosheets. AFM characterization has shown that the nanosheets are several atomic layers thick.

### Nanoribbons:

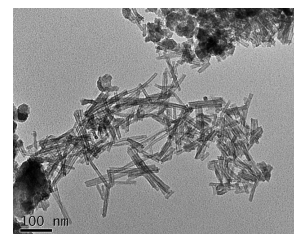
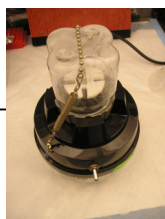
Nanoribbons can be synthesized by following similar procedure as the synthesis of nanotubes except that it is carried out at elevated temperatures  $\sim 240^{\circ}\text{C}$ . Nanoribbons are  $\sim 100\text{nm}$  in diameter and several microns in length. This morphology of titania interestingly retains the anatase crystal structure, however short nanotubes and nanosheets do not.

Different morphologies of nanotubes offer interesting chemical properties because of subtle differences in the surface structures. Detailed understanding of these surface structures will help us gain more knowledge about the surface of titania nanostructures in general.

Short Nanotubes

As synthesized  
Nanotubes

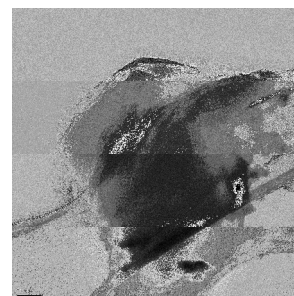
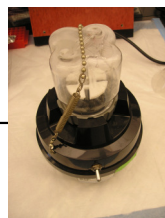
Ice bath



Nanosheets

As synthesized  
Nanotubes

Boiling  
water



Nanoribbons

Anatase nanoparticles (4g)  
NaOH (160g), 400 ml ddH<sub>2</sub>O

$\Delta$  240°C, 72 hrs

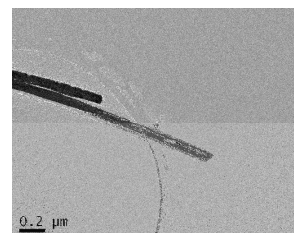


**Figure 2.3** Synthesis of Short nanotube, nanosheet and nanoribbon form of titania.  
A grinding media was used for short nanotubes and nanosheets,  
nanoribbons were synthesized by hydrothermal procedure  
Scale bar: 100 nm (top), 50 nm (center), 0.2 μ (bottom)

## 2.4 Structure of Titania Nanotubes:

Since the nanotubes were first synthesized almost a decade ago, several model structures have been put forward to explain the structural basis of nanotubes. Anatase, the raw material used for the synthesis of nanotubes is a layered structure which has a unit cell as shown in Figure 2.4. All the proposed structures are different stoichiometric and ionic forms of this layered structure. These include anatase, mixture of anatase and rutile structures, structures with different Ti:O ratios, monoclinic trititanate structures, orthorhombic protonated titanate structures and titanate with vacancies<sup>7,11,16,17</sup>. None of these structures provide a comprehensive understanding of the building blocks of nanotube. A new anatase based structure was proposed<sup>15</sup>.

The unit cell shown in Figure 2.4 is cleaved in the [001] direction with a spacing of 8.7Å to give a delaminated form of anatase. Delaminated structure of the anatase unit cell is shown in Figure 2.5. This structure is consistent with the crystal structure of nanotubes and nanosheets and provides better understanding of improved catalytic properties of nanotubes over anatase nanoparticles<sup>10</sup>. Simulations of the delaminated anatase structure have been performed and compared with the experimental observations.

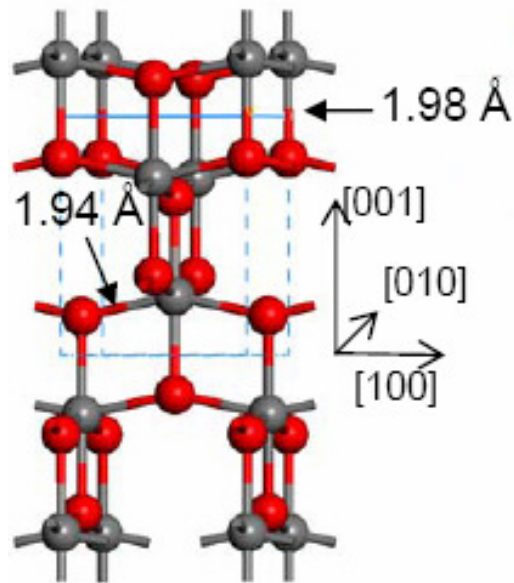


**Figure 2.4** Anatase unit cell<sup>15</sup>.

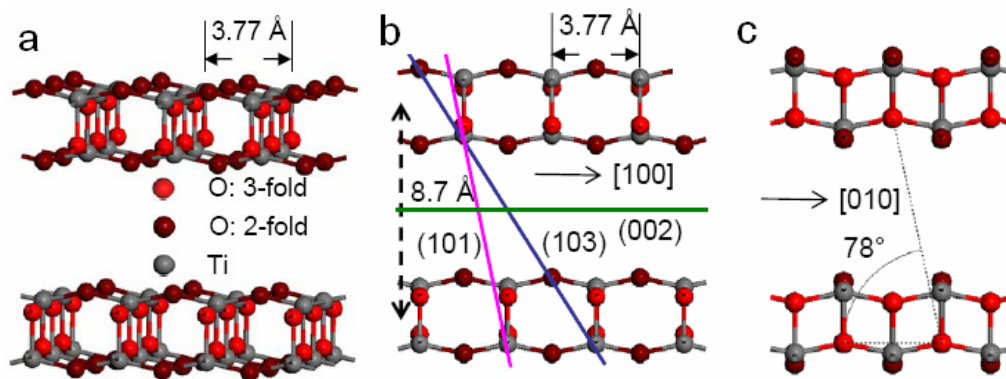


**Figure 2.5** Delaminated anatase structure

(a) Illustration of layers delaminated in [001] direction

(b, c) Delaminated structure viewed from different perspective

The three major planes that are seen in XRD are shown in green (002), blue (103), and purple (101). The glide shift is 78° at interlayer spacing of 8.7 Å<sup>15</sup>

XRD simulation of delaminated anatase structure was compared with the experimental XRD for nanotubes and nanosheets. Nanotubes and nanosheets derived from the grinding of the nanotubes show similar X-ray diffraction results as shown in Figure 2.6. The peak positions line up very well. This suggests that both the materials share the same intrinsic structure.

Nanotube and nanosheet structures made of delaminated anatase should be constructed in simulation software for comparison with experimental data. However construction of nanotube made of delaminated anatase requires more information. Since both nanotubes and nanosheets have the same diffraction peak positions a fair comparison could be made between the simulation data for nanosheets made of delaminated anatase unit cells and the diffraction data for nanotubes.

X-ray diffraction of nanosheets made of delaminated anatase unit cells was simulated and compared with the experimental diffraction peaks for the nanotubes and nanosheets. Peak positions of simulated nanosheet structure agree with experimental diffraction peaks of nanotubes and nanosheets (figure 2.6). The peak at  $2\theta=10.2^\circ$  translates to an interlayer distance of  $8.7\text{\AA}$ , a key feature of the delaminated structure as shown in Figure 2.4. An additional broad peak was observed in the background for the nanosheets positioned at  $2\theta=28^\circ$ . It was attributed to the size effects of the nanosheets.

TEM observations are also consistent with the delaminated anatase model. The delamination distance ( $8.7\text{\AA}$ ) (figure 2.5) is close to the interlayer distance observed in the TEM of the nanotubes ( $8\text{\AA}$ ). The difference in the spacing is due to the desorption of the water molecules from the layers due to vacuum. The inter-atomic distance of  $3.77\text{\AA}$  between the titanium atoms matches with the lattice fringes observed in the TEM of the nanosheets.

The two layers shown in figure 2.5 are offset by half a unit cell in [100] and [010] directions such that they form a glide angle of  $78^\circ$  also observed in HRTEM images of the nanotubes. Lattice fringes observed in the TEM of the nanosheets correspond to the lattice spacing of atoms in the (001) plane (figure 2.5).

All these observations confirm that the delaminated anatase structure is a comprehensive structure model and should help in better understanding of the catalytic properties of nanotubes.

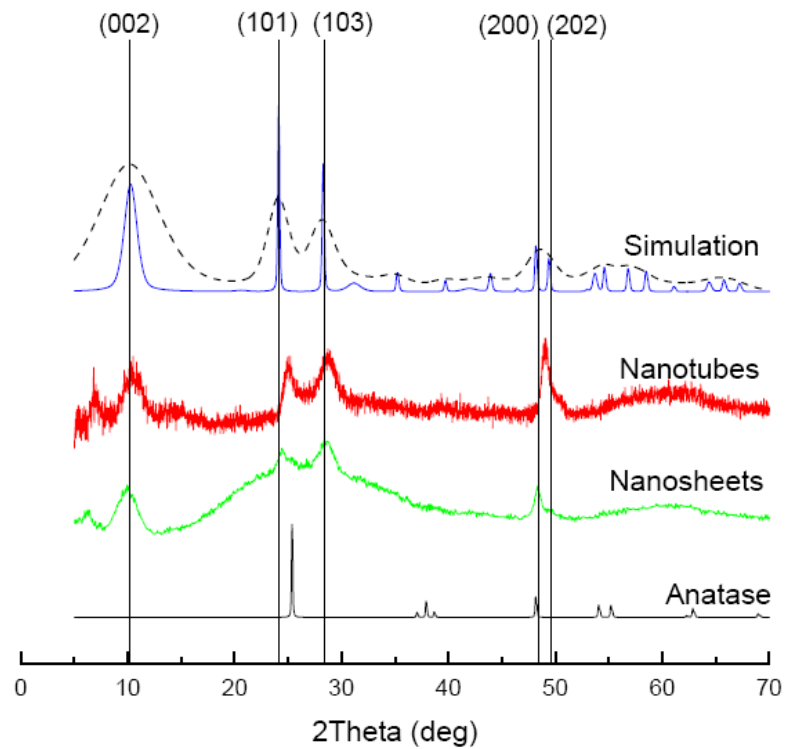


**Figure 2.6** XRD patterns of anatase, nanosheets, nanotubes, and simulation based on delaminated anatase structure. Blue line shows the simulation for nanosheet constrained in the c-direction and the dotted black line shows the simulation for nanosheet constrained in all the three directions. Broadened peak seen in the measured XRD of nanosheets may be attributed to limited size of individual crystallites or the background glass slide<sup>15</sup>.

## 2.5 Surface Chemistry of Titania Nanotubes:

Titania is widely used as a support material for various catalytic reactions and also as a catalyst. As a support material, titania has strong interactions with noble metals and these supported catalysts are used for industrial applications. These include Pt/TiO<sub>2</sub> catalysts for photocatalytic splitting of water. The structure of titania is crucial in dictating such applications.

For titania nanoparticles, discontinuities in crystal lattices lead to exposure of under-coordinated titanium cations. Thus nanoparticles have uncompensated positive charge and attract lone pair of electrons acting as Lewis acids. Some of the previous proposed models explain the charge balance of these under-coordinated cations by the presence of defects<sup>18</sup>. However, in delaminated anatase structure they are accounted by the presence of two-fold coordinated bridging oxygen with lone pair of electrons.

Studies have shown that water adsorbs on the surface of titania nanoparticles in two forms; molecular water and dissociated water. Dissociation of water molecules results in hydroxyl groups on the surface. Titania nanoparticles synthesized by different routes have shown the presence of hydroxyl groups<sup>2</sup>. Hydration is also dependent on the exposed plane of the structure. There seems to be a preference for (001) plane of the anatase structure for dissociation of water as shown by previous studies<sup>19</sup>. Hydration of titania surface promotes catalytic processes as shown by previous studies.

Surface complexation of catechol and other organic molecules at the hydrated interface of titania is well understood<sup>2</sup>. Terminal hydroxyl groups attached to the under-coordinated titanium atoms dominate the surface complexation of catechol, an organic molecule with bidentate hydroxyl groups. It would be interesting to discuss the state of

hydrated surface of nanotubes and nanosheets as it would play an important role in surface reactions.

Delamination of the anatase unit cell exposes under-coordinated titanium atoms and bridging oxygen atoms with lone pair of electrons which are active reaction sites. Titania nanosheets show experimental evidence for splitting of water<sup>15</sup>. Water is adsorbed on the surface of nanosheets both molecularly and in the dissociated form. Dissociated water yields hydroxyl groups on the surface. Several possibilities of distribution of the hydroxyl groups are shown in figure 2.7. One possibility is the dissociative adsorption of water molecules by forming terminal hydroxyl groups on two adjacent under-coordinated titanium atoms by breaking the  $Ti_{5c}-O_{2c}$  bond. The second possibility is the formation of hydroxyl groups on  $Ti_{5c}$  by breaking the  $Ti_{5c}-O_{2c}$  bond, but the OH group attaches to the adjacent  $Ti_{5c}$  site forming a six coordinated  $Ti_{6c}-OH$  bond leaving behind a fourfold coordinated Ti atom. The third possibility is the formation of two terminal hydroxyl groups; one on  $Ti_{5c}$  without breaking the  $Ti_{5c}-O_{2c}$  bond thus forming a  $Ti_{6c}-OH$  bond and the other one on  $O_{2c}$  called the bridging oxygen hydroxyl. These are the different possible scenarios of the formation of different types of hydroxyls. NMR results for the nanosheets suggest the formation of terminal hydroxyl groups on the two adjacent Ti atoms as shown by figure 2.7a<sup>15</sup>. NMR results for nanotubes suggest that water adsorbs in a molecular form and does not show significant dissociation. This suggests that nanosheets have a more reactive surface as compared to nanotubes.

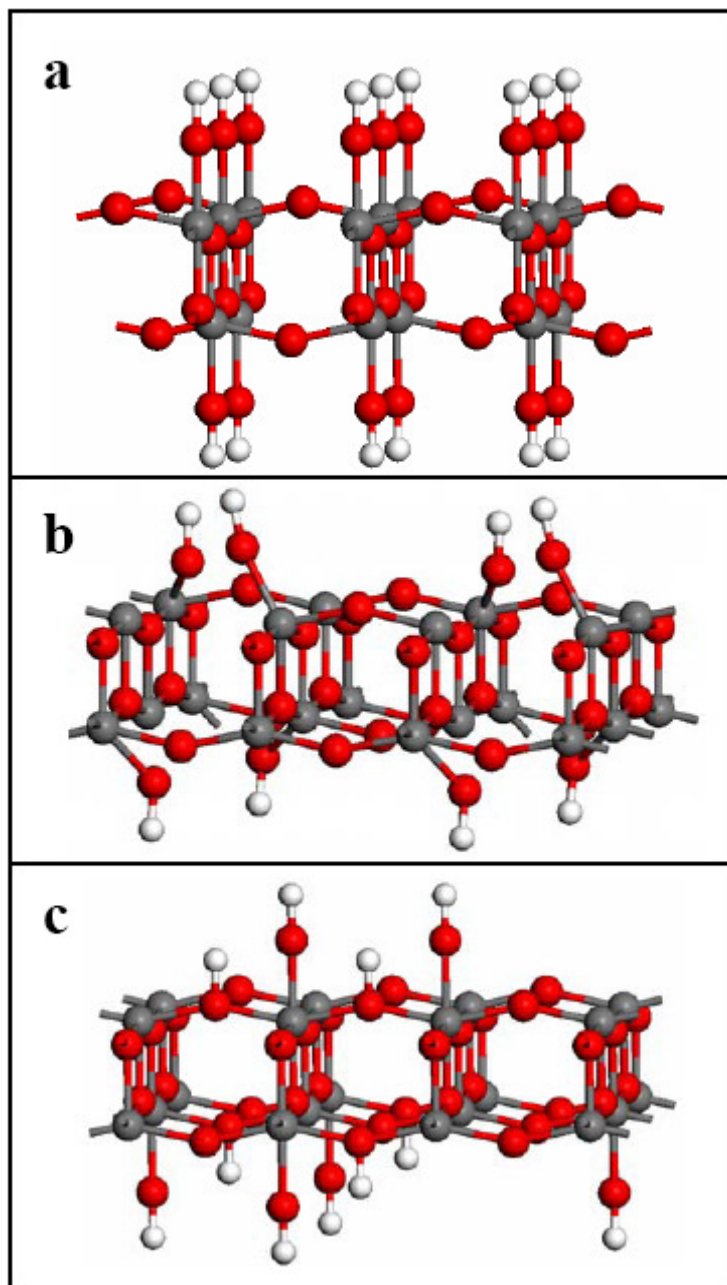


**Figure 2.7** Three different schemes of dissociative adsorption of  $\text{H}_2\text{O}$  on anatase (001) surface. (a)  $\text{H}_2\text{O}$  dissociates into a proton and a hydroxyl group by breaking the bridging O-Ti bond. The hydroxyl group settles on the Ti site forming a terminal hydroxyl, while the proton completes the newly formed nonbridging O site, also forming a terminal hydroxyl. The resulting configuration leaves all Ti fivefold coordinated. (b)  $\text{H}_2\text{O}$  dissociates as in (a). However, instead of settling the OH on the newly created  $\text{Ti}_{4c}$  site, the OH settles on the adjacent  $\text{Ti}_{5c}$  site, making it sixfold coordinated and leaving behind a  $\text{Ti}_{4c}$  site. Unlike in (a), two very different terminal hydroxyls are formed. (c)  $\text{H}_2\text{O}$  dissociates where the hydroxyl settles on the fivefold coordinated Ti site, making it sixfold coordinated, while the proton settles on bridging oxygen forming a bridging hydroxyl<sup>15</sup>.

## 2.6 References:

1. Rajh, T., Nedeljkovic, J.M., Chen, L.X., Poluektov, O. & Thurnauer, M.C. Improving optical and charge separation properties of nanocrystalline TiO<sub>2</sub> by surface modification with vitamin C. *Journal of Physical Chemistry B* **103**, 3515-3519 (1999).
2. Rodriguez, R., Blesa, M.A. & Regazzoni, A.E. Surface complexation at the TiO<sub>2</sub> (anatase) aqueous solution interface: Chemisorption of catechol. *Journal of Colloid and Interface Science* **177**, 122-131 (1996).
3. Saponjic, Z.V. et al. Shaping nanometer-scale architecture through surface chemistry. *Advanced Materials* **17**, 965-+ (2005).
4. Varghese, O.K., Gong, D.W., Paulose, M., Grimes, C.A. & Dickey, E.C. Crystallization and high-temperature structural stability of titanium oxide nanotube arrays. *Journal of Materials Research* **18**, 156-165 (2003).
5. Zhao, J.L., Wang, X.H., Sun, T.Y. & Li, L.T. Crystal phase transition and properties of titanium oxide nanotube arrays prepared by anodization. *Journal of Alloys and Compounds* **434**, 792-795 (2007).
6. Zheng, Q., Zhou, B.X., Bai, J., Cai, W.M. & Liao, J.S. Titanium oxide nanotube arrays and their applications. *Progress in Chemistry* **19**, 117-122 (2007).
7. Kasuga, T., Hiramatsu, M., Hoson, A., Sekino, T. & Niihara, K. Formation of titanium oxide nanotube. *Langmuir* **14**, 3160-3163 (1998).
8. Mor, G.K., Varghese, O.K., Paulose, M., Ong, K.G. & Grimes, C.A. Fabrication of hydrogen sensors with transparent titanium oxide nanotube-array thin films as sensing elements. *Thin Solid Films* **496**, 42-48 (2006).
9. Zhuang, H.F., Lai, Y.K., Li, J., Sun, L. & Lin, C.J. Fabrication of highly ordered titanium dioxide nanotube array and investigation of its photocatalytic activity. *Acta Chimica Sinica* **65**, 2363-2369 (2007).
10. Jia, Y.Y. et al. Synthesis and characterization of TiO<sub>2</sub> nanotube/hydroquinone hybrid structure. *Journal of Nanoscience and Nanotechnology* **7**, 458-462 (2007).
11. Kasuga, T., Hiramatsu, M., Hoson, A., Sekino, T. & Niihara, K. Titania nanotubes prepared by chemical processing. *Advanced Materials* **11**, 1307-+ (1999).
12. Lee, J. et al. Short carbon nanotubes produced by cryogenic crushing. *Carbon* **44**, 2984-2989 (2006).

13. Jeong, S.H. & Lee, K.H. Field emission properties of short crystalline carbon nanotubes cut by sonication on substrate. *Japanese Journal of Applied Physics Part 2-Letters & Express Letters* **43**, L1106-L1108 (2004).
14. Liu, F. et al. Preparation of short carbon nanotubes by mechanical ball milling and their hydrogen adsorption behavior. *Carbon* **41**, 2527-2532 (2003).
15. Mogilevsky, G. et al. Layered Nanostructures of Delaminated Anatase: Nanosheets and Nanotubes. *J. Phys. Chem. C* **112**, 3239-3246 (2007).
16. Du, G.H., Chen, Q., Che, R.C., Yuan, Z.Y. & Peng, L.M. Preparation and structure analysis of titanium oxide nanotubes. *Applied Physics Letters* **79**, 3702-3704 (2001).
17. Sun, X.M. & Li, Y.D. Synthesis and characterization of ion-exchangeable titanate nanotubes. *Chemistry-a European Journal* **9**, 2229-2238 (2003).
18. Ma, R.Z., Bando, Y. & Sasaki, T. Nanotubes of lepidocrocite titanates. *Chemical Physics Letters* **380**, 577-582 (2003).
19. Gong, X.Q. & Selloni, A. Reactivity of anatase TiO<sub>2</sub> nanoparticles: The role of the minority (001) surface. *Journal of Physical Chemistry B* **109**, 19560-19562 (2005).

## CHAPTER 3

### Introduction to Drug Delivery

#### 3.1 Motivation for Targeted Delivery:

Pharmaceutical science has undergone a series of revolutions for improved drug performance. This includes improvement of solubility, stability, permeability to biological membrane, targeting to particular tissues, cells and intracellular compartments. Close control of all of these desired properties have been tried to achieve optimized drug performance. These properties can be divided into two categories; one which involves the biological function of the drug molecules, and the other which relates to physicochemical characteristics.

Drug molecules are synthesized to achieve the best of both the properties. However, at some point it is difficult to achieve all of these, and certain properties are compromised. This results in drugs with side effects, higher toxicity and other ill-effects. To retain all of the above mentioned properties and achieve the best results, new materials were discovered which are multifunctional in nature and provide better solutions to drug delivery.

These materials are composites of drug molecules and carrier systems which protect the drug from being released before it reaches the target site. Conventional dosage forms of drug molecules when administered show rapid release, and peak to toxic levels followed by

concentrations which decrease over time and are ineffective. Carrier systems with controlled release characteristics are used for long lasting effects, and avoid toxic levels of drug molecules to be released.

Another important motivation for these systems is that disease causing organisms such as pathogenic cells and tumor cells develop a situation called multi-drug resistance, wherein certain proteins in the organism or the cells pump the drug molecules out of the cytoplasm of the cell. Thus in order to kill the pathogenic organisms or avoid tumor growth excess drug concentration has to be used to overwhelm the proteins so that an effective dose is capable of achieving the desired effect. In doing so, however the side effects are escalated and could pose a threat to the body.

Several carrier systems are thus used to achieve both multifunctional materials for protected delivery without compromising on pharmacological properties and escape the multidrug resistance of the organism or the tumor cells. In the following section we discuss the different types of nanoparticle systems used as drug delivery vehicles.

### 3.2 Nanoparticles for Drug Delivery:

Nanoparticles used for drug delivery can be broadly classified into three different categories based on their physical, chemical and biological characteristics. These are size, type of material (organic/inorganic), conjugation/encapsulation technique, and disease condition.

#### Size:

Carrier systems used for drug delivery applications can range from a few nanometers to a few microns in diameter. Size affects the course of nanoparticles once administered inside the body. The size effects also depend on the route of administration which can be nasal, oral, intra-venal or transdermal. Too small a size of the nanoparticle can cause aggregation leading to difficulty in aerosolization for nasal delivery, and drug release in the lungs. Large porous micron size particles made of nanoparticles have been synthesized to achieve both good aerosolization properties and better drug delivery characteristics (figure 3.1)<sup>1</sup>. Nanoparticles of several tens of nanometer in size can cross the leaky vasculature of tumor cells to deliver chemotherapeutic agents. Particles of only a few nanometers, if not targeted properly, could also circulate across the body and have toxic effects to vital organs such as heart. Thus size is an important factor for engineered application of nanoparticles in drug delivery.

Apart from individual nanoparticle systems, microtechnology fabrication techniques have also been employed to create microchips which contain drug reservoir arrays for transdermal drug delivery (figure 3.2). These reservoirs which are several microns in size release the drug solution when an electric potential is applied, and controlled release can be

obtained by molding special features such as valves on the chip<sup>2</sup>. The microchip fabrication technology could be used to treat diabetes and other medical conditions.

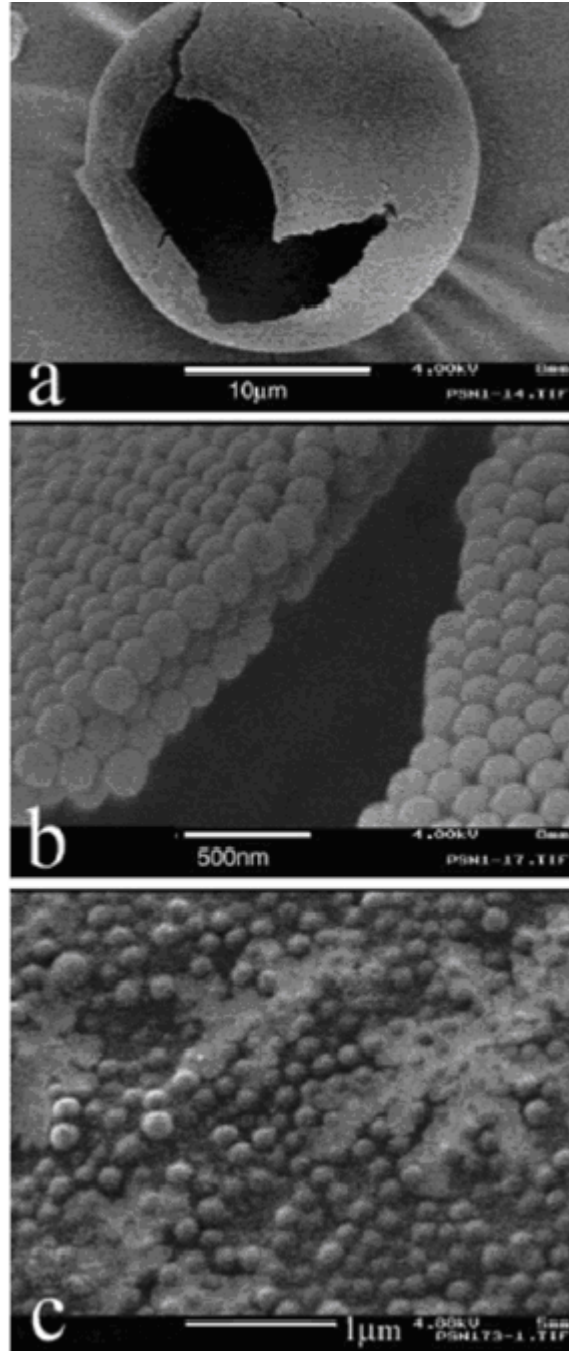


**Figure 3.1** Large porous micro-particle made of nanoparticles  
(a) hollow micron sized particle, (b) a magnified view of the particle in (a) showing the shell made of nanoparticles, (c) individual nanoparticles after dispersion of the micro-particle in a solution of ethanol/water<sup>1</sup>.

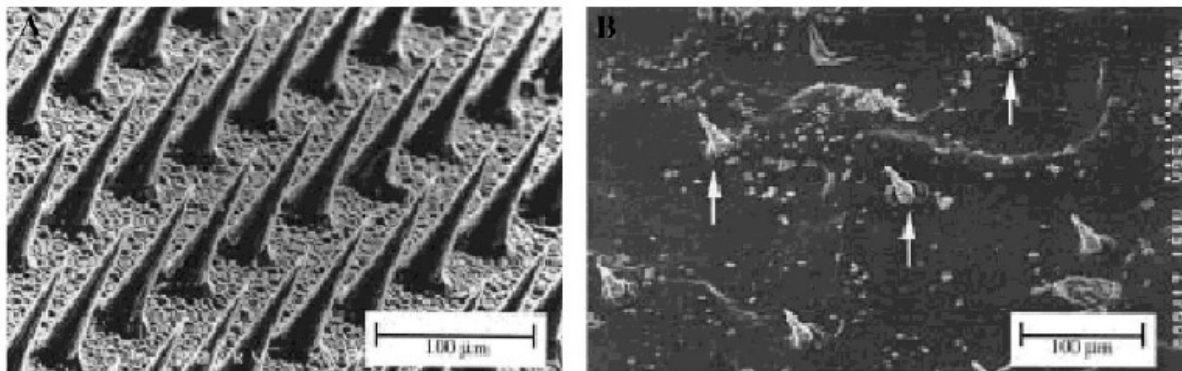


**Figure 3.2** Microchip based transdermal drug delivery device. SEM image of (left) array of needle shaped drug reservoirs, (right) micro needle tips inserted across the epidermal region of the skin, white arrows show the insertions made by the needles<sup>2</sup>.

#### Type of material:

A large variety of nanostructures made of different materials is used for drug delivery applications. These are either organic nanoparticle systems or inorganic materials.

Organic nanoparticles are among the most widely used carriers for drug delivery applications due to their ease of encapsulation, surface modification capabilities by binding ligands for targeting purposes which allows prolonged systemic circulation for sustained drug delivery. Several biodegradable and biocompatible organic nanoparticles such as polyesters, polyanhydrides, poly (ethylene) glycol and poly (lactic) acid loaded with drug molecules are synthesized. Poly (lactic) acid nanoparticles alone are not efficient for drug delivery. However, block-co-polymers such as PEG/PLA are commonly used to make the nanoparticles hydrophilic with better therapeutic efficiency<sup>3</sup>. Block-co-polymers in specific solvents yield interesting structures called as micelles where the hydrophobic regions self associate in an aqueous environment away from water to form the core and hydrophilic

regions form the surface of the structure. Hydrophobic drug molecules selectively partition into the hydrophobic core (figure 3.3)<sup>4</sup>.

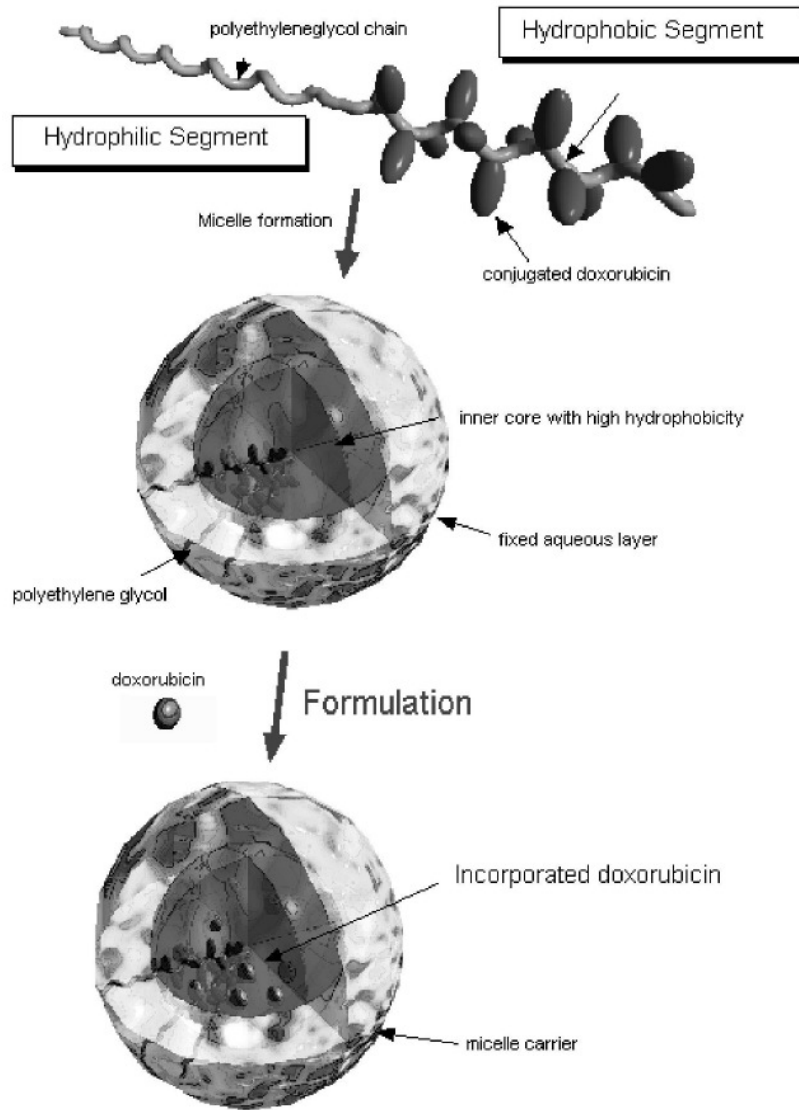


**Figure 3.3** Micelles for drug delivery: a hydrophilic surface and hydrophobic core. Doxorubicin, a chemotherapeutic drug conjugated to hydrophobic chains protected in the hydrophobic core of the micelles<sup>4</sup>.

Surface modification of polymer nanoparticles with a variety of ligands is possible for targeting the drug molecules. Drug molecules could be attached to nanoparticles through bonds which can be cleaved by enzymes as they enter the cellular compartments releasing the

drug molecules to perform their desired function (figure 3.4)<sup>5</sup>. Polymer nanoparticle systems thus demonstrate good encapsulation design for loading drug molecules, smart nanoparticle-drug complex for timely release of drug molecules, and biocompatibility. Apart from being used as nanoparticles, polymer materials containing drug molecules could also be used for coating medical devices such as stents. However, these materials generate an inflammatory response from the cells in the surrounding blood vessels.

Oxide based materials could be used as alternatives for such applications. Some of the polymer nanoparticles face problems such as degradation and leakiness under physiological conditions. Inorganic materials could possibly provide alternative solution to such problems.

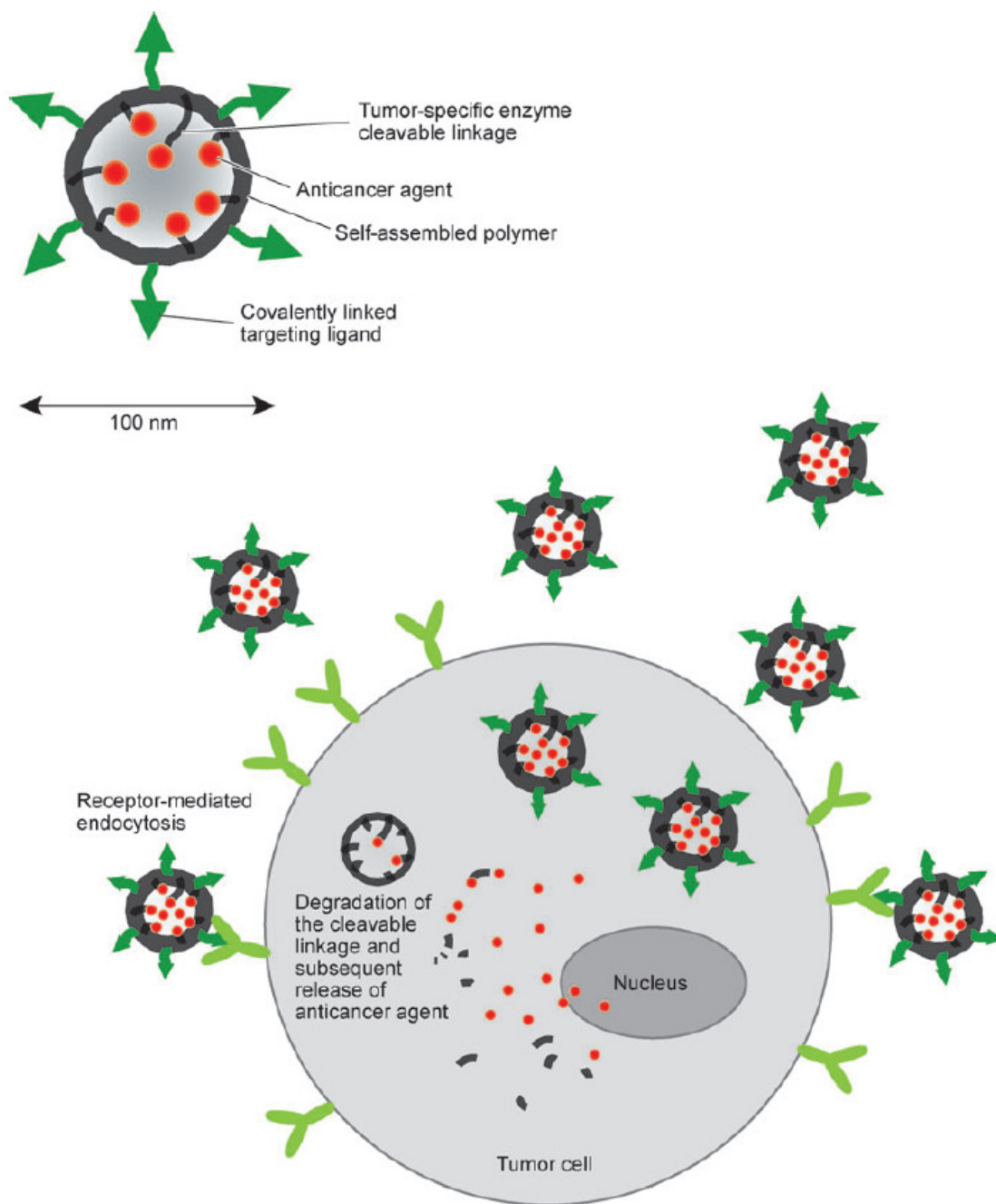


**Figure 3.4** Nanoparticle conjugated to drug through enzyme cleavable linkage. Targeting ligands on surface of nanoparticles attach to receptors on cell surface and enter the cell. Drug released by enzymatic degradation of the linkage<sup>6</sup>.

Amorphous oxide coatings have been successfully used as a platform for drug delivery in stent devices and can replace polymeric materials<sup>7</sup>. A broad range of functional groups can be attached to the surfaces of inorganic materials to explore their potential as drug delivery vehicles. For example carbon nanotubes (figure 3.5) have shown the potential for surface functionalization, and the ability to deliver macromolecules such as DNA and other proteins<sup>8</sup>.

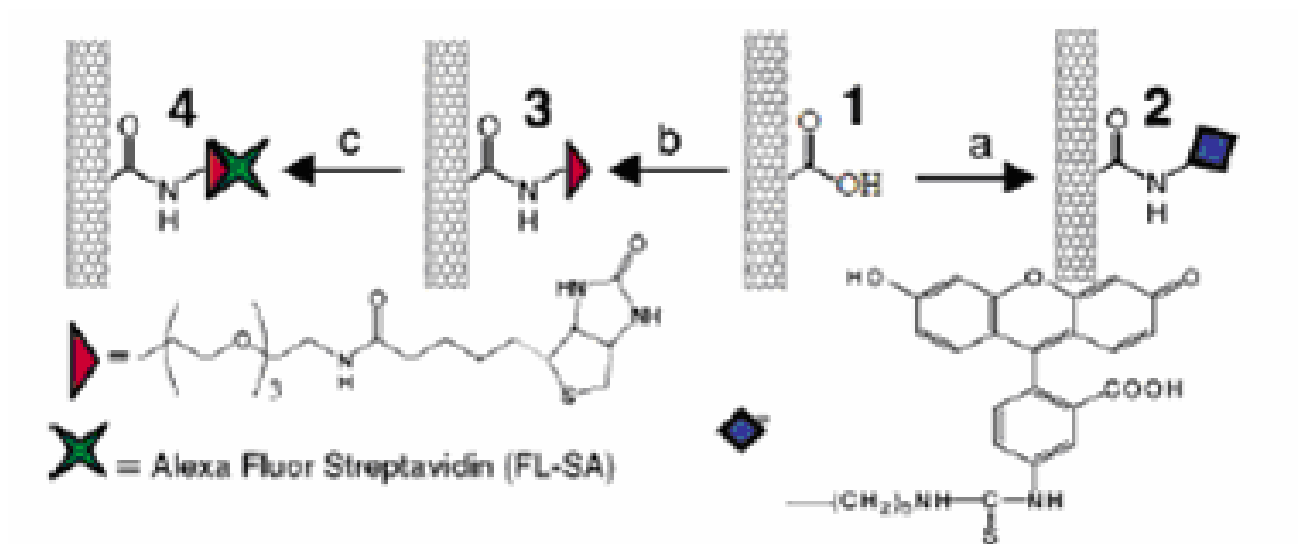


**Figure 3.5** Carbon nanotube surface modified with different functional groups<sup>8</sup>.

In addition to therapeutic potential, diagnostic applications such as iron oxide for MRI contrast imaging have also been explored<sup>9</sup>. Inorganic nanomaterials provide a stable support system for drug delivery.

Some of the issues that inorganic systems could face however are solubility and toxicity, as these are not biodegradable. Studies have shown that the solubility can be improved by functionalization, and standard tests exist to determine the toxic effects of inorganic nanomaterials before they could be used for drug delivery applications.

## Conjugation/Encapsulation Technique:

Several conjugation techniques exist for incorporation of drug molecules into the nanoparticle systems. The two determining factors for these techniques are 1) qualitative and quantitative encapsulation efficiency 2) triggered or controlled release.

Qualitative efficiency of a conjugation is based on the need for a localized effect without exceeding toxic levels in rest of the body. Protected delivery of macromolecules, such as DNA, by forming electrostatic complexes with cationic polymer nanoparticles has been tried. However, enzymatic degradation releases the DNA before reaching the target site. Micellar structures made of block-co-polymers were used as protective structures to target the DNA. Drug-cationic polymer complex (figure 3.6) forms the hydrophobic core and poly (ethylene) glycol molecules form the hydrophilic surface of the micelles<sup>10</sup>. Similar strategies are employed for protected delivery of other drug candidates.

Some of the conjugation techniques require the exposure of drug molecules to harsh polymerization reactions which affects their stability. Simple strategies, such as hydrophobic partitioning into polymeric nanoparticles, are used to maintain the integrity of drug molecules, and have the desired effect at the target site. The nature of the solvent used for encapsulation also plays an important role in determining the encapsulation efficiency of the drug molecules<sup>11</sup>. Solvents with non-protonated forms of the drug doxorubicin show better hydrophobic partitioning inside the nanoparticles with a hydrophobic core<sup>12</sup>. Interesting differences in loading efficiencies and morphology are observed as the composition of polymer nanoparticles is changed<sup>11</sup>.

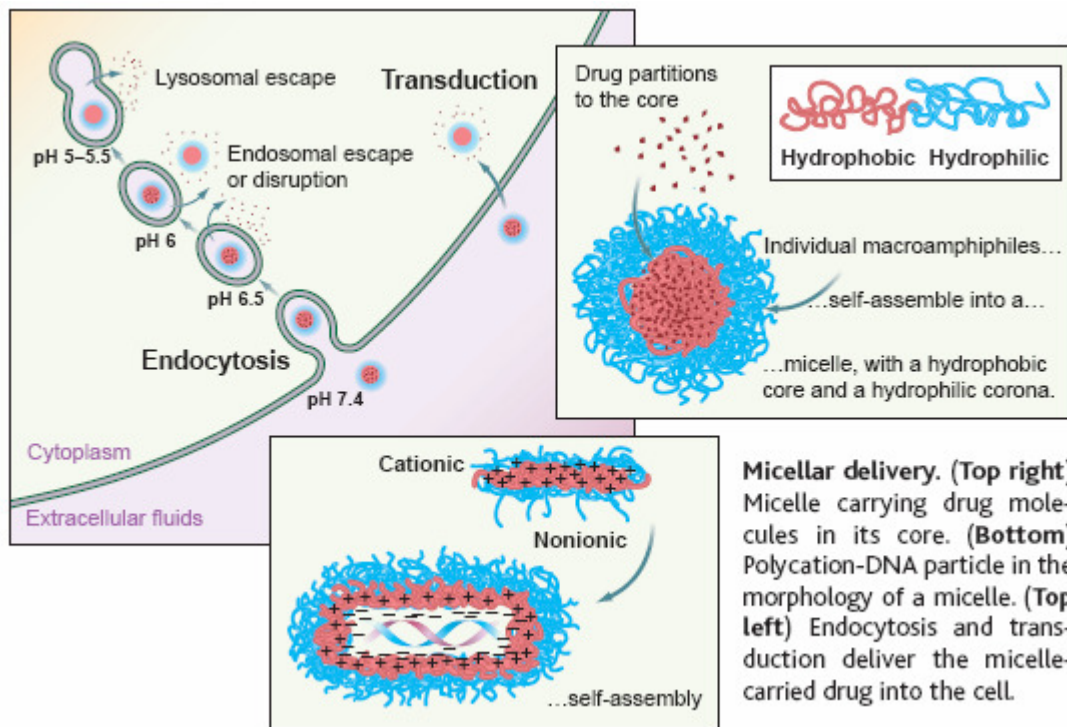


**Figure 3.6** Block-co-polymer for DNA and drug delivery<sup>10</sup>.

The nature of bond between the drug molecules and the nanoparticle carrier system is crucial in controlling the drug release kinetics. Triggered or controlled release of drug molecules is dependent on four factors which are; 1) location of the drug molecules, 2) type of bonding between the drug and the nanoparticles, 3) size and morphology of nanoparticles, and finally the 4) composition of the nanoparticles.

As mentioned before, drug molecules adsorbed on the surface of nanoparticles are prone to enzymatic degradation before they reach the target site, and are released in an uncontrolled manner. Protective micellar structures which host the drug molecules in the hydrophobic core of the nanoparticles show controlled release characteristics.

Smart nanoparticle systems are designed such that the bonds between the nanoparticle and the drug moiety are pH sensitive, and are cleaved by enzymes to release the drug.

Polymer-doxorubicin conjugates show such differences as the complex is hydrolyzed in different pH solutions. Higher release rates are observed for acidic pH as shown in (figure 3.7)<sup>5</sup>.

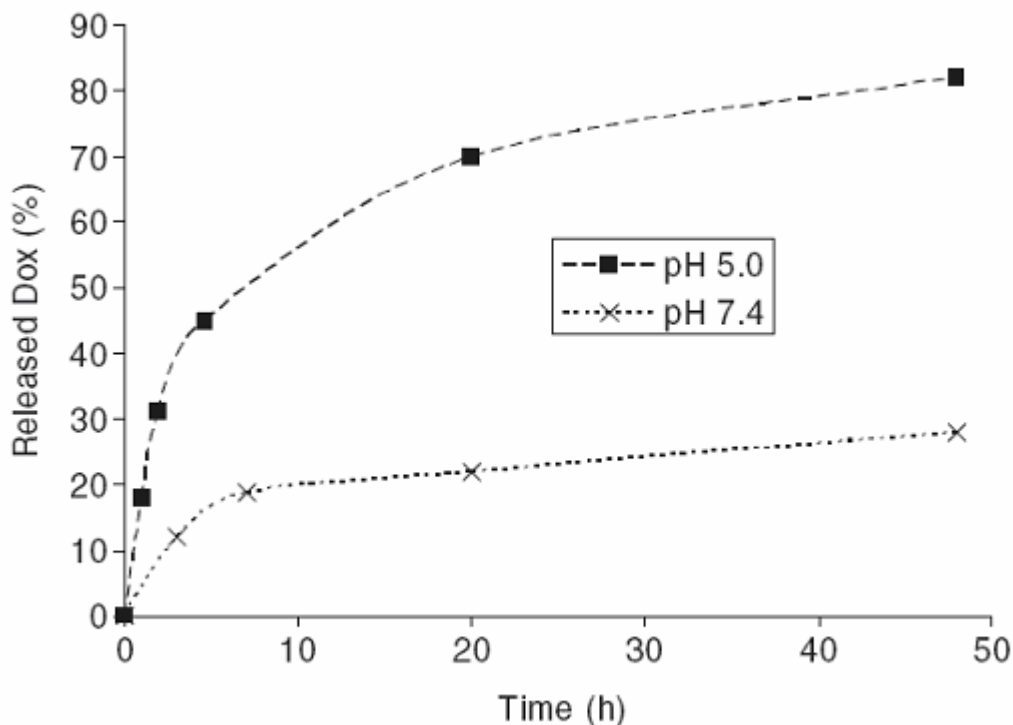


**Figure 3.7** pH dependent release of doxorubicin from polymer-doxorubicin conjugates<sup>5</sup>.

Such systems have great potential for transportation of drug molecules into cellular organelles called endosomes, which have lower pH values as compared to the rest of the cell. The drug molecules can be released inside these structures and the drug can perform further action. A localized and pH dependent drug release for chemotherapeutic treatment such as this show that concentrations lower than the free anticancer drugs can produce similar cytotoxic effects.

Small nanoparticles could show larger burst effects such as undesired and uncontrolled release of drug molecules as compared to large sized nanoparticles. This could be due to weak adsorption of drug molecules as excess quantities are loaded on the nanoparticle surface.

Varying the composition of composite nanoparticles can change the particle size and the morphology from particle to disc-like structures, in turn affecting the release characteristics (figure 3.8)<sup>11</sup>.

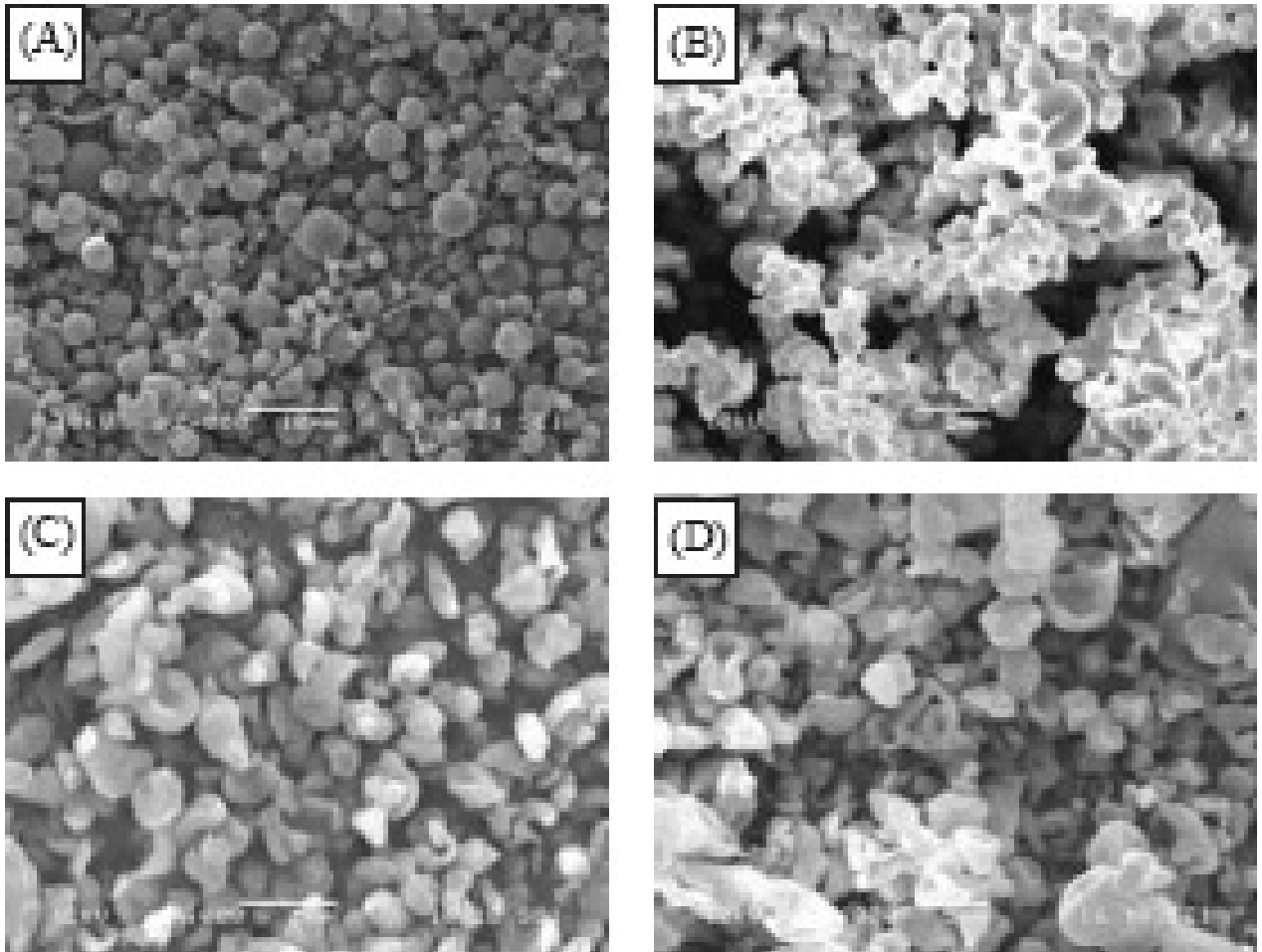


**Figure 3.8** SEM pictures of spray-dried (Poly-lactic: glycolic acid) PLGA microparticles. Different morphologies for two co-polymer ratios: from spheres for 65:35 to disc shape for 85:15; (A) Blank PLGA 65:35 microparticles; (B) drug-loaded PLGA 65:35 microparticles (C) drug-loaded PLGA 65:35 microparticles in the presence of a surfactant; (D) drug-loaded PLGA 85:15 microparticles in the presence of a surfactant.<sup>11</sup>

## Disease Conditions:

A wide range of disorders can be treated by using novel nanoparticle drug delivery systems. One of the most researched area is that of cancer. Cancer cells are different from normal cells in the body. Certain receptors found on the surface of the cell wall are over expressed in cancer cells as compared to the normal cells. These over expressed receptors are used as gateways for the treatment of cancer. Cancer treatment involves either a diagnostic approach where nanoparticles with surface ligands are used to target tumor sites followed by radiation therapy, or an invasive approach by using drug delivery followed by targeting. Thrombosis is another critical condition associated with heart attack and strokes caused by the formation of a clot. A protein called fibrin is responsible for clot formation. Thrombolytic drugs are targeted to the clot sites using biocompatible nanoparticles to break down the fibrin, and eventually the clot. Arthritis and Diabetes Mellitus are among the other diseases for which nanoparticles based drug delivery systems are being investigated.

### 3.3 References:

1. Tsapis, N., Bennett, D., Jackson, B., Weitz, D.A. & Edwards, D.A. Trojan particles: Large porous carriers of nanoparticles for drug delivery. *Proceedings of the National Academy of Sciences of the United States of America* **99**, 12001-12005 (2002).
2. Tao, S.L. & Desai, T.A. Microfabricated drug delivery systems: from particles to pores. *Advanced Drug Delivery Reviews* **55**, 315-328 (2003).
3. Caliceti, P., Salmaso, S., Elvassore, N. & Bertucco, A. Effective protein release from PEG/PLA nano-particles produced by compressed gas anti-solvent precipitation techniques. *Journal of Controlled Release* **94**, 195-205 (2004).
4. Nakanishi, T. et al. Development of the polymer micelle carrier system for doxorubicin. *Journal of Controlled Release* **74**, 295-302 (2001).
5. Pechar, M., Braunova, A., Ulbrich, K., Jelinkova, M. & Rihova, B. Poly(ethylene glycol) - Doxorubicin conjugates with pH-controlled activation. *Journal of Bioactive and Compatible Polymers* **20**, 319-341 (2005).
6. Nie, S.M., Xing, Y., Kim, G.J. & Simons, J.W. Nanotechnology applications in cancer. *Annual Review of Biomedical Engineering* **9**, 257-288 (2007).
7. Shih, C.M., Lin, S.J., Su, Y.Y. & Shih, C.C. Amorphous oxide - a platform for drug delivery. *Journal of Controlled Release* **102**, 539-549 (2005).
8. Kam, N.W.S., Jessop, T.C., Wender, P.A. & Dai, H.J. Nanotube molecular transporters: Internalization of carbon nanotube-protein conjugates into mammalian cells. *Journal of the American Chemical Society* **126**, 6850-6851 (2004).
9. Sun, C., Sze, R. & Zhang, M.Q. Folic acid-PEG conjugated superparamagnetic nanoparticles for targeted cellular uptake and detection by MRI. *Journal of Biomedical Materials Research Part A* **78A**, 550-557 (2006).
10. Hubbell, J.A. Enhancing drug function. *Science* **300**, 595-596 (2003).
11. Lin, R.Y., Ng, L.S. & Wang, C.H. In vitro study of anticancer drug doxorubicin in PLGA-based microparticles. *Biomaterials* **26**, 4476-4485 (2005).
12. Gillies, E.R. & Frechet, J.M.J. pH-responsive copolymer assemblies for controlled release of doxorubicin. *Bioconjugate Chemistry* **16**, 361-368 (2005).

## CHAPTER 4

### Titania Nanotube- As a Drug Delivery Device for Doxorubicin: An Anticancer Drug

#### 4.1 Why Nanotubes?

Efficient and targeted drug delivery with minimal side effects holds the key for the effectiveness and success of anticancer chemotherapy. It is essential to find high payload vehicles of anticancer drugs with targeting capability. Polymeric systems have been explored widely for such purpose. However, the payload of such systems is often limited.

From a materials science point of view, large surface area sorbent materials are the most effective in carrying adsorbates such as drug molecules. So far, because of a large number of requirements the sorbent materials have to meet simultaneously, promising inorganic sorbent materials have not been identified for drug delivery. Novel structures of titania nanotubes could be used for anticancer drug delivery.

The 5-6 nm inner diameter of a titania nanotube is ideal for loading large drug molecules. The possibility of carrying out inside/outside surface chemistry in titania nanotubes enables functionalization of the outside surface with hydrophilic polymeric coating, and attaching targeting ligands. Thus, nanotubes functionalized on the surface and

drug molecules loaded inside could be used as a targeted drug delivery vehicle. Such hybrid material could possess the desirable features of both inorganic and organic systems, and could yield a clinically viable and effective anticancer drug delivery system. In this chapter, we characterize the loading and release of doxorubicin, a chemotherapeutic drug, from the nanotube surface as a first step towards exploring such possibilities.

First, we introduce the structure of doxorubicin and its characteristic optical properties used as an important tool for this study. Adsorption and desorption experiments were carried out to determine the binding characteristics of doxorubicin on the surface of nanotubes. Optical measurements were used to characterize the entire process. In vitro experiments were performed for the nanotubes loaded with the drug molecules. Results of the In vitro experiments are discussed to determine the efficacy of nanotubes as doxorubicin transporters.

## 4.2 Knowing the Drug:

Doxorubicin is widely used as a chemotherapeutic drug for the treatment of cancer. It intercalates with the DNA inside the cell nucleus and destroys the function of DNA essential for the growth of cancer cells. It has a tetra-cyclic benzene ring, called the chromophore linked to an amino sugar group as shown in figure 4.1<sup>1</sup>. The drug molecule has quinone and hydroxyquinone groups present on the chromophore at C5, C12 and C6, C11 respectively. It was shown that both the chromophore and the amino group play an important role in binding to the DNA<sup>2</sup>. Interesting studies have been conducted to identify the binding mechanism of the drug to the DNA.

In order to achieve effective transportation of the drug molecules into the cell, various nanoparticle carrier systems were investigated as mentioned in chapter 3. In this section, adsorption and desorption phenomenon of doxorubicin on titania nanotube surface is being discussed. Doxorubicin has unique optical properties such as absorption and fluorescence as shown in figure 4.2, which are used as important tools in this study. We shall first discuss these properties<sup>3</sup>.

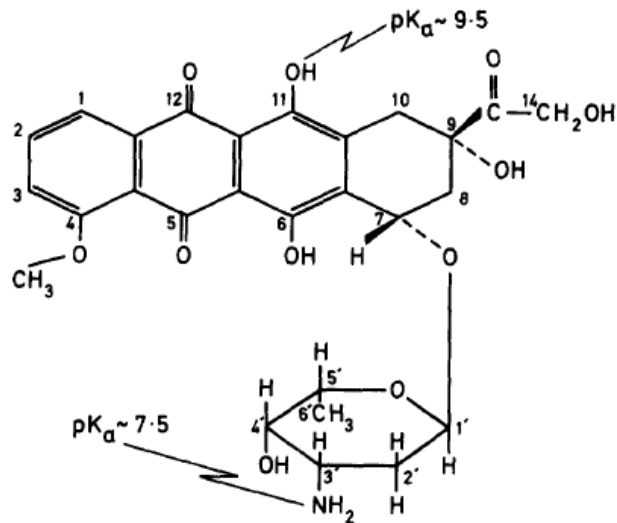


**Figure 4.1** Doxorubicin molecule: benzene ring (chromophore) attached to the sugar group. The chromophore is responsible for optical properties of the molecule<sup>1</sup>

## 4.2.1 Optical Properties

### 4.2.1.1 Absorption:

Valence electrons in an atom are loosely bound to the nucleus. Incident photon energy induces the transition of valence electrons of an atom from a ground state to an excited state as shown in figure 4.3. This process is called absorption. Molecular orbital theory can be used to explain the absorption phenomenon<sup>4</sup>. A bond between the atoms is formed by the sharing of valence electrons in the atomic orbital. When atomic orbitals on each of adjacent atoms are combined they produce two molecular orbitals, one of higher energy and one of lower energy than the atomic orbitals. The lower energy orbital is called a bonding orbital and represents the ground state electronic configuration. The higher energy orbital is called an antibonding orbital which can be occupied in an electronically excited state. These orbitals can be of three types depending on the kind of bond; one is symmetrical about the internuclear axis called a  $\sigma$  or  $\sigma^*$  based on their bonding or antibonding nature, the

second one is antisymmetric about the plane that includes the internuclear axis called as  $\pi$  or  $\pi^*$ , and the third type is called as a non-bonding orbital 'n' which represents a lone pair of

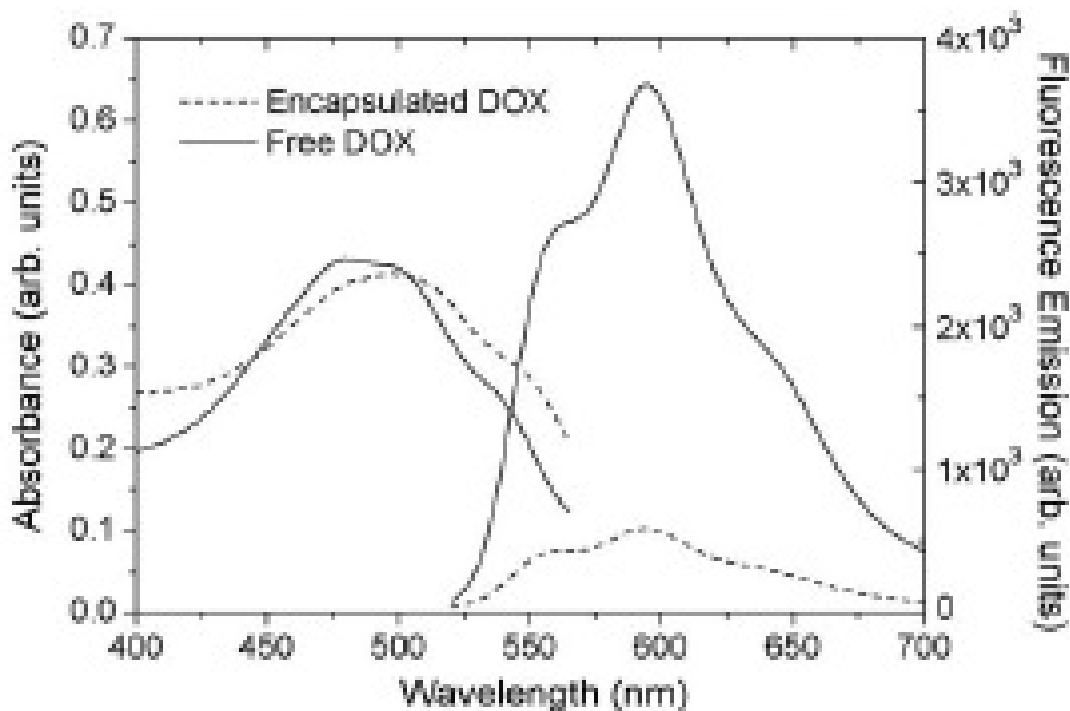


**Figure 4.2** Visible absorption (left) and fluorescence (right) spectra of doxorubicin (dark line)<sup>3</sup>

electrons on a particular atom (oxygen for doxorubicin) and has the highest ground state energy level as shown in figure 4.3.

C-C single bond has  $\sigma$  orbitals and C=C has both  $\sigma$  and  $\pi$  orbitals occupied in the ground state. An incident photon excites the electrons from these states into the respective antibonding orbital energy levels causing  $\sigma \rightarrow \sigma^*$  and  $\pi \rightarrow \pi^*$  transitions as shown in figure 4.3.  $n \rightarrow \pi^*$  transitions are usually observed in molecules containing atoms with strong electro negativity. For a molecule containing all these bond types, absorption intensity is higher for  $\pi \rightarrow \pi^*$  transition than those corresponding to  $\sigma \rightarrow \sigma^*$  or  $n \rightarrow \pi^*$  transitions.

The chromophore part of the doxorubicin molecule has carbon atoms bound to each other by alternate single and double bonds. Due to abundance of the single and double bonds in the chromophore, doxorubicin has strong absorption properties. Studies have also shown strong  $n \rightarrow \pi^*$  transitions in doxorubicin<sup>5</sup>. These are sensitive to the protonated-deprotonated state of the chromophore. The transitions are translated into absorption peaks at wavelengths corresponding to the difference in the energy levels.  $\pi \rightarrow \pi^*$  and  $n \rightarrow \pi^*$  are the two transitions reported in literature for doxorubicin. These transitions are related to the fluorescence properties as discussed in the following section. Absorption spectrum of doxorubicin solution or any other organic molecules is broad and separation of these electronic transitions is not possible. However it shows an absorption maximum at ~490nm and is useful for our purposes.

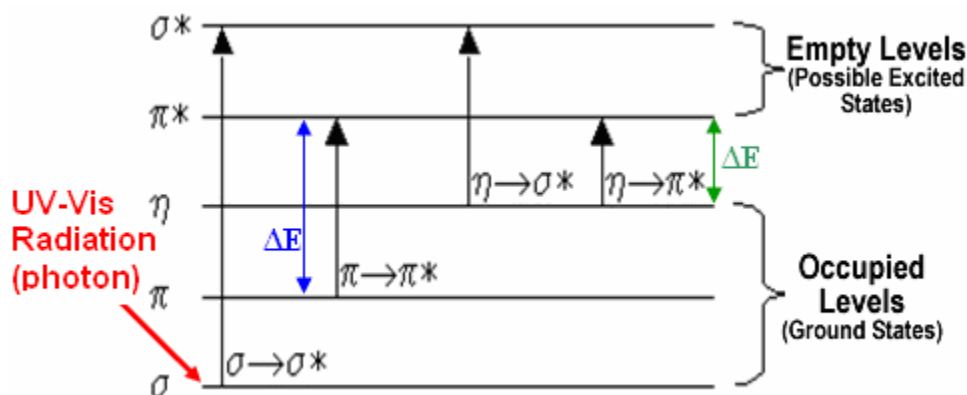


**Figure 4.3** Molecular orbital model representation of the absorption phenomena

#### 4.2.1.2 Fluorescence:

Fluorescence is a property closely related to absorption. An electronically excited state has two unpaired electrons in different orbitals. These electrons have opposite spins so that the electronic state has an overall spin of zero. This is usually the situation for excited states produced by absorption of a photon, and is called as a singlet state as shown in figure 4.3. When the excited singlet state emits a photon, the state transfers to the ground state, which is also a singlet state. Such a radiative process in which there is no overall change of spin is called fluorescence. The radiated photon is characteristic of the excited singlet state and is related to the excited-state energy in the absorption process.

Fluorescent peaks of doxorubicin molecule are related to the  $\pi \rightarrow \pi^*$  and  $n \rightarrow \pi^*$  transitions during the absorption process. Doxorubicin shows three peaks; one centered at ~590 nm, and two shoulder peaks at 560 and 640 nm. The peak with the maximum intensity positioned at 590 nm corresponds to photon emission followed by  $\pi \rightarrow \pi^*$  transition during absorption. The other two peaks correspond to photon emission followed by  $n \rightarrow \pi^*$  transition during absorption. Changes in the peak position provide details of the electronic state of the molecule. The important feature of fluorescence is that very weak signals can be measured by the detectors and are normally used in chemical analysis for detecting and measuring quantitatively extremely small amounts of material<sup>4</sup>.

Absorption is measured using a BioTek Absorbance Microplate Reader. Fluorescence is measured using a Nanodrop Fluorospectrophotometer ND-3300.

### 4.3 Testing the Device:

#### 4.3.1 Filling the Nanotube Container – Loading the Drug:

Doxorubicin. HCl (mol. wt: 540 g/mol) from Fisher Scientific was used for this study. The drug is a red colored powder stored at room temperature and protected from light. Loading/adsorption experiments were carried out under ambient conditions.

2 mg of doxorubicin was added to 10 ml of distilled water and stirred to give a ruby red colored solution as shown in figure 4.4. To this solution 50 mg of as synthesized titania nanotubes were added and stirred. During the stirring procedure a 200 $\mu$ l sample solution was taken out at different times and each of these was centrifuged at 12000 rpm to separate the free drug in the solution from the drug molecules adsorbed on the nanotube surface. Absorbance of the top solution was measured to monitor the amount of free drug left in the solution at different time intervals. After the stirring is stopped, the ruby red colored solution turns colorless in a few minutes as the nanotubes adsorbed with drug molecules settle down. The drug molecules are immediately adsorbed on the surface of titania nanotubes as shown by the instantaneous drop in the absorbance intensity (figure 4.5). The adsorption process is discussed in more detail in the following section. Quantitative estimation of the doxorubicin content has been discussed in the Appendix I section.



**Figure 4.4** (left) Doxorubicin solution in distilled water.  
(right) Red precipitate (bottom) of nanotube-doxorubicin conjugate formed after addition of nanotube to doxorubicin solution. Nanotube-doxorubicin conjugates are used for drug delivery

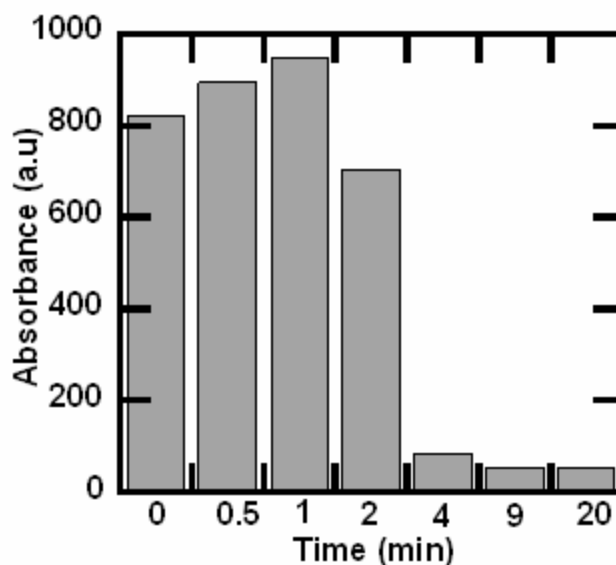
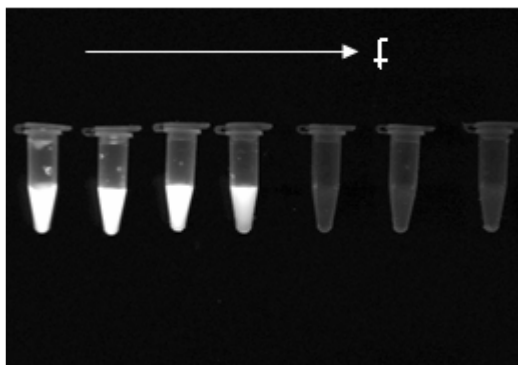


**Figure 4.5** Absorption intensity of supernatant solution containing free doxorubicin separated from nanotube adsorbed doxorubicin during the adsorption process. Decreasing intensity of free doxorubicin in solution shows increased adsorption of doxorubicin on the nanotube surface.

#### 4.3.1.1 Loading Mechanism:

Metal oxide/aqueous interfaces play an important role in the adsorption of organic molecules. Water adsorbs on the surface of titanium oxide in two forms: one as molecular water and the other in the dissociated form<sup>6</sup>. Dissociated water forms hydroxyl groups on the surface of metal oxides. Multisite complexation approach has been used to explain the

adsorption of organic molecules at the metal oxide/aqueous interface. This involves protonation-deprotonation of hydroxyl groups adsorbed on the surface of the metal oxide and the adsorbing organic molecules. Interesting studies have been conducted to understand the role of dissociated water for complexation of organic molecules, such as catechol and hydroxyquinone on the surface of titania<sup>6</sup>. Different hydroxyl species from the dissociated water have different acidities based on the co-ordination number of the anchoring atom. These are dictated by the crystal faces of the metal oxide.

Adsorption of doxorubicin on the surface of titania nanotubes can be thought of as a two step process. First step is the hydration of the nanotube surface and the second step is the surface complexation of doxorubicin. For titanium dioxide nanotubes, as mentioned in chapter 2, most of the adsorbed water is in the molecular form. However, presence of small quantities of dissociated water was detected by NMR<sup>7</sup>. There are two types of hydroxyl groups formed as a result of dissociation as mentioned in chapter 2; 1) attached to a 5-fold co-coordinated titanium atom without breaking the Ti=O bond to give a  $Ti_{6c}-OH$ , and 2) attached to a bridging oxygen with lone pair of electrons. Each of these hydroxyl groups is a good protonation-deprotonation site. These hydroxyl groups are however not available in abundance for binding. Thus the surface of titania nanotubes hydrated with molecular water could play an active role in the binding of doxorubicin.

Doxorubicin is hydrophobic in nature, however when dissolved in water, protonation of amino groups of the molecule make it more soluble. Protonated amino groups on the doxorubicin molecule could bind to the bridging oxygen through hydrogen bonding. Protonation of the amino groups does not alter the optical properties of doxorubicin due to its distant location from the chromophore region; hence binding through this group cannot be

detected with the help of optical measurements. The only possible way binding through this group could affect the optical properties is due to anchoring of the amino groups on the nanotube binding site and self association of the planar regions of the molecules resulting in quenching of fluorescence; which is observed. Although protonated amino groups have been emphasized as the binding groups and a key component in release of the drug as shall be discussed in the following sections, other reactive sites on doxorubicin molecule should not be neglected.

Fluorescence measurements of doxorubicin adsorbed on the nanotube surface could provide additional information about the binding mechanism. Figure 4.6 shows the solution spectra of pure doxorubicin and doxorubicin adsorbed on the nanotube surface. It is interesting to note that the lower shoulder peak at 560 nm is blue shifted for the doxorubicin adsorbed on the nanotube as compared to pure doxorubicin. The shoulder peaks represent the photon emission followed by  $n \rightarrow \pi^*$  transition during absorption and is associated with oxidation state of the oxygen atoms in the chromophore<sup>4</sup>. A blue shift of this peak could be attributed to binding of the quinone oxygen to under coordinated titanium atoms. This shows that not only the amino group of the doxorubicin molecules, but the quinone region could also help in binding. For quantitative estimate of adsorbed doxorubicin refer to appendix I.

Fluorescence spectra for doxorubicin adsorbed on nanotube surface thus suggests that quenching of fluorescence is due to self association of doxorubicin molecules as a result of binding through either the amino group or the quinone region of the molecule. The blue shift of the lower shoulder peak could thus be attributed to possible binding through the quinone region. Although enough evidence has not been found for binding through the amino group,

we will find out the crucial role it could play in the desorption of doxorubicin from the nanotube surface.

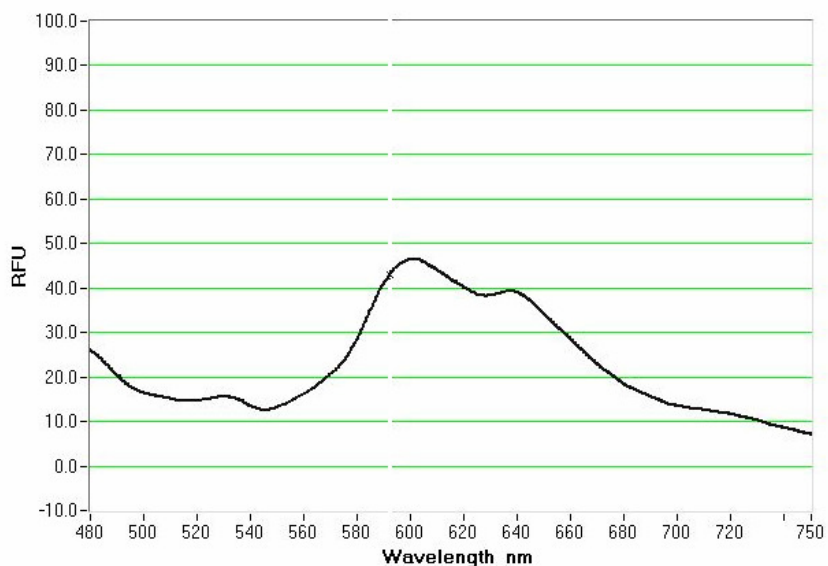
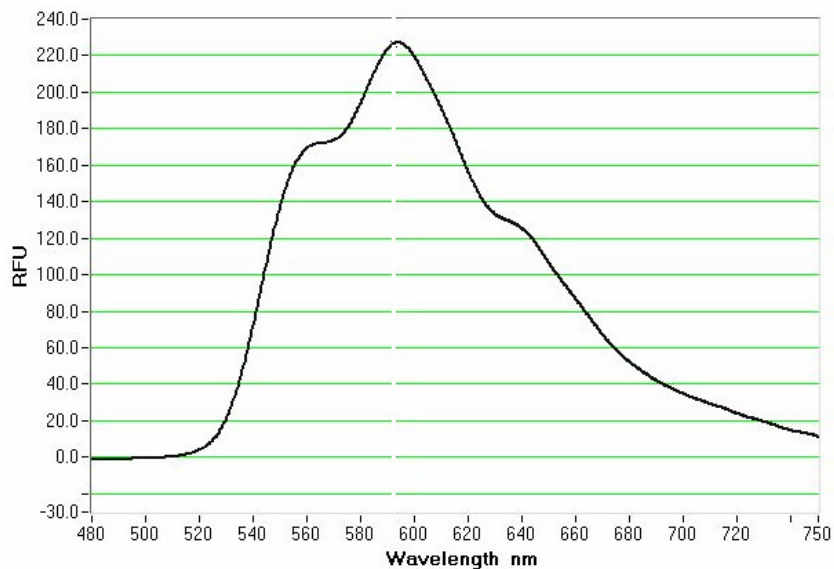


**Figure 4.6** Fluorescence spectra of free doxorubicin in solution (top) and doxorubicin adsorbed on the nanotube surface (bottom). A blue shift in the 560 nm peak corresponding to  $n \rightarrow \pi^*$  transition is due to protonation of the quinone group on the doxorubicin molecule. Doxorubicin binds to the nanotube surface through the quinone group.

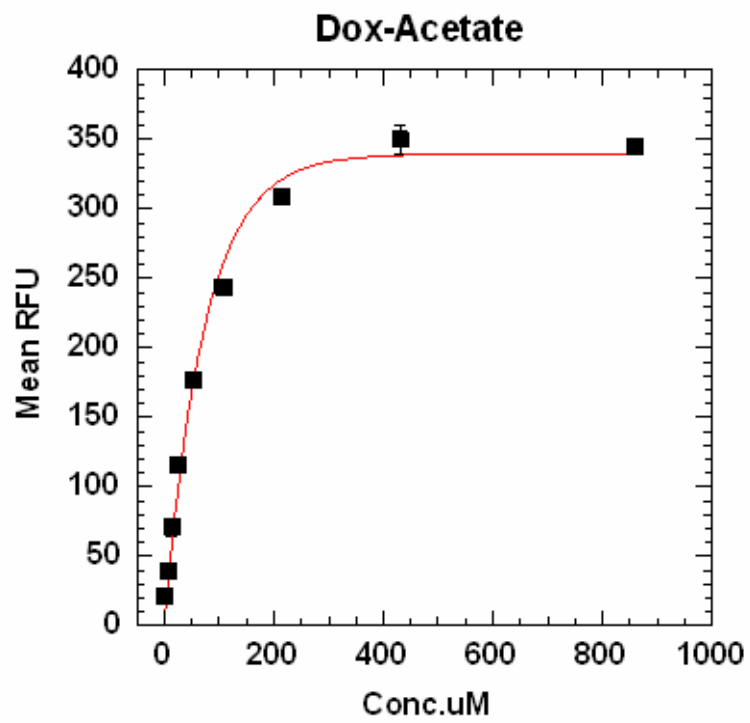
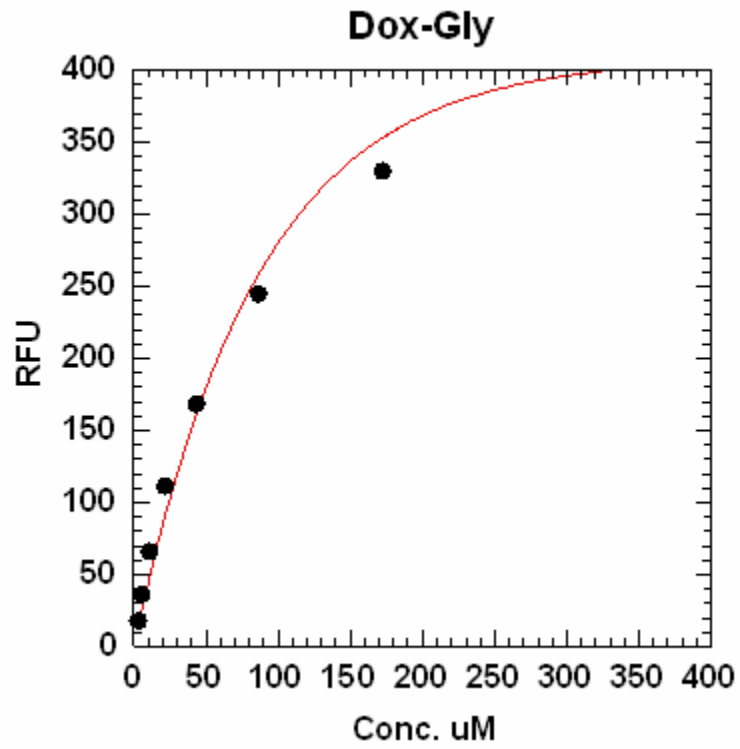
#### 4.3.2 Emptying the Nanotube Container – Releasing the Drug:

It is crucial to determine the desorption/release condition of doxorubicin from the nanotube surface as these shall be used for drug delivery under physiological conditions. All the release experiments were conducted at a physiological temperature of 37°C. Three different types of buffers were used for the release experiments. These are the Glycine buffer at a pH of 3.4, Acetate buffer at a pH of 5.7 and Phosphate Buffer Saline (PBS) at a pH of 7.4. All the buffer solutions are used at a concentration of 150 mM.

50 mg of Nanotube-adsorbed-doxorubicin were resuspended in a centrifuge tube with a buffer volume of 50 ml at a final doxorubicin concentration of 40 µg/ml. The centrifuge tube was fixed on a rotator in an oven at 37°C for homogeneous release. 200 µl of the buffer solution was then sampled out at regular intervals over a period of 72 hours. The sampled solution was centrifuged at 12000 rpm for 2 minutes to separate the free drug released into the solution from the drug adsorbed on the nanotube surface. The top solution was then used to measure the fluorescence to determine the free drug concentration released into the buffer. Free drug released was measured up to 72 hours for all the three buffers.

Fluorescence was measured during the release experiments to determine the concentration of doxorubicin. 2 µl of the sample volume was used for measurements on the Nanodrop Fluorospectrophotometer ND-3300. The sample is placed on a sample platform about the size of a pin head and a pedestal arm of the instrument is lowered to touch the sample platform and form a capillary. UV-Vis light of 400-700 nm is passed through the capillary column and fluorescence is measured. Doxorubicin has different solubility in three buffers used for the release experiments. Hence, fluorescence vs. concentration calibration

curves were plotted for the three buffers as shown in figure 4.7 and these plots were used to quantify the free doxorubicin.



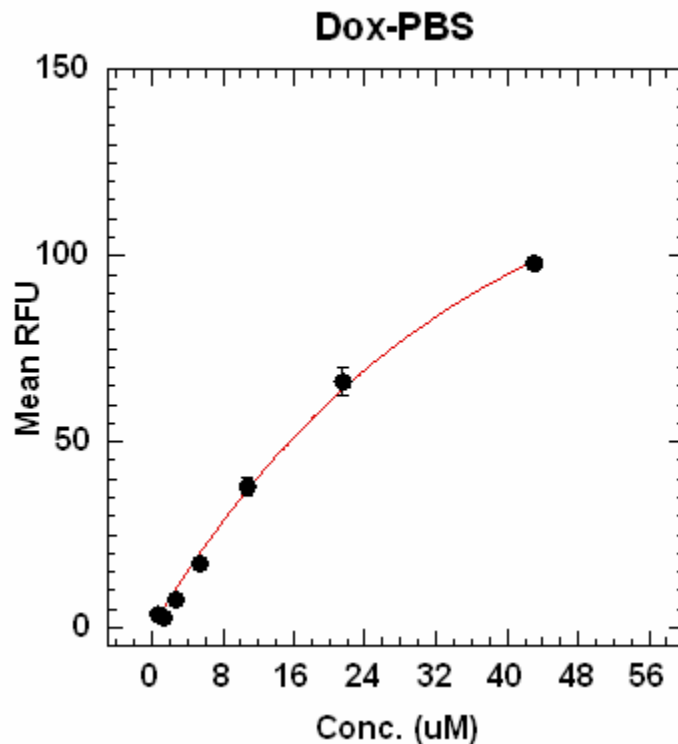


**Figure 4.7** Calibration curves of Doxorubicin in Glycine, Acetate and PBS buffers.

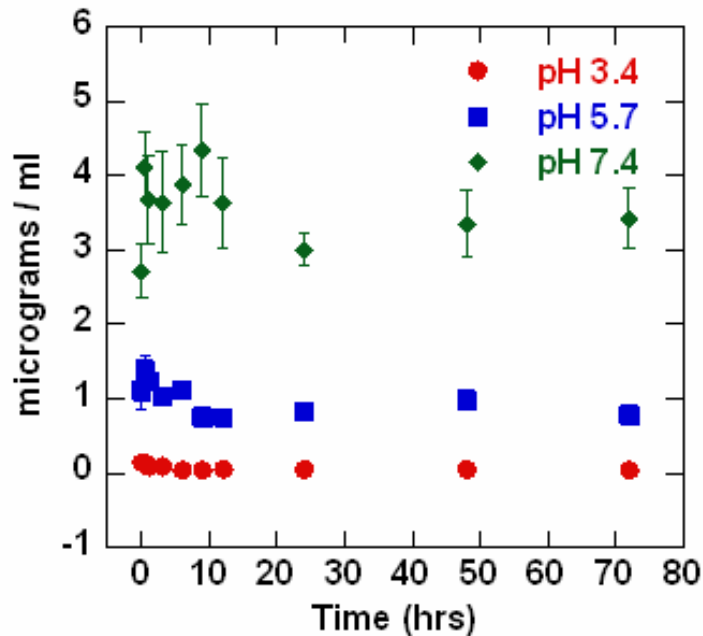
As discussed in the adsorption mechanism of doxorubicin, the lower shoulder peak of adsorbed doxorubicin is blue shifted as compared to pure doxorubicin. This was attributed to protonation of quinone oxygen in doxorubicin upon adsorption on nanotube surface. Doxorubicin released in the buffer solution after desorption regain the original peak position providing a direct evidence for deprotonation of the quinone oxygen. Thus, fluorescence makes a clear distinction between the adsorbed doxorubicin and free doxorubicin.

Figure 4.8 shows the comparison of the release of doxorubicin in three different buffers. The concentrations are obtained from the fluorescence measurements and the calibration plots for the respective buffers. PBS shows the maximum amount of free drug released into the solution. Acetate and glycine show negligible quantities of free drug

released. The differences can be explained clearly based on the dissociation of the drug molecules under different pH conditions as shall be discussed in the following section.

It is interesting to note the initial hump in the levels of doxorubicin in PBS after few hours which finally saturates to a concentration of 3-4  $\mu\text{g/ml}$ . Doxorubicin is soluble in PBS at concentrations much greater than these values. However, chemical equilibrium between the adsorbed molecules and the surrounding solution limits the free drug released. Only 10% of the adsorbed doxorubicin is thus released. The instantaneous release of doxorubicin in PBS could be attributed to a common phenomenon called burst effect observed in other nanoparticle carrier systems. This effect is usually associated with the change in temperature. However pH specific response in this system suggests that temperature is not the only contributing factor to release.

To confirm the pH-specific release, a control experiment was carried out. 50 mg of nanotube-adsorbed-doxorubicin was resuspended at a final doxorubicin concentration of 40  $\mu\text{g/ml}$  in water at 37°C, the same medium as was used for adsorption. Fluorescence measurements show no release in water and validates the pH specific response of the desorption process.



**Figure 4.8** Free doxorubicin concentrations released from nanotube-doxorubicin conjugates (dox. equivalent conc. 40 $\mu$ g/ml) in glycine (pH 3.4), acetate (pH 5.7) and PBS (pH 7.4) buffer at 37 $^{\circ}$ C as a function of time. PBS shows maximum release ~10% of doxorubicin on the nanotube surface

#### 4.3.2.1 Release Mechanism:

Several nanoparticle carriers used for doxorubicin delivery to cancer cells employ different strategies for the release of the drug. These include disruption of targeted polymer micelles by hydrolysis and release of doxorubicin at acidic pH inside structures called as endosomes or lysosomes of the cancer cells. Others take advantage of pH sensitive bonds such as hydrazine between doxorubicin and nanoparticle carriers cleaved by enzymes in the endosomes.

Doxorubicin adsorbed on the nanotube surface show pH dependent release. Titania nanotubes show preferential release of doxorubicin in PBS at a pH of 7.4. The pH specific release can be clearly explained based on the physical chemistry of the doxorubicin

molecule. The amino group on doxorubicin has a pKa of 7.5. pKa of an acid is related to the pH of the solution by the following Henderson-Hasselbalch equation.

$$pH = pK_a - \log \frac{[HA]}{[A^-]} \quad (4.1)$$

Where, [HA] is the un-dissociated form of the acid

[A<sup>-</sup>] is the deprotonated anion

It can be deduced from this expression that:

when the acid is 1% dissociated, [HA]/ [A<sup>-</sup>] =100, pH = pK<sub>a</sub> - 2

when the acid is 50% dissociated, [HA]/ [A<sup>-</sup>] =1, pH = pK<sub>a</sub>

when the acid is 99% dissociated, [HA]/ [A<sup>-</sup>] = 0.01, pH = pK<sub>a</sub> + 2

Thus in the PBS solution at pH=7.4 which is close to pKa=7.5 of the amino group, 50% of the groups should dissociate due to deprotonation and 50% of adsorbed doxorubicin should be released into the solution. Concentration of the free drug released however is only 10% of the adsorbed drug. This could be either due to the reasons of chemical equilibrium between the adsorbed doxorubicin and free doxorubicin in the solution or the saturation of the solution and lack of proper sink conditions for additional release.

Doxorubicin on the nanotube surface is in complete equilibrium with doxorubicin in the PBS solution at a concentration of 3-4 µg/ml. These concentrations are well below the solubility limit for doxorubicin and the solution could dissolve more drug molecules. However, adsorbate materials determine the quantity of drug molecules released and an equilibrium condition exists across the adsorbate/aqueous interface. Equilibrium concentration also depends on the stability of the structures carrying the drug molecules and

the nature of bonds involved in the adsorption of these molecules. Structures programmed to self destruct at a specific pH could release excess drug molecules; concentrations much higher than observed in this study. Titania nanotubes are stable structures and do not degrade like some of the polymer carriers. Thus the nanotubes retain excess doxorubicin and provide an ideal platform for slow release. Proper sink conditions are however required to further characterize the drug release and estimate the total doxorubicin quantity that could be put to therapeutic use. Ideally the highest concentration of released drug should be below 10% of its solubility in the solution for fulfillment of sink conditions.

An experiment was performed to create sink conditions for sustained release of doxorubicin and to determine the total quantity of drug released. Nanotube-adsorbed-doxorubicin was resuspended in a 15 ml tube with a buffer volume of 10 ml at a final doxorubicin concentration of 0.2 mg/ml. The tube was fixed on a rotator in an oven at 37°C for homogeneous release. After 5 minutes, the tube was centrifuged at 3000 rpm for 2 minutes to separate most of the nanotubes with the adsorbed doxorubicin from the free doxorubicin. The buffer solution with the free drug is emptied out from the tube. 200 µl of this buffer solution was transferred to a 1.5 ml centrifuge tube. The tube was again centrifuged at 12000 rpm for 2 minutes to separate any residual nanotube structures adsorbed with doxorubicin. The top solution was used to measure the fluorescence to determine the free drug concentration released into the buffer. The 15 ml tube containing the nanotube with the remaining adsorbed doxorubicin was resuspended in a fresh buffer solution of the same volume. The procedure is repeated for 15 times and the free drug concentration is recorded every time. This gives us an estimate of the total quantity of drug available for therapeutic use.

The concentration gradient between doxorubicin on the nanotube surface and the solution is crucial for dissolution of the drug. For every step as mentioned above, the initial concentration of free drug in the buffer solution is zero. However, the doxorubicin concentration on the surface of the nanotubes decreases over successive steps. This decreases the concentration gradient, a key component for dissolution resulting in a drop in the free drug concentration released into the buffer solution. Negligible quantity of doxorubicin is released in Glycine and Acetate buffers. The total quantities of desorbed doxorubicin molecules in the three buffers from the nanotube surface are shown in table I. 40% of the drug adsorbed on the nanotube surface is released into the PBS buffer as compared to 4% and 10% in Glycine and Acetate buffers respectively. Thus, we can conclude that a maximum therapeutic dose of doxorubicin can be desorbed from the nanotube surface at physiological pH values.

<b>Buffer</b>	<b>% Released</b>
Glycine	4
Acetate	10
PBS	40

**Table I.** Total quantity of free doxorubicin released from the nanotube-doxorubicin conjugates under sink conditions

All the concentrations reported in these experiments are based on fluorescence measurements. It is observed based on these measurements, that free doxorubicin released in acetate and glycine buffer is negligible. Chemical stability of doxorubicin in these solutions is a crucial factor in determining the optical properties. Fluorescence quenching due to self-

association of doxorubicin could also affect the optical measurements. Therefore it is important that we address these issues before concluding that a small quantity of doxorubicin is released into the solution.

Degradation studies have been done for doxorubicin molecule in the pH region 0-3.5<sup>8</sup>. The products of degradation are shown in figure 4.9. Doxorubicin degrades into doxorubicinone species which has the chromophore region intact and the sugar group. The presence of chromophore region means the degradation product is still optically active and fluorescence should be observed. Release experiments carried out in glycine and acetate buffer could possibly degrade doxorubicin. There are three possibilities after degradation:

1) doxorubicinone stays on the nanotube surface and daunosamine is released into the solution, 2) daunosamine stays on the nanotube surface and doxorubicinone is released into the solution, 3) both the degradation products are released into the solution. Absence of any fluorescence rules out the last two possibilities. Only the daunosamine portion of doxorubicin could thus be released into glycine or the entire doxorubicin molecule is intact on the surface of nanotubes. Hence, this proves that fluorescence measurements rightly establish the absence of any free drug in both glycine and acetate buffer solution.

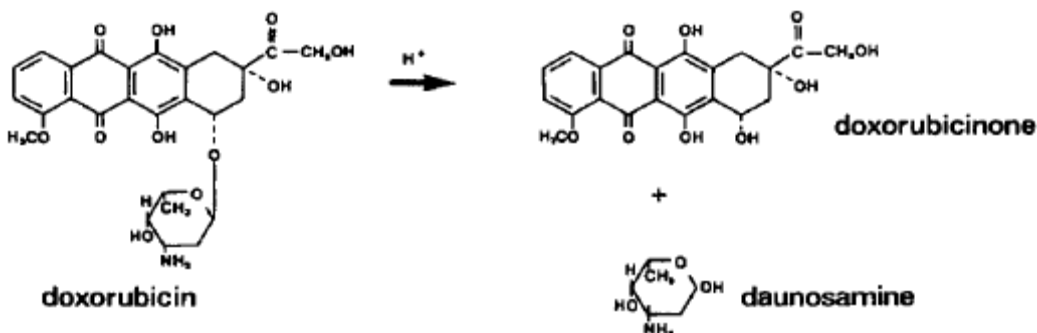


**Figure 4.9** Degradation products of Doxorubicin<sup>8</sup>

#### 4.4 Using the Device – In Vitro Experiments:

With the knowledge of the pH dependent controlled release of doxorubicin from the nanotube surface, in vitro experiments were performed to determine the effective use of nanotubes as drug delivery vehicles. Cancer cells were used for this purpose.

##### 4.4.1 Cell Culture:

HeLa (Human Cervical Cancer) cell lines were used for this study. The cells were grown in a 75 cm<sup>2</sup> flask containing DMEM (Dulbecco's Modified Eagle Medium) with 10% FBS (Fetal Bovine Serum), 1% Penicillin (antibiotic) and supplemental growth factors. Cells were incubated at 37°C in an atmosphere containing 5% CO<sub>2</sub>. Cell lines used in this study were seeded in 96 well plates for 24 hours to get a final density of 2 x 10<sup>4</sup> cells/well.

##### 4.4.2 Cytotoxicity - Background:

Cytotoxicity is a term used to define the toxic effects of a compound/material on any kind of cell. Standard set of experiments exist to determine these toxic effects. The compounds/materials used in this study are doxorubicin (anticancer drug), pure nanotubes, and doxorubicin loaded on nanotube surfaces. The cell under consideration is cancerous in nature. Toxic effects of compounds/materials in this study translate to anticancer potential. Three different cytotoxic experiments are performed to compare the effects of doxorubicin, nanotube and nanotube-doxorubicin conjugates. A range of concentrations is prepared for each of these in aqueous solution. Three separate plates were devoted for this study. Cells seeded in 96 well plates contain 100 µl of media. 10 µl of different concentrations of aqueous solution of doxorubicin, suspension of nanotube and nanotube-doxorubicin conjugate were added to cells in the three individual plates assigned to them. Untreated cells were used as controls. The treated cells along with the control were then incubated at 37°C in an

atmosphere containing 5% CO<sub>2</sub> for 12 hours. A standard assay as described in the next section was used to measure the cytotoxicity of the three compounds after 12 hours.

#### 4.4.3 MTS Assay – A Technique for Cytotoxicity Measurement:

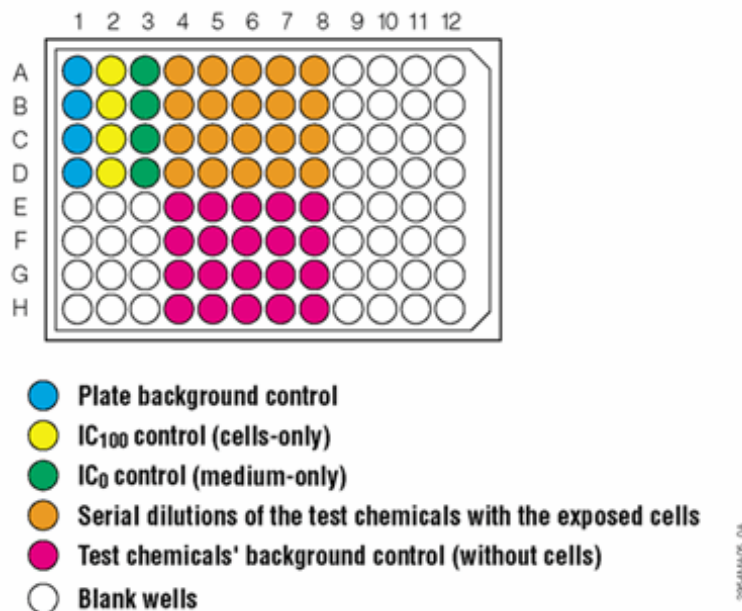


**Figure 4.10** MTS assay template for cytotoxicity study

It is a standard test procedure commonly used to test the toxic effects of industrial chemicals. It involves two reagents: 1) a well known compound (3-(4,5-dimethylthiazol-2-yl)-5-(3-carboxymethoxyphenyl)-2-(4-sulfophenyl)-2H-tetrazolium, inner salt; MTS) and 2) an electron coupling reagent, Phenazine Methosulphate (PMS). The two reagents MTS: PMS are mixed in a 20:1 ratio. For cytotoxic measurements 20 µl of the mixture is added to wells containing the treated cells and the control cells with 100µl of media. Figure 4.10 Shows a typical 96 well plate used for cytotoxicity measurements. The controls shown in the figure are also used for this study. After the addition of the reagents, the plates are incubated at 37 °C for 4 hours. Live cells produce an enzyme which reduces the reagents into a compound called as formazan which has light absorption properties. It absorbs light at a wavelength of

485 nm. Thus absorption measurements at this wavelength correspond to the number of live cells. This way we can determine the toxic effects of the compounds used in this study.

#### 4.4.4 Results & Discussion:

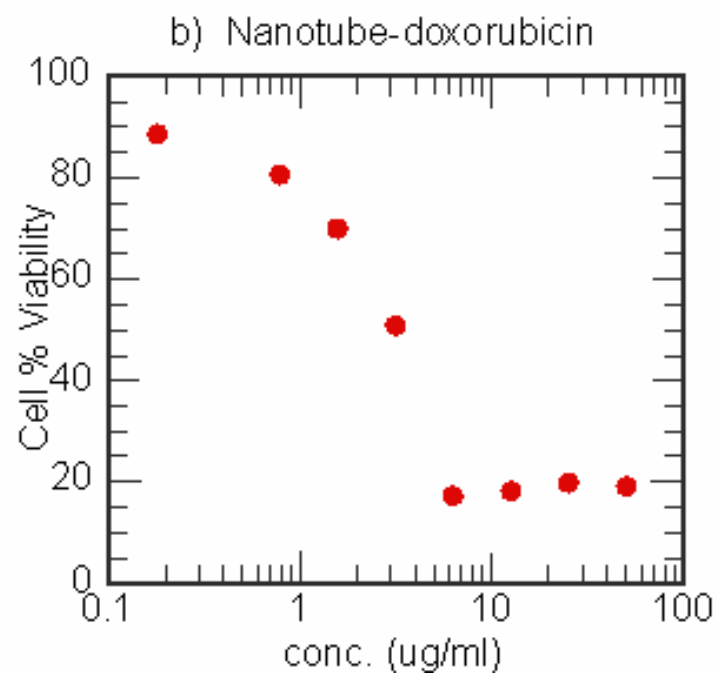
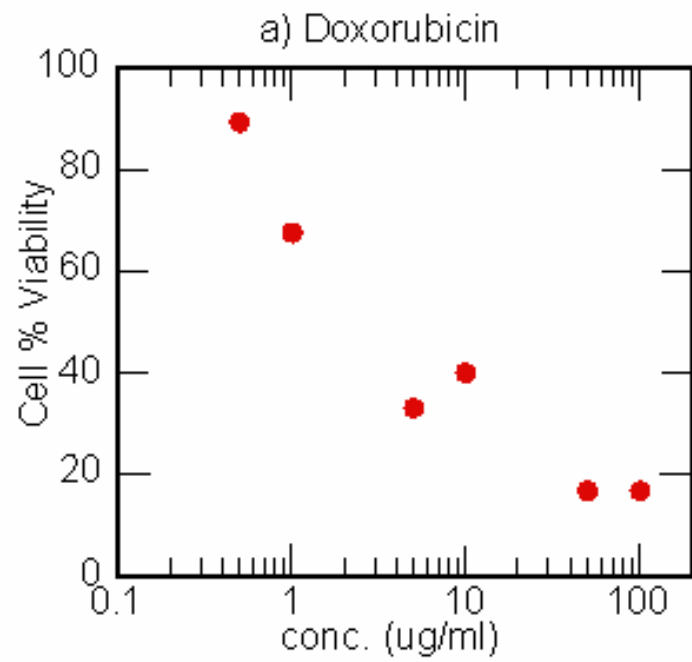
Figure 4.11 shows the comparison between the toxicity of doxorubicin, nanotube, and nanotube-doxorubicin conjugate. The X-axis shows the different concentrations of the compounds used and Y-axis represents the percent live cells corresponding to these concentrations. Triplicates of each concentration were used to obtain the average percent live cells. The percent live cell values were obtained by normalizing the absorption measurements of the treated cells over the untreated control cells.

Doxorubicin was dissolved in water for this study. Nanotube and nanotube-doxorubicin conjugates were suspended in PBS buffer before addition to the cells. After 12 hours of treatment, doxorubicin shows the cytotoxic effects as expected. Nanotube-doxorubicin conjugates show a strong cytotoxic effect and matches that of pure doxorubicin. Being able to achieve the same performance as a pure drug is remarkable. Nanotubes at all concentrations do not have any toxic effects on the cells. This confirms the inert nature of nanotubes and its potential to be used as a delivery device.

Literature values for toxicity of doxorubicin vary from 0.1-8  $\mu\text{g/ml}$  for different cell types<sup>9,10</sup>. It is important to note here that doxorubicin, when added to the cell, part of it enters the cell while the remaining drug is in the extra cellular region. Considerable effort has been made before in trying to understand the mechanism of cytotoxicity of doxorubicin. Research suggests that both intra cellular and extra cellular doxorubicin are responsible for cytotoxicity of the drug<sup>11</sup>. It was confirmed through experiments that no matter how much drug is present inside the cell, there must also be extra cellular doxorubicin concentration available for cytotoxicity. Binding of the drug molecules to the cell surface triggers a signaling pathway

for DNA damage. The internalized drug molecules subsequently intercalate with the DNA and thus the cytotoxic effect.

We would expect nanotubes to release a fraction of doxorubicin, around 10% of the adsorbed doxorubicin in the extra cellular region based on the release experiments in PBS. This extra cellular concentration could trigger the signaling pathway for DNA damage. Internalized nanotubes containing excess doxorubicin could interact with the DNA and damage the cell functioning. The observed toxic effect of nanotube-doxorubicin conjugate is thus a combination of fractional extra cellular drug release and an effective dose released inside the cell. We, thus have a delivery vehicle that carries an effective dose of doxorubicin. The key feature of this device is that it releases an extra cellular dose of drug required for cytotoxic effect and effectively transports a toxic dose in the intra cellular compartment.



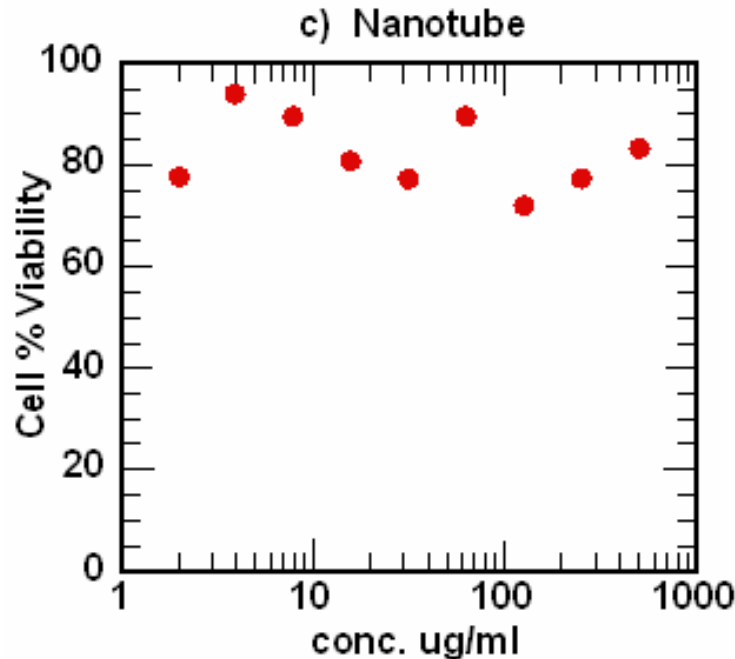


**Figure 4.11** Cytotoxic effect of a) doxorubicin, b) nanotube-doxorubicin conjugates and c) pure nanotubes on HeLa cells after 12 hrs of treatment. Doxorubicin and nanotube-doxorubicin conjugates show similar toxic effects. Note that the x-axis in b) represents doxorubicin equivalent concentration. Pure nanotubes show high % live cells and are not toxic. MTS assay was used to obtain the cell viability data.

#### Nanotube cell Interaction:

It would be interesting to obtain more information on the kind of interaction between the cells and the nanotube. A Zeiss Confocal microscope is used to image the nanotubes and the cells. Separate experiments were conducted for imaging cells treated with nanotubes. Cells were grown in 96 well plates and the same media was used as previous experiments. Fluorescein molecules were attached to the surface of nanotubes through amine functional groups. These molecules show fluorescence at ~520 nm, and assist in locating the nanotubes with respect to the cell. Cells were treated with nanotubes at a concentration of 0.1 mg/ml and incubated for 12 hours and 37°C. After incubation Trypsin (enzyme) is used to detach the cells from the surface of the well and transferred to centrifuge tubes. Cells were then spun

down using a centrifuge to obtain a pellet. The pellet containing the cells was then used for imaging.

A 520 nm fluorescence filter was used to image the cells across different sections. One of the cross-sections of the cell (figure 4.12) shows the nanotubes distributed inside the cell. It is interesting to note that most of the nanotubes are inside the cell. Imaging at different cross-sections confirmed that the nanotubes were indeed taken up by the cells and not just bound to the surface of the cells.

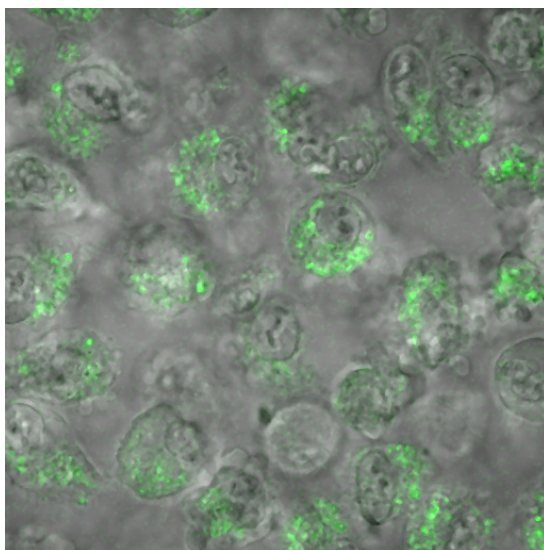


**Figure 4.12** Cross-section of HeLa cells treated with pure nanotubes. Green spots are fluorescein molecules attached to the nanotube surface. Nanotubes are internalized by cells and localized in the cytoplasm.

#### 4.5 Conclusion:

The potential of titania nanotubes as a vehicle for targeted drug delivery, for anticancer treatment is explored. Titania nanotubes used for this application are delaminated form of the raw material anatase nanoparticles which have a layered structure.

Under-coordinated atoms due to delamination are active sites for efficient adsorption of the anticancer drug, Doxorubicin, (4 wt% of the nanotubes) to form nanotube-doxorubicin conjugates. Under coordinated titanium atoms and bridging oxygen atoms are active sites on the nanotube surface for binding of Doxorubicin. Doxorubicin binds to the nanotube surface at these active sites through its protonated amine group on the glycoside. A blue shift of the peak centered at 560 nm, in the fluorescence spectra of nanotube-doxorubicin conjugates as compared to free doxorubicin, suggests another binding site on drug molecule corresponding to the quinone region.

3-4  $\mu\text{g/ml}$  of Doxorubicin is released from the nanotube-Doxorubicin (40  $\mu\text{g/ml}$  equivalent doxorubicin) conjugates in a phosphate buffer at physiological pH of 7.4 as compared to  $\sim 0$   $\mu\text{g/ml}$  in Glycine at pH 3.4 and  $\sim 1$   $\mu\text{g/ml}$  in Acetate buffer at pH 5.7. The release is determined by  $\text{pK}_a$  of the amine group of doxorubicin, due to deprotonation of amines. Under sink conditions, used to determine the total therapeutic dose available, 40% adsorbed drug was released at a pH of 7.4, as compared to 4% and 10% at pH values of 3.4 and 5.7 respectively. Nanotube-Doxorubicin conjugates show a controlled release at a physiological pH and temperature, and are tested in vitro in HeLa cell lines (Human Cervical Cancer).

In vitro experiments of nanotube-Doxorubicin conjugates and the free drug show that the conjugates have cytotoxic effects comparable to the free drug. Nanotubes, with large

surface area, strong adsorption properties, and pH sensitive release can be used as a drug delivery vehicle and provide alternative solution to polymeric materials with limited payload potential and degradation problems.

This study highlights the potential of nanotubes as a drug delivery vehicle. The results encourage working in the future direction which would involve surface modification of nanotubes with the drugs loaded and the targeting molecules attached to the surface. It would be a valuable to demonstrate the release of the rest of the 60% of doxorubicin molecules still attached to the nanotube surface thereby increasing the therapeutic value of the nanotube carriers.

#### 4.6 References:

1. Dalmark, M. & Storm, H.H. A Fickian Diffusion Transport Process with Features of Transport Catalysis - Doxorubicin Transport in Human Red-Blood-Cells. *Journal of General Physiology* **78**, 349-364 (1981).
2. Yuan, X.Y., Guo, D.S. & Zhang, M. The influence of Cu(II), Mg(II) on the binding of adriamycin with DNA and the study on their interaction mechanism. *Spectrochimica Acta Part a-Molecular and Biomolecular Spectroscopy* **63**, 444-448 (2006).
3. Missirlis, D., Kawamura, R., Tirelli, N. & Hubbell, J.A. Doxorubicin encapsulation and diffusional release from stable, polymeric, hydrogel nanoparticles. *European Journal of Pharmaceutical Sciences* **29**, 120-129 (2006).
4. Coyle, J.D. *Introduction to Organic Photochemistry*, (John Wiley & Sons Ltd, 1986).
5. Abraham, S.A. et al. Formation of transition metall-doxorubicin complexes inside liposomes. *Biochimica Et Biophysica Acta-Biomembranes* **1565**, 41-54 (2002).
6. Rodriguez, R., Blesa, M.A. & Regazzoni, A.E. Surface complexation at the TiO<sub>2</sub> (anatase) aqueous solution interface: Chemisorption of catechol. *Journal of Colloid and Interface Science* **177**, 122-131 (1996).
7. Mogilevsky, G. et al. Layered Nanostructures of Delaminated Anatase: Nanosheets and Nanotubes. *J. Phys. Chem. C* **112**, 3239-3246 (2007).
8. Beijnen, J.H., Wiese, G. & Underberg, W.J.M. Aspects of the Chemical-Stability of Doxorubicin and 7 Other Anthracyclines in Acidic Solution. *Pharmaceutisch Weekblad-Scientific Edition* **7**, 109-116 (1985).
9. Sampath, J. et al. Human SPF45, a splicing factor, has limited expression in normal tissues, is overexpressed in many tumors, and can confer a multidrug-resistant phenotype to cells. *American Journal of Pathology* **163**, 1781-1790 (2003).
10. Pechar, M., Braunova, A., Ulbrich, K., Jelinkova, M. & Rihova, B. Poly(ethylene glycol) - Doxorubicin conjugates with pH-controlled activation. *Journal of Bioactive and Compatible Polymers* **20**, 319-341 (2005).
11. Gerweck, L.E., Kozin, S.V. & Stocks, S.J. The pH partition theory predicts the accumulation and toxicity of doxorubicin in normal and low-pH-adapted cells. *British Journal of Cancer* **79**, 838-842 (1999).

## CHAPTER 5

### Introduction to Surlyn<sup>®</sup>

#### 5.1 Surlyn: An Intriguing Material

Surlyn<sup>®</sup> is the trade name of a specialty polymer made by DuPont, that belongs to a class of polymer materials called ionomers. Ionomers are semicrystalline materials which have intriguing mechanical and viscoelastic properties<sup>1-3</sup>. These properties are responsible for the phenomenon of self healing observed in Surlyn. This phenomenon is demonstrated by the closing of a hole in the sheet of Surlyn left behind by the penetration of a bullet<sup>4</sup>. It involves both elastic and time dependent recovery. The process being time dependent in nature, it is important to understand the changes in the physical properties of the material as a function of aging. Surlyn by itself also shows changes in the mechanical properties after cooling from the melt and aging at room temperature.

Physical properties are governed by the microstructure of the ionomer; hence in this chapter we will first briefly discuss the structure of Surlyn. Then we will see how these structures affect the viscoelastic and mechanical properties on aging. Finally, structural relaxations measured as a function of aging time by other groups using macroscopic techniques are discussed.

## 5.2 Structure of Surlyn:

### 5.2.1 Composition:

Ionomers are reduced salts of polymer acids. Cations are used to neutralize the polymer acids and form the salt. A wide range of ionomers exist based on the polymer acids and the cations used for neutralization<sup>5</sup>. Polymer acids are made of alkene backbone chains which have attached acid groups as side chains. One of the widely studied ionomers is neutralized ethylene/methacrylic acid (E/MAA) copolymer, known as Surlyn<sup>®</sup>.

Current study focuses on Surlyn<sup>®</sup> 8920 (E-0.054MAA-0.6Na) which contains 5.4 mol% MAA, and is 60% neutralized by sodium. Ethylene forms the backbone chain, and methacrylic acid is the side chain attached to the backbone. Figure 5.1 shows the schematic representation of the composition of Surlyn<sup>®</sup> 8920.

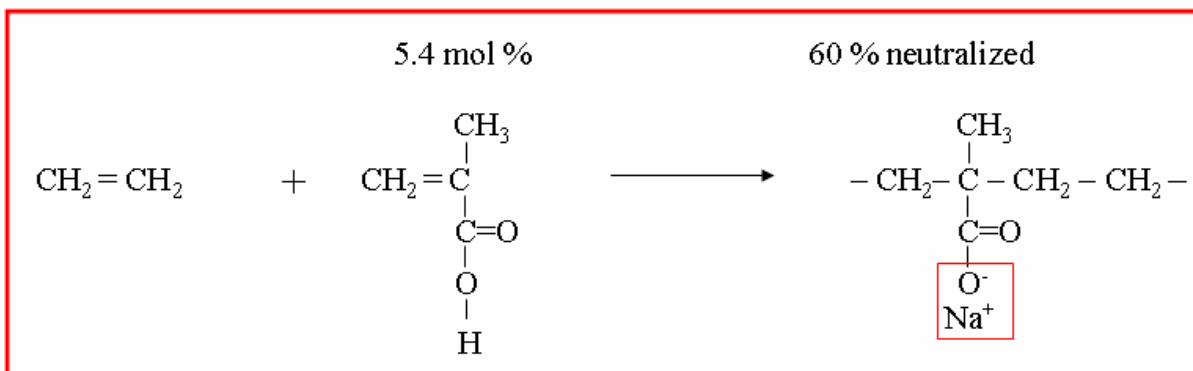


**Figure 5.1** Schematic representation of Surlyn<sup>®</sup> 8920

### 5.2.2 Morphology - Crystallites and Ionic Aggregates:

It is generally recognized that the structure of Surlyn<sup>®</sup> is heterogeneous<sup>6</sup>. It can be described by four regions; primary crystallites, secondary crystallites, ionic aggregates and the amorphous matrix as shown in figure 5.2.

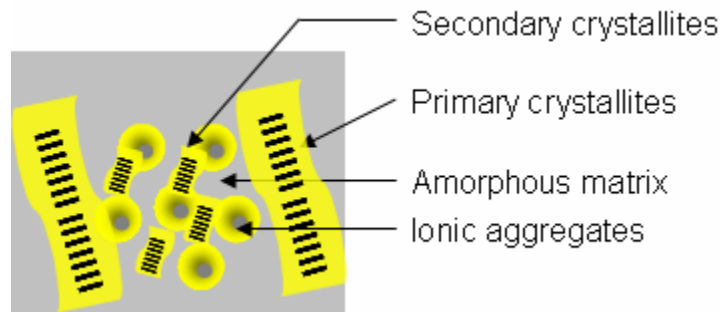


**Figure 5.2** Structure of Surlyn

Primary crystallites are made of the polyethylene chains in the ionomer. These are thick crystalline structures, and contribute significantly to the bulk modulus of the ionomer. It is due to the primary crystallites that ionomers have a semicrystalline nature.

Secondary crystallites are thinner than the primary crystallites, but made of the same polyethylene species. Secondary crystallites play an important role in the time dependent changes in the mechanical properties of the ionomer, which will be discussed later.

Ionic aggregates are much smaller structures as compared to the crystallites, and are formed because of the neutralization of methacrylic acid side chains. The side chains of acids self-associate around the cations due to electrostatic interactions. These ionic aggregates are attached to the polymer backbone chain, and act as reversible cross-linkers. Ionomers show interesting mechanical properties due to the presence of ionic aggregates in the polymer

matrix<sup>3</sup>. Flow and mechanical properties can be altered significantly by varying the acid content, cation concentration, and cation type (different size and valence states). Different grades of Surlyn are available based on the cations used for neutralization such as Na, Zn, K, etc<sup>6</sup>.

The matrix of the ionomer is made of the amorphous region, which has a glass transition temperature lower than the unneutralized acid copolymer. This region is ion-poor because of the participation of the MAA groups in the formation of ionic aggregates, and therefore has a lower  $T_g$ .

Differential scanning calorimetry (DSC) of Surlyn® 8920 exhibits two endothermic peaks as shown in Figure 5.3 (green curve). The peak at temperature  $T_{m1} = 85^\circ\text{C}$  corresponds to the melting of primary crystallites. In addition, an endothermic peak at  $T_{m2} = 55^\circ\text{C}$  was also observed which corresponds to the melting of secondary crystallites.

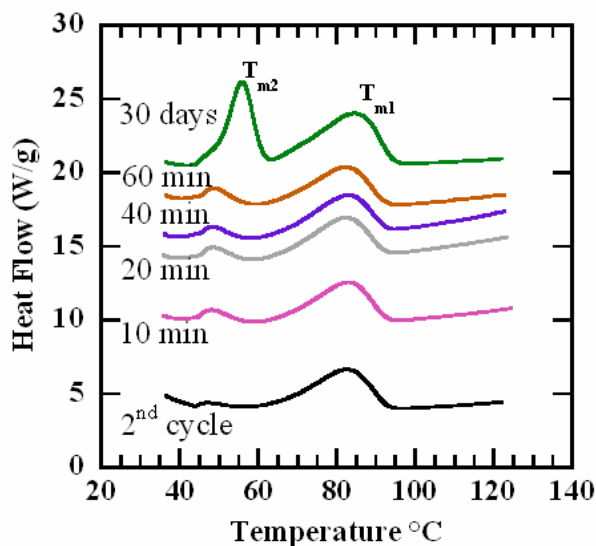


**Figure 5.3** DSC spectra of Surlyn

### 5.2.3 Structure Formation – A Dynamic Process:

The fascinating aspect of the properties of Surlyn is the dynamic nature of the structures during formation as the ionomer is cooled from the melt state to room temperature (RT), and how these structures affect the mechanical properties with aging. We shall first look at the process of formation of these structures followed by the influence of ionic aggregates on the structures.

As the ionomer is cooled from the melt, primary crystallites are formed first. In the amorphous regions of the ionomer, neutralized MAA forms ion-rich regions of ionic aggregates, such as  $\text{-O}^-\text{-Na}^+$  in Surlyn<sup>®</sup> 8920. The ionic aggregates are surrounded by a region with restricted chain mobility as compared to the ion-poor amorphous region<sup>7</sup>. Ionic aggregates remain stable in the melt at elevated temperatures, and the “regions of restricted mobility” raise the resistance to the flow of the polymer chains during primary crystallite formation<sup>8</sup>. This retains part of the amorphous region rich in polyethylene segments during the cooling process, and allows the formation of thinner secondary crystallites in the amorphous region after a long aging time at RT<sup>9</sup>. This is shown by the absence of the  $T_{m2}=55^\circ\text{C}$  peak in samples immediately after cooling from the melt, becomes visible after hours of aging, and fully developed after months of aging at RT. Secondary crystallites play an important role in the structural relaxation of the ionomer. These structures in combination are responsible for complex mechanical properties of the ionomer.

The effect of ionic aggregates on the formation of primary and secondary crystallites is clearly emphasized during the cooling process. Slow formation of secondary crystallites and changes in the “restricted region of mobility” around the ionic aggregates also show strong aging effects on the mechanical properties of ionomer. We will discuss the structure of

ionic aggregates in more detail, and how it affects other structures in the ionomer. Then we will discuss the aging effects on the mechanical properties of Surlyn as detected by common techniques.

## 5.2.4 Ionic Aggregates - A Key Component of Ionomers:

First we will discuss under what conditions ionic aggregates are formed, and how the glass transition of the polymer changes. This information is useful in understanding the structural relaxation and changes in mechanical properties related to the ionic aggregates. This will be followed by morphology of ionic aggregates and how they influence other crystallite structures in the ionomer.

### 5.2.4.1 Formation of ionic aggregates:

Formation of ionic aggregates is dependent on the nature of the host polymer and cationic species used for neutralization.

Host polymer with a low  $T_g$  favor the formation of ionic aggregates, however high  $T_g$  polymers have the reverse effect<sup>7</sup>. This is directly related to the freedom of movement for the ionic groups in the matrix with strong ionic associations formed in low  $T_g$  polymers. Presence of cations is not mandatory for the formation of ionic associations and it is known that even unneutralized E/MAA copolymers could form ionic associations<sup>10</sup>. This was supported by evidence of an increase in  $T_g$  of the amorphous phase with increasing MAA content<sup>6</sup>.

Upon neutralization with cations, the glass transition temperature of amorphous regions splits into two transitions, one above  $T_g$  corresponding to the order-disorder transitions in ionic aggregates and the other below but close to  $T_g$ . For convenience, these shall be named as A and B transitions respectively. A study on neutralized E/MAA copolymers showed that free MAA units from the amorphous region tend to associate with the ionic aggregates resulting in B transitions much lower than  $T_g$ . This suggests that ionic associations could form without the need for neutralization and have additive effects on the

mechanical properties of the ionomer. Cations help in the formation of strong ionic associations. Series of monovalent and divalent cations (Na, K, Li, Ca, Mg) are used for neutralization of acid groups in ionomers. Interesting differences in ionic associations are observed among different cations. For example, free MAA units in the amorphous region of Na-E/MAA ionomer show strong association with the ionic aggregates even at low neutralization levels depleting the ions in the amorphous regions. This results in splitting of  $T_g$  as mentioned before. However increasing neutralization of Zn-E/MAA demonstrates a continuous drop in the  $T_g$  of the amorphous region without any splitting. This suggests that MAA units do not preferentially associate with Zn aggregates. Thus different cations have different affinities for acid groups.

#### 5.2.4.2 Morphology of Ionic Aggregates:

Ionic aggregates are nothing but associated pairs, triplets, quartets (multiplets) based on the strength of ionic association and valence state of the cations used. Ionic aggregates are dynamic structures, as shown by NMR measurements, which have order-disorder transitions with a certain sticking coefficient between them<sup>11</sup>. In ionic aggregates, polymer acid side chains are anchored to the point of ionic association that restricts the mobility of the polymer backbone chains in the vicinity of the ionic aggregates. The mobility increases as the distance from the aggregates increases. Therefore each multiplet is surrounded by a region of restricted chain mobility as shown in figure 5.4<sup>7</sup>. Polymer chains with restricted motion will alter the flow properties significantly. The thickness of the region of restricted mobility around the ionic aggregates depends on the flexibility of the polymer backbone. The more flexible this chain is, the smaller the thickness of region of restricted mobility. The strength of the ionic association also determines the restricted mobility region. The larger the number

of multiplets is, the stronger the association is and therefore the stronger the anchoring is. Thus, the region of restricted mobility around the ionic aggregates would be large.

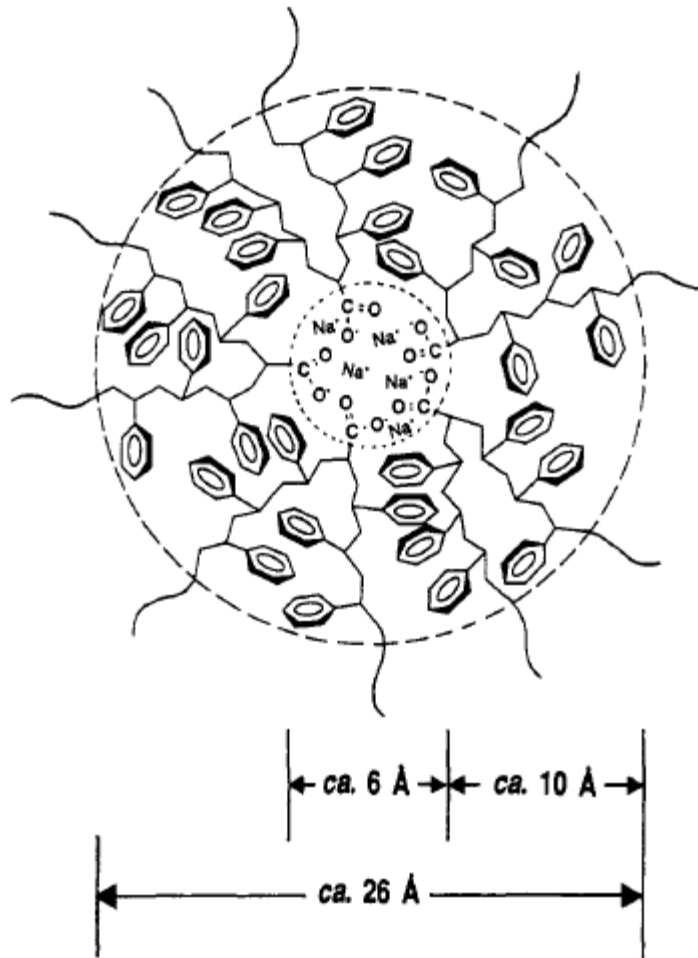


**Figure 5.4** Region of restricted mobility surrounding a multiplet in a poly(styrene-co-sodium methacrylate) ionomer<sup>7</sup>

With increasing ion content, the distance between the ionic aggregates decreases resulting in overlap of the regions of restricted mobility. Large numbers of such overlap regions could form a continuous phase which has its own  $T_g$ . These are phase separated regions called clusters. The point at which such regions start to form is not clear. Considerable differences

were found in the experimental results regarding the state of the ionic associations. In some cases experimental evidence showed the presence of clusters while in others, observations suggested ionic aggregates dispersed in the ionomer matrix. It was not clear, at what concentration the clusters were formed. Eisenberg came up with a theoretical model to account for the inconsistencies observed in the experiments, and proposed that there exists a critical ion concentration below which the cluster would cease to exist and ionic aggregates would be dispersed in the polymer<sup>10</sup>. A general condition for such structures to exist would be that the distance between the multiplets to be less than twice the thickness of the restricted mobility region. Figure 5.5 A shows the relative chain mobility around the multiplet which is less than that of the bulk. These regions of restricted mobility act as crosslink across the polymer and increase the  $T_g$  of the material. Figure 5.5 B shows a number of multiplets close together forming a contiguous region of restricted mobility phase separated which has its own  $T_g$ .

Although the formation of clusters in the system under consideration has not been investigated, evidence of the formation of regions of restricted mobility has been demonstrated in the next chapter as we study the aging effects on mechanical properties.

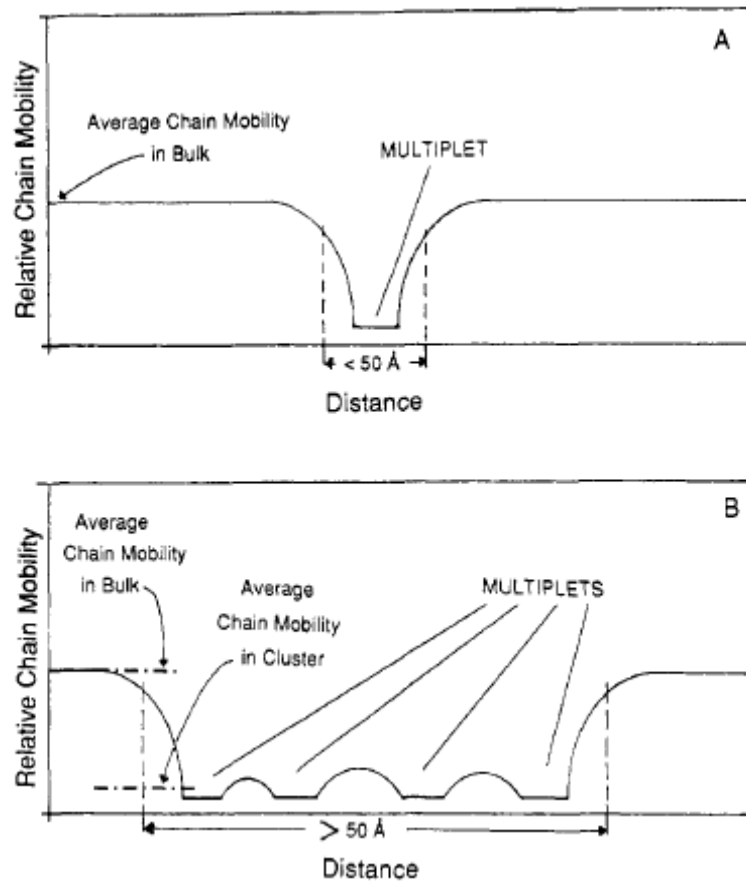


**Figure 5.5** Schematic representation of chain mobility:  
 (A) in the vicinity of an isolated multiplet;  
 (B) in the region of clustered multiplets<sup>7</sup>

### 5.2.4.3 Influence on crystallites:

As mentioned before, during the cooling process of the ionomer from the melt, ionic aggregates and regions of restricted mobility around them offer resistance to flow of the polymer chains during primary crystallization resulting in the formation of secondary crystallites. Increasing the ionic concentration would therefore directly affect the crystallinity of the ionomer.

Table II presents the effect of neutralization on volume fraction crystallinity, melting point of primary and secondary crystallites, and Young's modulus of ionomer<sup>6</sup>. Neutralization increases the resistance to flow of the polymer chains during primary crystallization, and reduces the crystallinity of the ionomer as more polyethylene chains are retained in the amorphous region. Neutralization reduces the primary crystal melting temperature only slightly, but the secondary crystallites melt at higher temperatures. Area of the primary crystallite endotherm decreases with neutralization as shown in figure 5.6. More polyethylene chains retained in the amorphous region in the form of secondary crystallites with increasing neutralization result in an increased amorphous phase modulus (E), and balance the decrease in crystallinity of the ionomer.

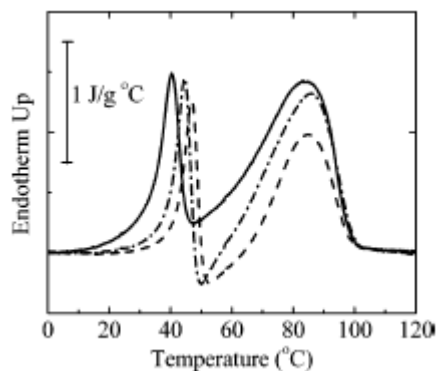


**Figure 5.6** Effect of neutralization on primary and secondary crystallites<sup>6</sup>:

DSC heating thermograms of E/MAA copolymer (22 wt % MAA) and two ionomers derived there from, all stored at room temperature for 6 days after molding: (—) 22-0Na, (— -) 22-26Na, and (— —) 22-48Na

ionomer	wt % Na	peak $T_{m1}$ , °C	peak $T_{m2}$ , °C	peak $E''$ , °C	volume fraction crystallinity $\phi_1$ (25 °C)	Young's modulus $E$ (25 °C), MPa
11.5-0Na	0	96	39	2	0.26	100
11.5-7Na	0.22	96	39	4	0.26	140
11.5-10Na	0.31	97	40	5	0.27	200
11.5-16Na	0.49	96	41	18	0.26	250
11.5-26Na	0.79	96	43	25	0.26	250
11.5-39Na	1.20	96	46	32	0.23	290
11.5-47Na	1.44	96	46	37	0.24	300
11.5-62Na	1.89	95	47	38	0.22	300
11.5-83Na	2.51	93	49	41	0.19	280
15-0Na	0	91	39	10	0.21	120
15-24Na	0.96	92	46	32	0.20	420
15-34Na	1.36	91	47	36	0.19	400
15-51Na	2.03	90	48	40	0.16	410
15-67Na	2.64	89	48	41	0.14	390
19-0Na	0	90	40	16	0.19	190
19-8Na	0.41	89	44	29	0.21	460
19-14Na	0.71	89	45	32	0.19	530
19-22Na	1.12	88	46	37	0.16	520
19-35Na	1.77	87	46	39	0.14	500
19-51Na	2.55	86	48	44	0.14	480
22-0Na	0	86	40	25	0.16	360
22-26Na	1.52	86	45	41	0.13	580
22-35Na	2.04	84	46	41	0.11	540
22-48Na	2.77	85	47	41	0.08	540
28-0Na	0	79	42	33	0.10	630
28-12Na	0.90	77	43	41	0.07	810
28-19Na	1.42	78	45	42	0.06	810
28-28Na	2.07	78	45	44	0.08	800

**Table II.** Effect of neutralization on primary crystallite and secondary crystallite melting temperature, bulk modulus of ionomer and crystallinity<sup>6</sup>

### 5.3 Mechanical Properties and Aging Effects in Surllyn: As Detected by Macroscopic Techniques:

Systematic studies have been performed to identify the effect of structural changes in the ionomer on flow and mechanical properties as a function of aging time. For better understanding of these properties, comparative studies have been conducted based on a variety of ionomer systems. Several techniques have been used to separate the individual

contributions of these structures. A standard approach is to use an instrument to measure the mechanical properties, and a technique to obtain the structural details. These procedures are used in conjunction to draw conclusions regarding the structure responsible for observed mechanical property.

Over the years of investigation of mechanical properties of ionomers, contributions due to ionic aggregates and secondary crystallites have been hard to discern. This is due to the fact that ionic aggregates split the glass transition of amorphous regions into two transitions. One is at a low temperature, usually below room temperature, and the other transition is close to the secondary crystallite melting temperature. Researchers have come up with innovative techniques to separate the two contributions to the aging effect on mechanical properties.

A group reported their work on one of the ionomers, a complex Zn & 1, 3-bis (amino methyl) cyclohexane (BAC) salt of ethylene-methacrylic acid copolymer, used Dynamic Mechanical Thermal Analysis (DMTA) and Differential Scanning Calorimetry (DSC) to separate the individual contributions to the mechanical properties<sup>3</sup>. The aim of this work was to determine the effect of formation of ionic crystallites on the mechanical properties of the ionomer. The procedure involved molding the ionomers under pressure at 160°C, and then was cooled to room temperature. Mechanical properties were measured at different aging times from few hours to several days after molding and compared with the DSC thermograms. The mechanical properties measured are storage modulus ( $E'$ ) and loss modulus ( $E''$ ). For an applied strain represented by  $\varepsilon = \varepsilon_o \sin(\omega t)$  and the resulting stress in a viscoelastic material represented by  $\sigma = \sigma_o \sin(\omega t + \delta)$  (where  $\delta$  is the phase lag between the applied stress and the resulting stress), the storage modulus is given by

$E' = (\sigma_o / \epsilon_o) \cos \delta$ , which measures the elastic energy stored in the material and loss modulus is given by  $E'' = (\sigma_o / \epsilon_o) \sin \delta$ , which measures the energy dissipated as heat, representing the viscous portion. The ionic crystallites for this system had a melting point around 55°C, and figure 5.7 shows the temperature dependence of storage ( $E'$ ) and loss modulus ( $E''$ ) aged at different times at room temperature. The value of  $E'$  increases and  $E''$  decreases below 60°C with aging, which suggests improved elastic properties with the formation of ordered ionic crystallites and decrease in the viscous properties. No change in the properties was observed above 60°C since the ionic crystallites melt above this temperature. Although, there exists a good correlation in these observations, influence of polyethylene crystallites could not be completely ruled out as pointed by another group. X-ray diffraction of the samples confirmed that no secondary crystallites were formed, and that the aging effects observed were due to ionic aggregates. Therefore a combination of different techniques was able to determine the structure responsible for the observed aging effects on mechanical properties.

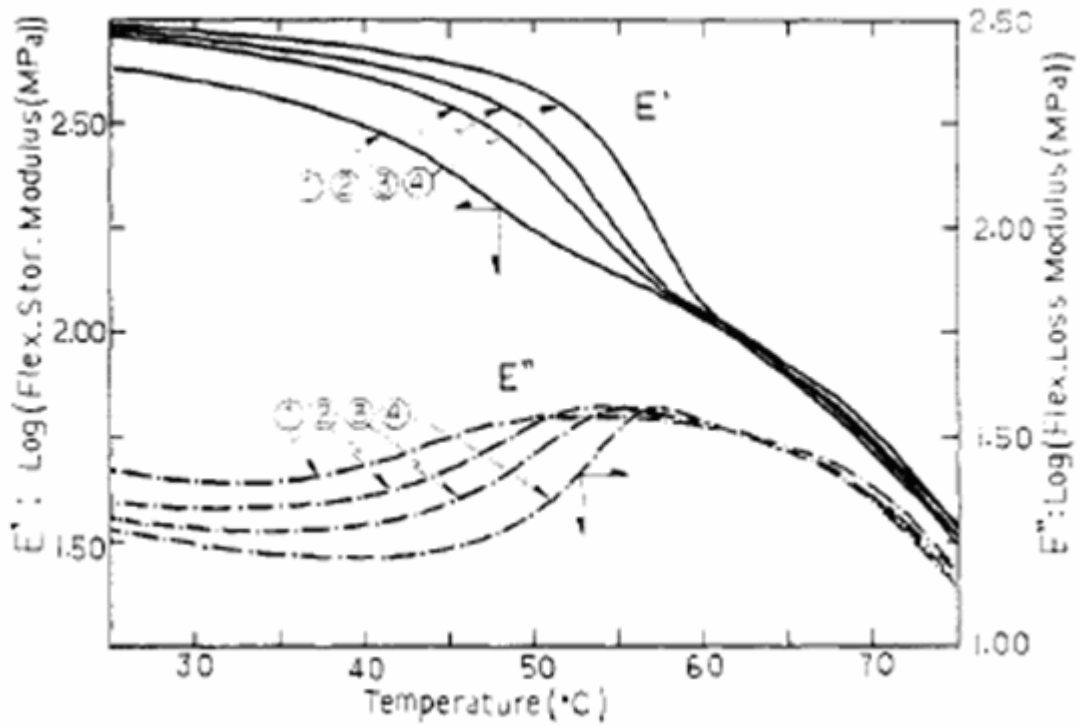


**Figure 5.7** Temperature dependence of dynamic modulus ( $E'$ ) and the loss ( $E''$ ) for the sheet of EMMA-0.6Zn-0.4BAC aged at 23°C in nitrogen. 1), aged for 0 day (3-5 h) after molding. 2), aged for 3 days after molding. 3), aged for 9 days after molding. 4), aged for 38 days after molding

However, the possibility of formation of crystallites of sizes much lower than the resolution of X-ray diffraction can not be ruled out. A better approach is required to confirm the absence of other minor contributions. Structural relaxation detected by change in the storage and loss modulus in the DMTA has contributions both from the ionic aggregates and the secondary crystallites. Interesting variations of the DMTA technique can be effectively used to separate the contribution from the structures<sup>6</sup>. One of these techniques is variable frequency DMTA as shown in figure 5.8. Storage modulus ( $E'$ ), loss modulus ( $E''$ ) and the ratio of the two modulus given by  $\tan \delta$ , which characterizes the damping ability of the material are measured at different frequencies by this method.

Structural relaxation due to ionic aggregates is frequency dependent, whereas secondary crystallite is not. An EMMA-22MAA-48Na ionomer was tested at three different frequencies as shown in figure 5.8. The location of the step drop does not change for  $E'$ ,  $E''$  and  $\tan \delta$ , and is identical to the melting point of secondary crystals ( $T_{m2}$ ). However the magnitude of this step drop decreases for  $E'$  and  $E''$  as the frequency is increased. This frequency dependence is attributed to a material in the vicinity of its glass transition; ionic aggregates in this case.

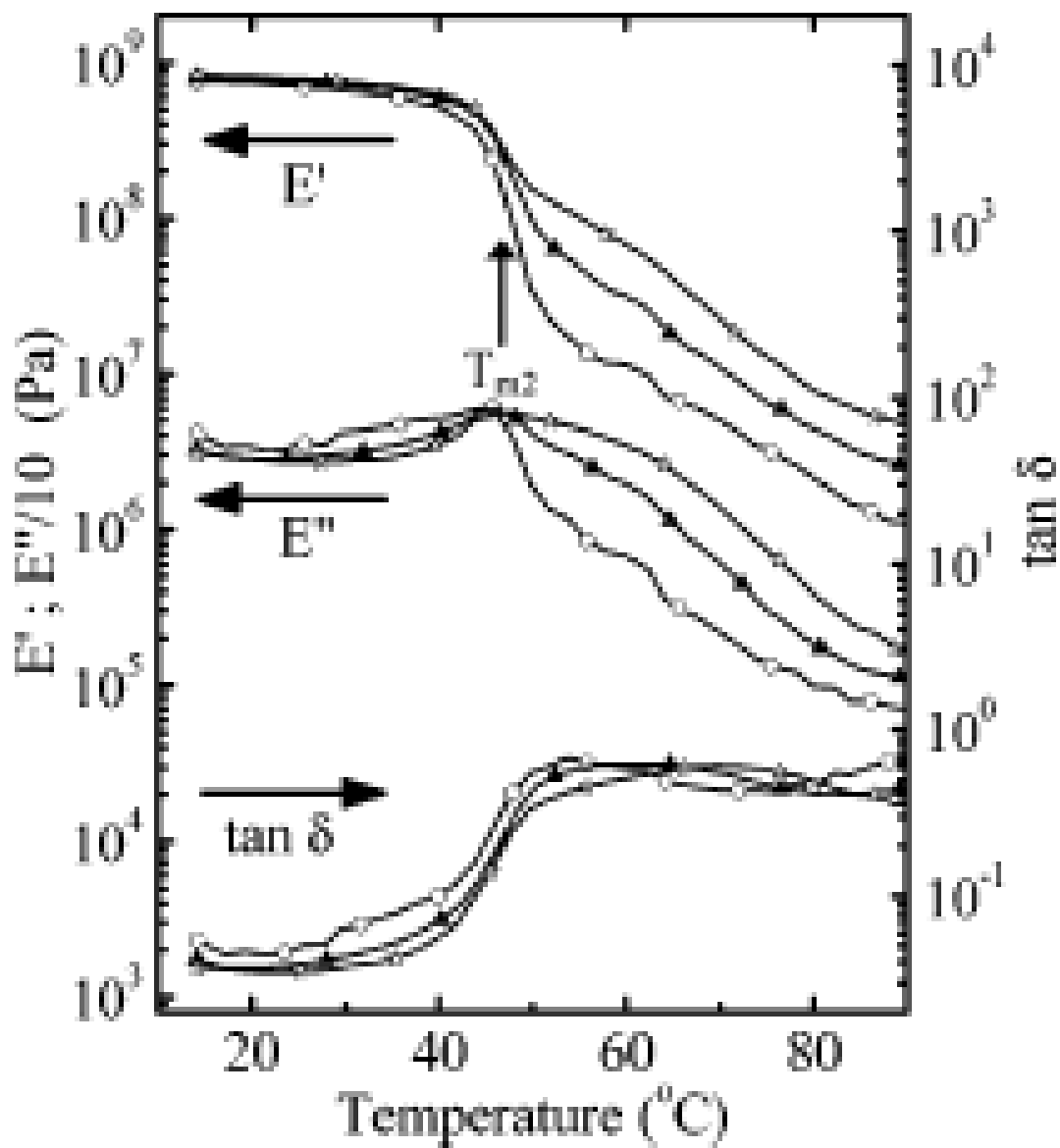


**Figure 5.8** Frequency-dependent DMTA data for ionomer 22-48Na, aged at room temperature for 6 days after molding: ( $T_{m2}$ -secondary crystallite melting temperature);  $E'$  (storage modulus),  $E''$  (loss modulus) and  $\tan \delta$  ( $E'/E'' \rightarrow$  damping ability of the material): each plot corresponds to a different frequency. ( $\circ$ ) – 0.16 Hz, ( $\blacktriangle$ ) – 1.6 Hz and ( $*$ ) – 12.7 Hz.

#### 5.4 References:

1. Eisenberg, A. & King, M. *Ion-containing Polymers, Polymer Physics*, (Academic Press, New York, 1977).
2. Eisenberg, A., King, M. & Navratil, M. Secondary Relaxation Behavior in Ion-Containing Polymers. *Macromolecules* **6**, 734-737 (1973).
3. Hirasawa, E., Yamamoto, Y., Tadano, K. & Yano, S. Formation of Ionic Crystallites and Its Effect on the Modulus of Ethylene Ionomers. *Macromolecules* **22**, 2776-2780 (1989).
4. Huber, A. & Hinkley, J.A. *Impression Testing of Self-Healing Polymers*. (National Aeronautics and Space Administration, Hampton, 2005).
5. Bonotto, S. & Bonner, E.F. Effect of Ion Valency on the Bulk Physical Properties of Salts of Ethylene-Acrylic Acid Copolymers. *Macromolecules* **1**, 510-515 (1968).
6. Wakabayashi, K. & Register, R.A. Morphological origin of the multistep relaxation behavior in semicrystalline ethylene/methacrylic acid ionomers. *Macromolecules* **39**, 1079-1086 (2006).
7. Eisenberg, A., Hird, B. & Moore, R.B. A New Multiplet-Cluster Model for the Morphology of Random Ionomers. *Macromolecules* **23**, 4098-4107 (1990).
8. Yarusso, D.J. & Cooper, S.L. Analysis of Saxs Data from Ionomer Systems. *Polymer* **26**, 371-378 (1985).
9. Loo, Y.L., Wakabayashi, K., Huang, Y.E., Register, R.A. & Hsiao, B.S. Thin crystal melting produces the low-temperature endotherm in ethylene/methacrylic acid ionomers. *Polymer* **46**, 5118-5124 (2005).
10. Eisenberg, A. Clustering of Ions in Organic Polymers. A Theoretical Approach. *Macromolecules* **3**, 147-153 (1969).
11. Jia, Y.Y., Kleinhammes, A. & Wu, Y. NMR study of structure and dynamics of ionic multiplets in ethylene-methacrylic acid ionomers. *Macromolecules* **38**, 2781-2785 (2005).

## CHAPTER 6

### Mechanical Properties of Surlyn: As Detected by a Microscopic Technique

#### 6.1 Background & Motivation:

Several macroscopic techniques have been used to study the aging effects on physical properties of Surlyn as mentioned in the previous chapter. The two physical properties of common interest are viscoelasticity which characterizes the flow behavior of the material, and mechanical properties such as modulus of elasticity which characterizes the strength of the material. Aging effects on these properties have been attributed to structure-property relationship. We know that the structure of Surlyn is complex, and thus makes the understanding of structure-property relationship a difficult task.

The structure of Surlyn is made of primary crystallites, secondary crystallites, ionic aggregates, and the amorphous region. These structures form at different times during and after cooling from the melt. Primary crystallites form immediately after cooling from the melt, whereas the secondary crystallites form at different aging time after cooling from the melt. Ionic aggregates are known to exist even in the melt, and get stronger as cooled and aged. The slow process of formation of secondary crystallites and development of stronger ionic aggregates alters the flow and mechanical properties of Surlyn with aging. Structural relaxation effects in and around these regions as they form and develop at different aging times influence the structure-property relation. Structural relaxation in and around secondary

crystallites and ionic aggregates in combination change the flow and mechanical properties as they form during and after cooling. It is important to know which structures are responsible for these changes as they are formed.

In previous studies flow properties such as viscosity, and mechanical properties such as storage modulus have been measured at different aging times to determine their influence on secondary crystallites and ionic aggregates as they develop. Most of the observations reported were at long aging times of several hours to days, and these were supported by DSC thermograms. Understanding the changes in properties at short aging times is crucial since it determines the properties at long aging times and helps us get a better insight into the structure of Surlyn. A microscopic approach is used to measure these properties at short aging times and in this chapter we shall see how different this is from the macroscopic techniques.

## 6.2 Introduction to Local Thermal Analysis (LTA) Technique:

In this study we use a microscopic technique to measure the viscoelastic and mechanical properties at short aging times of minutes to hours as compared to days to months in previous studies. The technique involves an atomic force microscope based Local Thermal-mechanical Analysis probe, which is used to measure creep response of Surlyn at short aging times after cooling from the melt. The probe is made of a micron size tip, as shown in figure 6.1, which serves as the contact point between the probe and the sample. A constant force can be applied by the tip on the sample through a cantilever system using the same principle as the atomic force microscope. The special feature of the probe is that, current can be passed through it to heat the tip and measure creep response at different temperatures. Due to the microscopic size of the tip, multiple creep response data could be obtained at different aging times from the same sample.

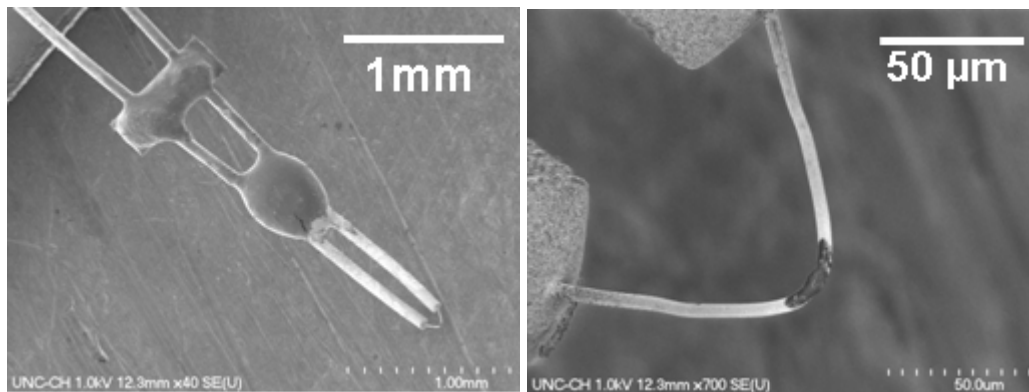


**Figure 6.1** Scanning electron microscopy image of the Local Thermal Analysis probe.

Creep response data obtained at different temperatures and aging times is characterized by a viscoelastic model. The model is used to quantify the mechanical properties such as modulus and viscosity from the creep curves as a function of aging time. In this chapter we discuss the

details of the probe, the experimental procedure to obtain the creep response characteristics, viscoelastic model to describe the data qualitatively and analysis of the structure-property relation as a function of aging.

### 6.2.1 A Micron-sized Probe for Creep Measurement:

The experiments were performed by using a  $\mu$ TA 2990 Thermal Analyzer microscope by TA Instruments. The microscope is built on an Explorer type AFM platform with added LTA features. The probe tip is made of a 5  $\mu$ m diameter Pt/ Rh wire with a nominal spring constant of 5 N/m. As shown in Figure 6.1, the leads of the Pt/Rh wire are encased inside a 75 micron diameter silver wire through which current can be applied. The temperature of the tip is calibrated through the electrical resistance of the Pt/Rh wire tip with a known standard. The LTA probe tip approaches the sample with a constant force (30-50  $\mu$ N) at a chosen probe tip temperature. The contact area of the probe and the sample is 15x5  $\mu$ m<sup>2</sup> as determined by AFM images of the sample after the experiments. Displacement of the probe after engaging the sample surface at a given force is recorded versus the engagement time over a period of 35 seconds, producing a response curve of creep at a chosen temperature.

### 6.2.2 Choosing the Probe Tip Temperature:

Differential scanning calorimetry (DSC) of Surlyn<sup>®</sup> 8920 exhibits two endothermic peaks as shown in Figure 6.2. The peak at temperature  $T_{m1} = 85^{\circ}\text{C}$  corresponds to the melting of polyethylene crystalline lamellae, the product of primary crystallization. In addition, an endothermic peak at  $T_{m2} = 55^{\circ}\text{C}$  was also observed which corresponds to secondary crystallites. This peak is absent in samples immediately after cooling from the melt and

becomes visible after hours of aging and fully developed after months of aging at RT<sup>1</sup>. In this study, creep curves were obtained at both 30°C and 70°C with one below and the other above the endothermic peak at  $T_{m2} = 55^\circ\text{C}$ . This would allow us to identify the characteristics of room temperature structural relaxation in regions surrounding ionic aggregates through their effect on viscoelastic properties.

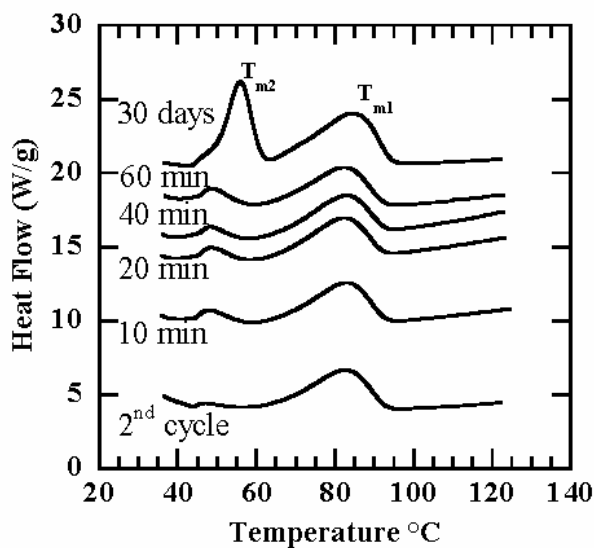


**Figure 6.2** DSC spectra of Surlyn<sup>®</sup> as a function of relaxation (aging) time. The first run is with the sample aged for 30 days at room temperature. The second cycle followed immediately after the first run. Others were run after cooling from the melt and after waiting at room temperature for certain time as indicated in the figure.

### 6.2.3 Experimental Procedure for Creep Measurement:

The sample is mounted on a metallic holder which sits on a hot stage as shown in figure 6.3. Using the hot stage, the entire sample is heated to  $110^{\circ}\text{C}$ ,  $20^{\circ}\text{C}$  above the melting temperature  $T_{m1}$  of polyethylene crystallites to erase the thermal history of the sample. The hot stage is then turned off and the sample is transferred immediately to the AFM stage that is kept at room temperature. This allows the sample to cool down to room temperature in less than 3 minutes as tested by an embedded thermocouple. Following this, the sample was subject to LTA measurements with the AFM tip to obtain a creep curve. Since the contact area between the probe and the sample is micron-sized with limited thermal effects in other parts of the sample surface, the creep measurement can then be repeated at different spots of the sample surface, each corresponding to a different aging time at room temperature. Creep curves were collected from the same sample at relaxation times of 10 min, 20 min, 40 min, 60 min, 80 min, 140 min, 200 min and 280 min after the thermal reset. Isothermal response curves are collected at given probe tip temperatures.

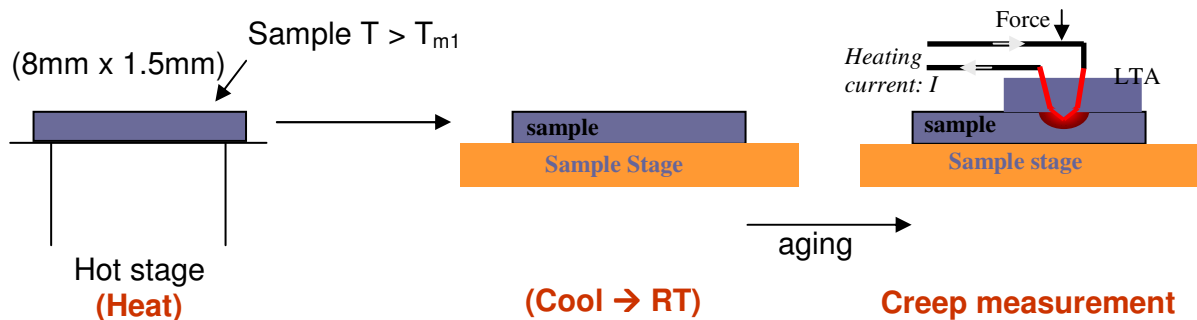


**Figure 6.3** Experimental procedure for creep measurement

Figure 6.4 (a) shows the creep curves measured at 30°C for various times of aging at room temperature and Figure 6.4 (b) shows the creep curves measured at 70°C for different times of aging at RT.

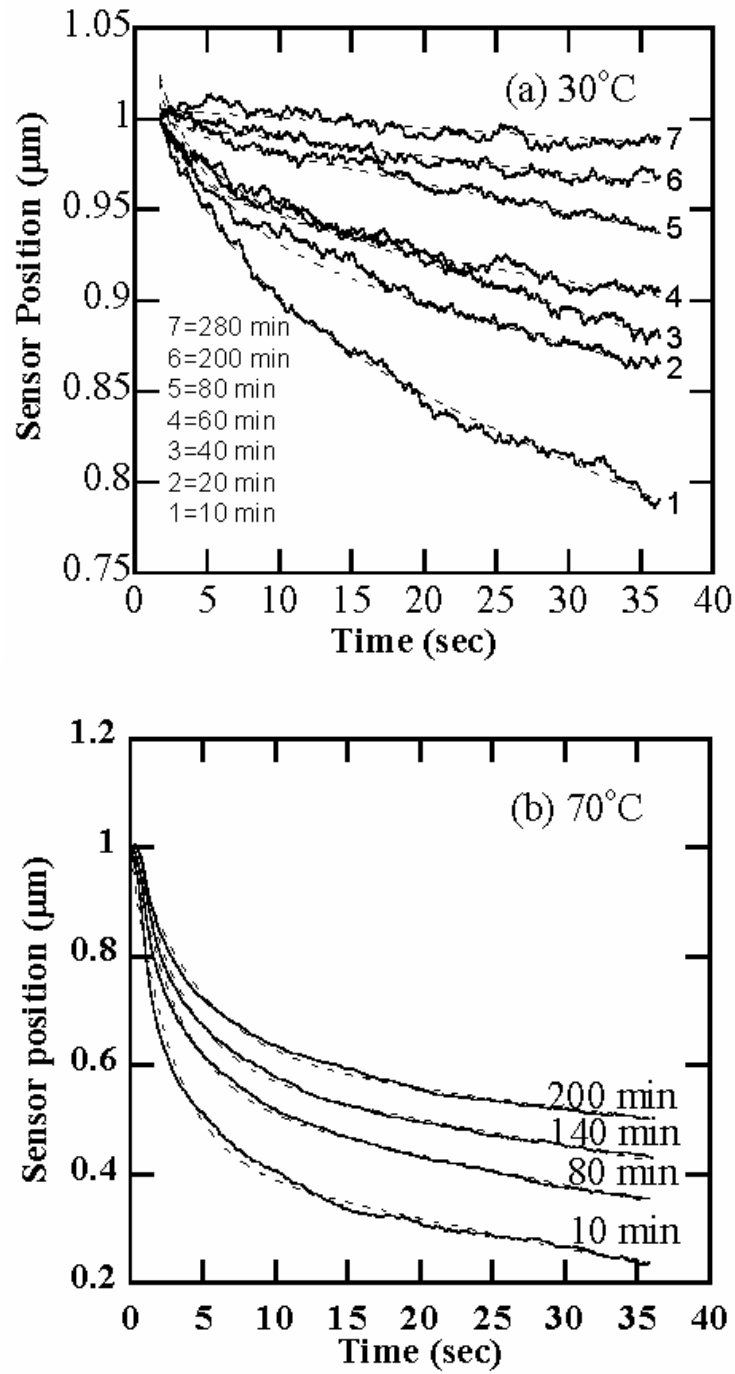


**Figure 6.4** Creep curves measured at (a)  $30^\circ\text{C}$  and at (b)  $70^\circ\text{C}$  after aging at room temperature for various aging (relaxation) times as indicated in the figure. The dashed lines are fits using the Burger model as described in the text.

#### 6.2.4 Burger Model: Modeling Creep in Surlyn:

Viscoelastic models are frequently used to explain creep in materials with complex structures such as ionomers and polymers. These models have viscous and elastic components which could be used in different combinations depending on the material under investigation. Components of the model can be assigned to different regions in the material based on the structures responsible for either viscoelastic or elastic response to an applied force. In this study using a viscoelastic model for the observed creep response of Surlyn could help us understand the dominance of different regions of the ionomer with aging.

In order to describe the data quantitatively, a Burger model is employed. The Burger model is one of the commonly used linear viscoelastic model for explaining glass transition and other physical properties of polymers<sup>2-4</sup>. As shown in Figure 6.5 (a) it consists of two components, a Maxwell part consisting of a dashpot (viscosity  $\eta_1$ ) in series with a spring (modulus  $E_1$ ) and a Voigt part consisting of a dashpot (viscosity  $\eta_2$ ) in parallel with a spring (modulus  $E_2$ ). The Maxwell and Voigt parts are connected in series. The strain induced due to an applied stress can be represented by  $\varepsilon_1$  across Maxwell spring,  $\varepsilon_2$  across the Maxwell dashpot and  $\varepsilon_3$  across the Voigt component. The total strain induced in the system is given by  $\varepsilon = \varepsilon_1 + \varepsilon_2 + \varepsilon_3$ . Here  $\varepsilon_1 = \sigma_0/E_1$ ,  $d\varepsilon_2/dt = \sigma_0/\eta_1$ ,  $d\varepsilon_3/dt + (E_2/\eta_1) \varepsilon_3 = \sigma_0/\eta_1$ . After eliminating  $\varepsilon_1$ ,  $\varepsilon_2$  and  $\varepsilon_3$ , we obtain the total strain in the system to be as shown in figure 6.5a;

$$\varepsilon = \sigma/E_1 + \sigma/E_2(1 - \exp(-t/\tau_2)) + (\sigma/\eta_1)t$$

The overall strain of this system as a function of time at a given stress  $\sigma$  is illustrated in Figure 6.5 (b) where the dominant contribution of each component in the Burger model is indicated. The negative sign represents the change in the probe position. Voigt viscoelasticity contributes to the creep curve an exponential decay with the measurement time whose depth

is determined by Voigt modulus. Maxwell viscoelasticity contributes to the creep curve a linear decay with the measurement time. Creep curves shown in Figure 4 are fit with the Burger model.

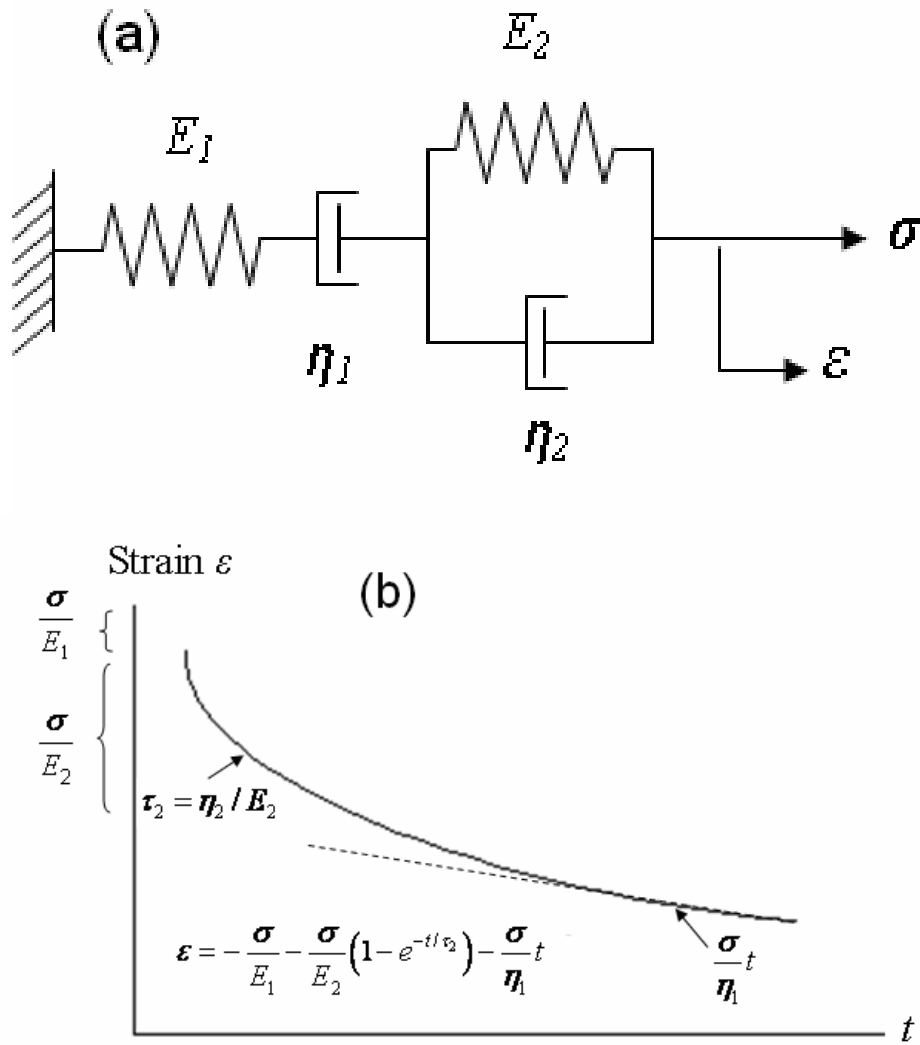


**Figure 6.5** (a) Burger model with the Maxwell and Voigt elements in series. (b) Characteristic solution of the Burger model for creep under constant stress.

In order to curve fit the data with the Burger model, a right combination of elastic and viscous parameters is required. In order to obtain these parameters, experiments are simulated by Finite Element approach.

This method allows construction of geometry of the sample with a point load application to simulate the applied force of the probe. The point load is applied across the same cross-sectional area as used for experiments. Intrinsic material properties such as room temperature modulus, coefficient of thermal expansion, and conductivity for Surlyn are used as input parameters before the simulation is started. A public domain finite element code 'Calculix' is used for simulation purpose<sup>5</sup>. The code has a simple visco-plastic constitutive model built-in, and has provisions for user-defined constitutive models. Since the source-code is available and well documented, it was just as easy to modify the built-in model to the Burger model.

An axial-symmetric simulation of the experiment with a point load applied on the viscoelastic body was constructed using the graphics preprocessor to the programme. Once the code was modified and the geometry constructed, a series of simulations were performed with different values for the elastic and viscous parameters to form a database of creep curves. These curves were fit using a multi-exponential curve. The experimental data was then fit using the same model function, and the parameters of the fits were used to find the most likely set of viscoelastic parameters to model the behavior. The extracted values for components of the burger model as a function of temperature and aging time are shown in the following section.

In Surlyn, ionic aggregates are the ion-rich regions and the amorphous part of the ionomer is ion-poor. Ionic aggregates are distributed in the ionomer matrix and help in cross-

linking. In the Burger model, Maxwell part represents the flow behavior which is closely related to the crosslink-deficient ion-poor regions. In contrast, the Voigt part describes the retarded elastic behavior which is closely related to the crosslink-abundant ion-rich regions. Which of these regions dominates the flow and mechanical properties of Surlyn is determined by the extracted values for the parameters.

### 6.3 Results & Discussion:

As shown in Figure 6.2 the  $T_{m2}$  peak at 55°C in the fully relaxed ionomer corresponds to the melting of secondary crystallites and possibly ordered structure around ionic aggregates. This peak disappears in the second and subsequent runs at aging times of 10 min, 20 min, 40 min, and 60 min. Visible intensity of this peak is observed as the secondary crystallites begin to form after a few hours of aging at RT. We need to know if there are other significant structural changes taking place at short aging times before the appearance of the  $T_{m2}$  peak.

The extracted values of Maxwell viscosity  $\eta_1$ , Voigt modulus  $E_2$ , and Voigt viscosity  $\eta_2$  based on the Burger model are shown in Figure 6.6 as a function of the time of aging at RT. As shown in Figure 6.6 (a), Maxwell viscosity  $\eta_1$  measured at 30°C exhibits a linear increase with the time of aging at RT, whereas it changes very little when measured at 70°C. Figure 6.6 (b) shows that Voigt modulus  $E_2$  shows a similar trend as Maxwell viscosity. In contrast to Maxwell viscosity and Voigt modulus, Voigt viscosity  $\eta_2$  measured at 70°C does depend significantly on the time of aging at RT as shown in Figure 6.6 (c). Voigt viscosity at 30°C was not shown because the dominance of Maxwell viscosity makes the determination of Voigt viscosity unreliable. Also, the Maxwell modulus  $E_1$  is not measurable in the experimental creep curve due to the instantaneous response of the associated strain ( $\sigma / E_1$ ) as indicated in Figure 6.5 (b). These quantitative estimates for the different components of the Burger model provide the basis for the understanding of structural relaxation at short aging time.

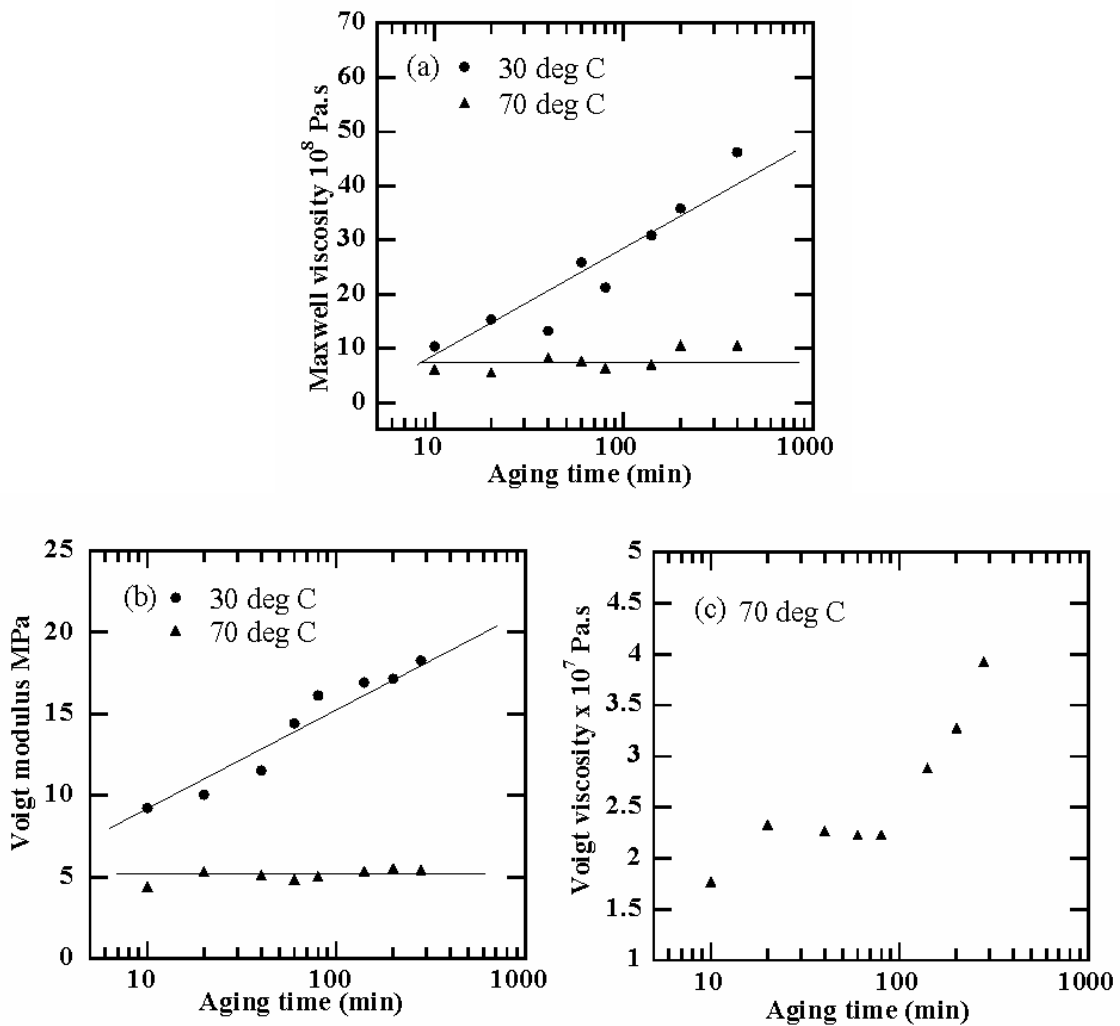


**Figure 6.6** Extracted values based on the Burger model fits of the creep curves. (a) Maxwell viscosity, (b) Voigt modulus, and (c) Voigt viscosity are shown as a function of the time of relaxation at room temperature. Values derived from both the 30°C and 70°C creep curves are shown.

Structural relaxation at RT depends on the conformation in the polymer chains around the ionic aggregates and how it changes as a function of aging time. It is well known that neutralized ionomers consist of ion-poor and ion-rich regions where the former possesses a glass transition temperature below  $RT^6$ . In contrast to ion-poor regions, structural relaxation could occur at RT in ion-rich regions. Restricted mobility region models have been used to explain structural relaxation around ion-rich region in both amorphous and semicrystalline ionomers<sup>6,7</sup>. One possible scenario is that the structural relaxation at RT could lead to denser packing of polymer chains, effectively increasing the size of the restricted mobility region around the ionic aggregate. The growth of the effective size of restricted mobility region could lead to more overlapped restricted mobility regions yielding higher number of percolation pathways of such overlapped regions throughout the sample. Subsequently, the viscoelastic properties are altered with aging at RT.

In semicrystalline ionomers, secondary crystallites could form at short aging times at RT, although not detectable by DSC. Previous reports have shown the formation of secondary crystallites at aging time of few hours at  $RT^6$ . It is possible that secondary crystallites could contribute to increased number of percolation pathways along with the overlapped regions of restricted mobility at short aging times at RT.

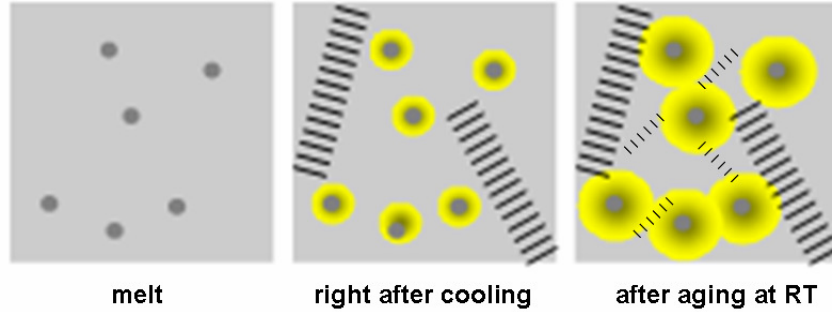


**Figure 6.7** Illustration of structural relaxation at RT after cooling from the melt. In the melt the ionic aggregates are present. Right after cooling from the melt, primary crystals are present and the region with restricted mobility around the ionic aggregate is small. The effective size of such restricted mobility region grows and small secondary crystallites form after aging at RT.

This scenario is illustrated in Figure 6.7. This model provides a qualitative understanding of the observed viscoelastic properties. In the Burger model, Maxwell part represents the flow behavior which is closely related to the crosslink-deficient ion-poor regions. In contrast, the Voigt part describes the retarded elastic behavior which is closely related to the crosslink-abundant ion-rich regions.

Our experiments demonstrate that both Maxwell and Voigt components measured at 30°C exhibit strong dependence on the aging time at RT (Figure 6.6) before the emergence of the  $T_{m2}$  peak in DSC (figure 6.2). This indicates that significant structural relaxations take place at RT after quenching from the melt in the ion-rich region and the possible formation of secondary crystallite structures not detected by DSC could contribute to percolation pathways.

Figure 6.6 also shows that the Maxwell viscosity and the Voigt modulus measured at 70°C exhibit no effect of aging at RT. This could possibly be explained by significant reduction in the effective size of the restricted mobility regions at 70°C. The reduction in size of the restricted mobility regions could eliminate those overlaps and percolation pathways

formed by RT aging so that Maxwell viscosity and Voigt modulus are largely determined by the ion-poor regions.

Unlike Maxwell viscosity and Voigt modulus, Voigt viscosity measured at 70°C (Figure 6.6 (c)) does show aging effect at RT. This shows that the RT structural relaxation in the restricted mobility regions is not completely erased thermally at 70°C with remnant effect on the retardation of the elastic property. In case the terminology of the glass transition is still appropriate for the current context, this means that the glass transition temperature of the restricted mobility regions is near or above 70°C.

## 6.4 Conclusion:

An AFM-based Local thermal analysis technique and a Burger model have been used to study the structure-property relation of Surlyn<sup>®</sup> at short aging times at room temperature after cooling from the melt. Previous studies have shown the presence of primary crystallites, secondary crystallites, ion-rich regions and the ion-poor regions in a fully relaxed ionomer. It is shown that structural relaxations of ion-rich regions contribute to the viscoelastic properties at short aging times, perhaps by contributing to the formation of percolation pathways of ion-rich regions. The current study demonstrates the ability of the LTA technique for observing the structural relaxation of ion-rich region at room temperature at short aging times. When measured at 30°C, Voigt modulus (closely associated with the crosslink-abundant ion-rich regions) and Maxwell viscosity (closely associated with the crosslink-deficient ion-poor regions) show strong effect of aging at RT after cooling from the melt. This suggests that the effective size of restricted mobility regions around ionic aggregates increases with aging at RT leading to more overlapped restricted mobility regions with increased number of percolation pathways. Secondary crystallites not detectable by DSC could form at short aging times and aid in increased number of percolation pathways. At 70°C, the overlapping regions of restricted mobility and the percolation pathways induced by RT aging break down as shown by the constant Voigt modulus and Maxwell viscosity values versus the time of aging at RT. However, Voigt viscosity measured at 70°C shows aging effect at RT. This shows that structural relaxations around the ionic aggregates are not completely erased thermally at 70°C with remnant effect on the elastic properties of the ionomer. Mechanical properties of Surlyn observed at long aging times in the presence of a fully relaxed structure are influenced by structural relaxation effects of the region around the ionic aggregates at short aging times.

## 6.5 References:

1. Loo, Y.L., Wakabayashi, K., Huang, Y.E., Register, R.A. & Hsiao, B.S. Thin crystal melting produces the low-temperature endotherm in ethylene/methacrylic acid ionomers. *Polymer* **46**, 5118-5124 (2005).
2. Gobet, F., Ciliberto, S. & Dauxois, T. Aging phenomena in nonlinear dissipative chains. *European Physical Journal B* **34**, 193-199 (2003).
3. Wang, H.C., Thompson, D.G., Schoonover, J.R., Aubuchon, S.R. & Palmer, R.A. DMA-FTIR creep-recovery study of a poly(ester urethane) elastomer with molecular-level viscoelastic modeling. *Macromolecules* **34**, 7084-7090 (2001).
4. Riande, E., Diaz-Calleja, R., Prolongo, M.G., Masegosa, R. & Salom, C. *Polymer Viscoelasticity: Stress and Strain in Practice*, (Marcel Dekker, New York, 2000).
5. Dhondt, G. *The Finite Element Method for Three Dimensional Mechanical Applications*, (Wiley, New York, 2004).
6. Wakabayashi, K. & Register, R.A. Morphological origin of the multistep relaxation behavior in semicrystalline ethylene/methacrylic acid ionomers. *Macromolecules* **39**, 1079-1086 (2006).
7. Eisenberg, A., Hird, B. & Moore, R.B. A New Multiplet-Cluster Model for the Morphology of Random Ionomers. *Macromolecules* **23**, 4098-4107 (1990).

## CHAPTER 7

### Surlyn-Titania Nanotube Composite: Synthesis, Characterization And Mechanical Properties

#### 7.1 Background & Motivation:

Inorganic and organic composite materials have been synthesized before to improve the mechanical properties of the parent organic matrix. Features such as conductivity, optical properties, and magnetic properties can be introduced in a variety of polymers by using inorganic materials as reinforcing structures<sup>1-3</sup>.

Ionomers in particular are interesting polymer materials due to their inherent properties which are useful for a variety of applications ranging from Golf ball coatings to packaging applications where the high-melt strength of ionomers is of importance in sealing of plastic films under heat and pressure. Flow and mechanical properties at high temperature play an important role for such applications. Also, there is an increasing use of ionomers in composite structures combined with glass, and carbon or aramide fibers serving sophisticated military applications. These applications also demand high temperature strength and faster recovery of mechanical properties.

In this chapter we will discuss Ionomer composites with titania nanotubes as the reinforcing structures, and how it could aid in faster recovery of mechanical properties.

Surlyn, a semicrystalline material in the presence of different components in the matrix is already by definition composite in nature. From the previous chapter, we have realized through careful understanding of the creep behavior of Surlyn, how different components in combination have an effect on the mechanical properties of the material. As concluded from the previous chapter, we also know that structurally relaxed Surlyn at long aging times after cooling from the melt has improved mechanical properties, and this depends on structural relaxation at short aging times. Structural relaxation at short aging time occurs due to subtle contributions from polymer chains with restricted mobility around the ionic aggregates. Presence of rigid reinforced structures could assist in structural relaxation at such short aging times in further improving the mechanical properties at that point and eventually in samples aged over long times.

Surlyn/titania and Surlyn/silicate based hybrid materials have been synthesized before by sol-gel reactions<sup>4,5</sup>. The methods used to synthesize these materials were novel in that nanoparticle structures used as reinforcements were synthesized in situ in the matrix of Surlyn. Although the mechanical properties improved to some extent, these were mere mechanically dispersed structures, and did not show any evidence of strong surface interactions between the nanoparticles and the polymer matrix. A reinforced structure that binds to the matrix through a strong inorganic/organic interface could improve the mechanical properties to a large extent.

This chapter introduces a unique approach to the synthesis of Surlyn/titania hybrid materials where the reinforced structures are titania nanotubes. Nanotubes have a large aspect

ratio as compared to nanoparticles and when dispersed anisotropically in the matrix of Surlyn could improve the mechanical properties in all the directions. Also, nanotubes have a reactive surface demonstrated by its ability to adsorb organic molecules in a short time of contact as mentioned in chapter 4. Reactive surface of titania nanotubes with long aspect ratio could be good candidates for composite structures of Surlyn.

In this chapter synthesis of the composite material shall be discussed, first followed by characterization, mechanical properties and its comparison with Surlyn.

## 7.2 Synthesis of Surlyn-Titania Composite:

Surlyn/inorganic hybrid materials have been synthesized before by sol-gel methods which involved unique in situ polymerization of alkoxide precursors to form oxide nanoparticles dispersed in the matrix of Surlyn. This approach used the swelling property of Surlyn in alcohols, which enhanced the permeability for diffusion of alkoxide precursors followed by polymerization resulting in mechanical dispersion of nanoparticles. Composites of both acid forms and neutralized forms of Surlyn were synthesized using this procedure<sup>5</sup>. Neutralized form of Surlyn took a longer time to swell in the solution due to the presence of stronger ionic associations, and was carried out at elevated temperatures. In this study we adopt a procedure which could not only produce a composite with stronger inorganic/organic interface but also solve the problems of processing rheology for neutralized form of Surlyn.

Instead of swelling Surlyn in the propanol solution, a procedure usually employed to synthesize the hybrid materials of Surlyn, we dissolve the polymer in an organic solvent. Dissolving the neutralized form of Surlyn in organic solvents has faced some challenge due to the strong ionic aggregates. Therefore, we dissolve the unneutralized acid precursor of Surlyn in the organic solvent and neutralize it later. The acid polymer has ethylene backbone chains, that form the primary crystallites, and methacrylic acid chains that form the ionic associations. Not all organic solvents can dissolve ionomers. A model process has successfully shown the ability of xylene:butanol, as a solvent mixture to recycle ionomer based materials<sup>6</sup>. This is significant because the solvent used for recycling has shown that it can dissolve and also reprecipitate the ionomer, a process required to preferentially separate the ionomer from application surfaces and other polymer mixtures. The ability of

xylene/butanol solvent 4:1 to dissolve/precipitate the ionomer is used for uniform dispersion of nanotubes, and precipitation of composite after synthesis.

Nanotubes used to make the composite were synthesized by the hydrothermal procedure as mentioned in chapter 2. These are a few hundreds of nanometer in length and 10-12 nm in diameter as shown in figure 7.1.

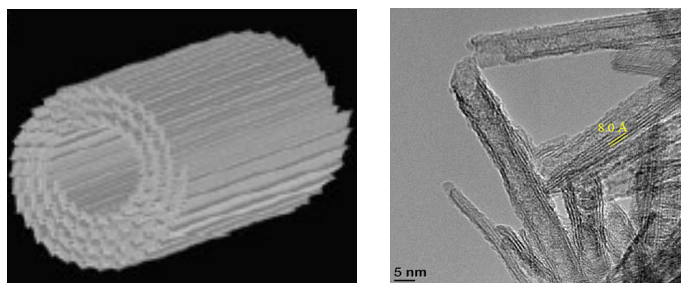


**Figure 7.1** Titania nanotubes synthesized by hydrothermal process  
(left) a model structure showing the scroll nature of the tube  
(right) TEM of nanotubes.

5 g of precursor acid pellets were dissolved in 100 mL of solvent mixture and stirred at 75°C for 90 minutes. The process is carried out in a teflon beaker. A homogeneous melt of the polymer acid is formed in the organic solution, and is called solution A. A separate solution containing 500 mg of acid pellets in 20 mL of xylene is heated at 75°C for 60 minutes, and this mixture is labeled as solution B. Note here that the solution used contains only xylene, as this solution is used for dissolution and not precipitation. 500 mg (10 wt %) of as synthesized titania nanotubes was sonicated in 20 mL of xylene to obtain well suspended nanotubes and poured in solution B. Solution B containing the nanotubes dispersed in acid polymer was added to Solution A. The resultant solution was then allowed to homogenize by stirring at 75°C for 30 minutes. It contains unneutralized acid polymer and titania nanotubes dispersed in the organic solvent. 60% of the unneutralized acid groups were reduced by Na ions after the addition of 5.74 mL of 1 M NaOH. This mixture was then kept open overnight at 75°C to

evaporate the solvents as the neutralization proceeds. As the solvent evaporates, the neutralized product begins to precipitate. The precipitate retains significant amount of solvent and is kept in the oven at 50°C for 4-5 hrs until the sample is dry. The composite thus obtained is opaque as shown in figure 7.2 a, due to the dispersion of nanotubes and air bubbles.

The above procedure is repeated for synthesis of neutralized form of Surlyn without the titania nanotubes, so that we could compare the mechanical properties of composite and the pure form. Surlyn without titania nanotubes as reinforced structures is shown in figure 7.2 b.



**Figure 7.2** a) Composite of Surlyn and titania nanotubes.  
b) Surlyn prepared from neutralization of acid polymer using same procedure as the composite without the titania nanotubes

### 7.3 Characterization:

Scanning Electron Microscopy (SEM) was performed to characterize the morphology of composite and Energy Dispersive X-ray analysis (EDAX) was used in combination to determine the distribution of titania nanotubes in the polymer matrix. The composite materials are poor conductors and to avoid any imaging issues they were sputter coated with conductive material such as silver. SEM was then performed on these sputter coated composites. Figure 7.3 a shows a fractured surface of the composite with the polymer fibers extending out of the surface. Figure 7.3 b shows tube like structures on one of the exposed fracture surface of the composite. The elemental composition of this region was determined by EDAX and figure 7.3 c shows the green spots as titanium atoms as distributed in figure 7.3 b. It is thus confirmed that titanium dioxide nanotubes are uniformly distributed in the polymer matrix.

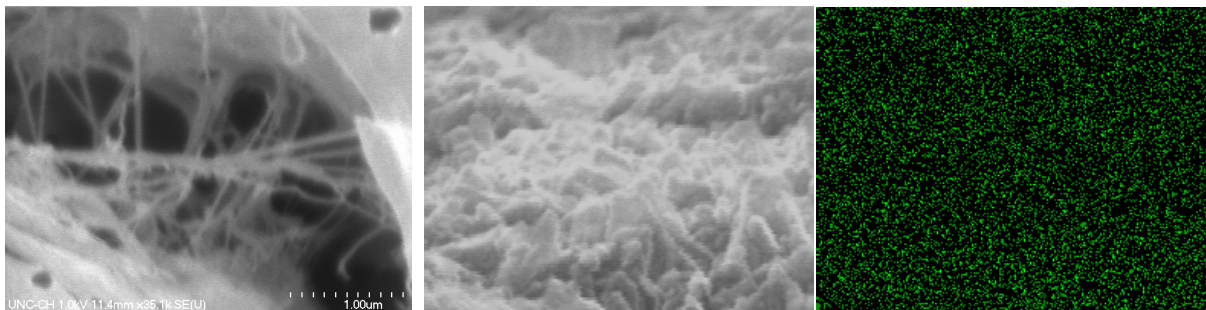


**Figure 7.3** a) A fractured surface of the composite as observed by SEM (scale bar 1 $\mu$ )  
b) Tube like structures observed on of the cross-sections coated with polymer c) EDAX  
analysis shows the presence of titanium atoms as distributed in (b).

## 7.4 Mechanical Properties:

### 7.4.1 Materials and Technique:

Mechanical properties of the composite were measured by the AFM based Local Thermal Analysis technique as mentioned in chapter 6. A micron size probe is used to measure the creep response of composite and Surlyn as a function of temperature and aging time following exactly the same procedure as mentioned in chapter 6.

Before the creep measurement, both composite and Surlyn samples were hot pressed at 90°C into sheets to remove the bubbles introduced during synthesis. Sheets were then stored at room temperature for several days before being used for creep measurement. Before the creep experiments were started, a hot stage was used to heat the samples to melt temperature and erase the thermal history of the samples. These were then cooled to room temperature and aged at different times. Creep response was then measured at these different aging times at two probe tip temperatures 30°C and 70°C. The significance of choosing these probe tip temperatures is explained in chapter 6.

The Burger model is used to determine the structure-property relation in the composite in a similar way as the ionomer in chapter 6. Differences observed in the mechanical properties could be a direct or indirect affect of the nanotubes.

Creep curves were obtained at 30°C and 70°C at relaxation times of 10 min, 20 min, 40 min, 60 min, 80 min, 140 min, 200 min and 280 min after the thermal reset. Burger model was used to curve fit the creep response and extract the viscoelastic parameters. It is recommended that the reader refer to chapter 6 for details of the curve fitting exercise and determination of the model parameters. Figure 7.4 shows the extracted values of Maxwell viscosity and Voigt modulus at 30°C and 70°C for composite and Surlyn.

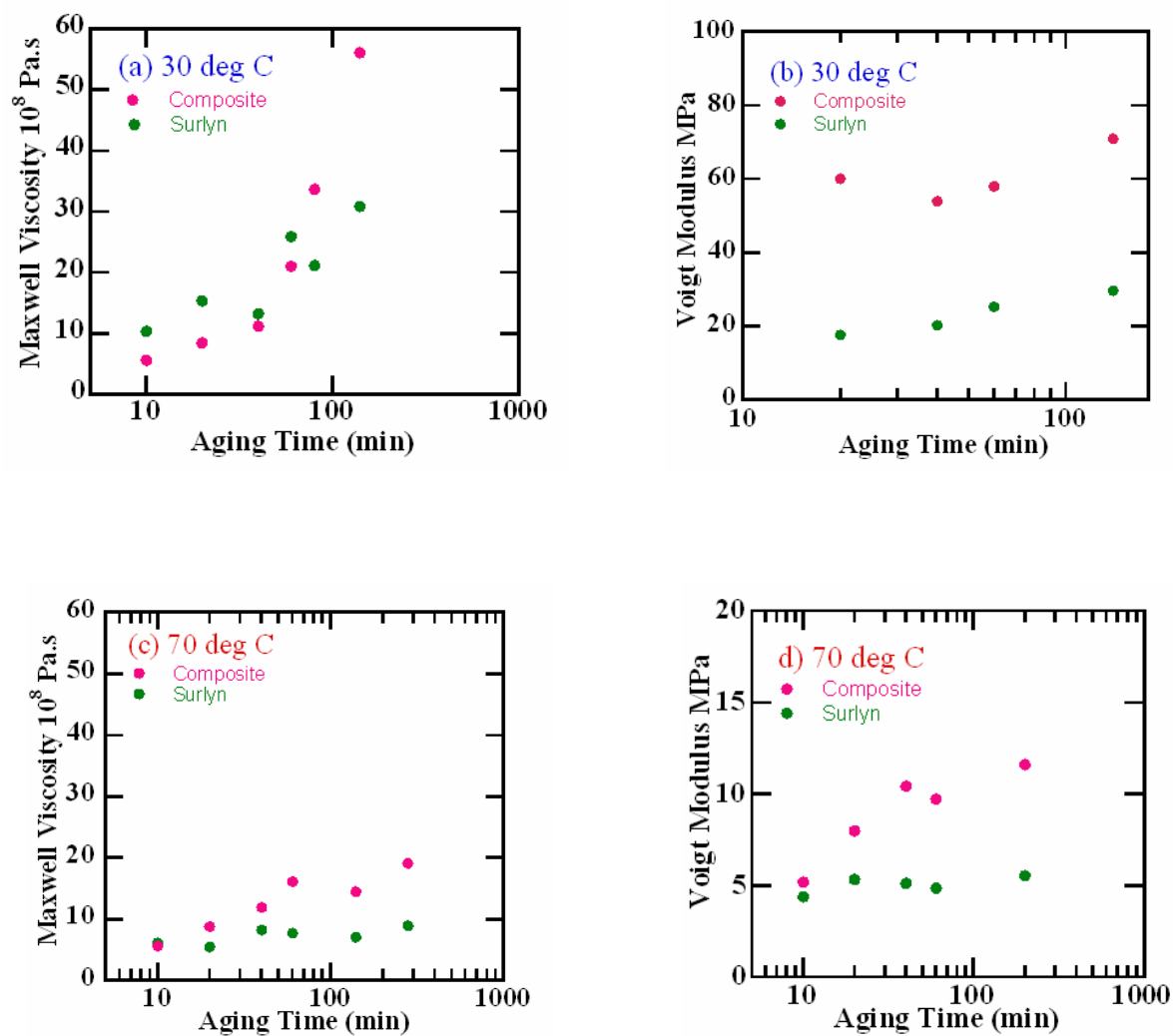


**Figure 7.4** Comparison of the Maxwell viscosity and Voigt modulus values for Surlyn and composite as a function of aging time at two temperatures 30°C and 70°C. Surlyn sample used in this study is prepared by neutralizing the precursor acid polymer.

#### 7.4.2 Results & Discussion:

Interesting differences are observed between the mechanical properties of Surlyn and the composite as shown in figure 7.4.

Figure 7.4 a shows the increase in Maxwell viscosity with aging at 30°C probe tip temperature for both composite and Surlyn, the later showing higher value at short aging time but dominated by former over long aging times. Figure 7.4 b shows that the presence of titania nanotubes improves the voigt viscosity by three times as compared to Surlyn. The aging effects on this property are however comparable. Both Maxwell viscosity and Voigt modulus for Surlyn do not show any aging effects at 70°C probe tip temperatures. Composite show better high temperature aging effects as compared to no effect in Surlyn as shown in figures 7.4 c & d.

As mentioned in chapter 6, the importance of regions of restricted mobility is clearly understood and we know how it helps in the structural relaxation of the ionomer by cross linking of the ordered structures such as ionic aggregates and crystallites. Here we can think of titania nanotubes also as an ordered structure which of course does not have any time dependent changes in its structure, but is a rigid template assisting the formation of ordered regions around its boundaries which could show aging effects. Regions of restricted mobility could also be present around the nanotubes and help in cross linking as the ionomer is cooled from the melt. These cross linked regions are represented by the Voigt component of the Burger model. Maxwell component of the Burger model characterizes the flow behavior of the polymer. Flow of the ionomer could be altered significantly if the movement of polymer chains is docked in the ionic aggregates or on the nanotube surface.

An interesting observation could be made from the change in the Maxwell viscosity at 30°C as shown in figure 7.4 a. It is apparent that Surlyn shows higher Maxwell viscosity at short time as compared to composite. Change in the flow properties of the ionomer with aging is dominated by the presence of ionic aggregates and is well proven by comparing ionomers with different neutralization levels. Presence of a reactive titania surface induces changes in the distribution of ionic aggregates.

- **Species of Ionic Aggregates: Aging Effects on Flow properties**

Ionic aggregates in the composite could be thought of as two types; type I which is similar to the pure Surlyn forming ionic aggregates with the order-disorder transition and type II which could form ordered structure around the nanotubes since nanotubes have surface hydroxyl groups with possible hydrogen binding sites for the free anion groups in the ionomer. Order-disorder transitions in ionic aggregates are dynamic in nature and bonds associate and dissociate with a bidirectional flux of free ions and associated ions. In composites due to the presence of nanotubes type I ionic aggregates take longer time to associate.

After cooling from the melt, nanotubes dispersed in the matrix are weakly associated with the type II aggregates, and type I aggregates take longer time to form in the composite as compared to Surlyn. Due to faster growth of the ionic association Surlyn shows a more viscous amorphous region as compared to the composite at short time as shown in figure 7.4 a. However with aging, type I ionic aggregates develop in the composite and more ordered structures (type II) are formed around the nanotubes shown by higher Maxwell viscosity values at long aging times. Both the presence of type I ionic aggregates and type II aggregates around nanotubes shows better properties at long aging times. At 70°C, which is the temperature higher than the DSC peak corresponding to the order-disorder transition of

the ionic aggregates type I, the Maxwell viscosity of Surlyn does not change with aging as shown in figure 7.4 c. The contribution from the type II ionic aggregates, the order structure around the nanotubes in the composite is clearly highlighted by the increase in Maxwell viscosity at 70°C.

- **“Regions of Restricted Mobility and Nanotubes”: Aging Effects on cross linking**

In chapter 6 the importance of “regions of restricted mobility” has been emphasized in cross linking of the ionic aggregates, the ordered structures in the ionomer and how this affects the overall mechanical properties of the ionomer. The Voigt component of the Burger model represents the cross-links in the ionomer. Figure 7.4 b shows the comparison of Voigt modulus of Surlyn and composite at 30°C as a function of aging time. It is interesting to note that the value for the composite is three times that of Surlyn. However, there does not exist a significant difference in the aging effect.

In Surlyn, regions of restricted mobility overlap and show the aging effects from the onset of this overlap. Titania nanotubes in composite could be thought of as structures which help in cross linking the regions of restricted mobility yet to overlap with each other. Titania nanotubes here do not show any time dependence because of its rigid structure, but the restricted mobility regions grow across the nanotube structure until they overlap and show the aging effect not much different from Surlyn as depicted by similar aging effects on Voigt modulus at 30°C (figure 7.4 b). In spite of the rigid structure of nanotubes, ordered structure around the nanotubes could possibly contribute to the overlapping and the aging effect. Similar trend in the aging effect on Voigt modulus for both Surlyn and composite however suggests that it does not take any part in this process.

At 70°C the overlapping regions of restricted mobility break down and Surlyn does not show any aging effects on the Voigt modulus. The composite would face a similar situation with no structural relaxation across the restricted mobility region; however the ordered structure around the nanotubes could generate restricted mobility zones around it and overlap with other similar regions. This could be responsible for the aging effects observed for Voigt modulus in composite (figure 7.4 d). These experiments show that although regions of restricted mobility important for structural relaxation through cross links and secondary crystallites cease to exist at 70°C, ordered structures can still form around titania nanotubes due to a strong inorganic/organic interface and assist in cross linking at elevated temperatures improving the mechanical properties for high temperature applications.

Tensile tests on structurally relaxed Surlyn and composite materials were compared and it was found that the Elastic Modulus for the composite (24 MPa) is 4 times improved over that of pure Surlyn (6 MPa). Theoretical values for the composite could not be extracted due to lack of enough information such as the molecular weight of the polymer, since it is proprietary information.

## 7.5 Conclusion:

Surlyn-titania nanotube composite, material with the ability for faster recovery of mechanical properties after cooling from the melt, as compared to pure Surlyn polymer, is synthesized for high temperature applications.

A micron sized probe with heating feature, has been used to compare creep response of the two materials to a constant applied force, at different aging times after cooling from the melt. Ordered structures, developing in Surlyn during cooling and after cooling from the melt, are known to be responsible for the recovery of mechanical properties at long aging times. Subtle structural changes, such as polymer chains with restricted mobility around the under-developed ordered structures, contribute to slow recovery of mechanical properties in Surlyn at short aging times after cooling from the melt. Titania nanotubes, used as reinforcing structures in Surlyn, catalyze the structural changes and therefore contribute to faster recovery of mechanical properties such as viscosity and modulus. Faster recovery of mechanical properties in Surlyn-titania nanotube composite, transforms to improved mechanical properties at long aging times, an important criterion for high temperature applications.

## Appendix I

### Quantitative estimation of Doxorubicin content in Nanotubes:

#### **Experimental Approach:**

Thermogravimetric measurements were carried out to determine the total doxorubicin content in the nanotubes.

For 2 mg of doxorubicin used for loading, the weight loss data shows that the total number of doxorubicin molecules adsorbed on 50 mg of nanotube surface =  $2.23 \times 10^{18}$  molecules

#### **Theoretical Approach:**

##### Surface Area of Nanotubes:

The total surface area of nanotubes after calculating the inside and outside surface area is  $187 \text{ m}^2/\text{g}$ .

For 50 mg of nanotubes used in this study,

$$\begin{aligned}\text{Total surface area} &= 187 \times 50 \times 10^{-3} \text{ m}^2 \\ &= 9.35 \text{ m}^2\end{aligned}$$

##### Surface Area of Doxorubicin:

Doxorubicin molecule has a total length of approximately 1.12 nm extending from the end of one benzene ring to the benzene ring at the other end and a width of 0.45 nm from the top of the chromophore to the glycosidic sugar group.

$$\begin{aligned}\text{Surface Area of one side of the molecule} &= 1.12 \times 0.45 \\ &= 0.504 \text{ nm}^2\end{aligned}$$

Considering a monolayer adsorption of doxorubicin molecule on the entire surface of the nanotube, we have the

The total number of doxorubicin molecules =  $9.35 / 0.504 \text{ nm}^2 = 18.55 \times 10^{18} = 16.63 \text{ mg}$ .

This value corresponds to 27 wt % of doxorubicin loaded in the nanotubes assuming a monolayer adsorption across the entire surface of the nanotube. Since only 2 mg of doxorubicin were used for loading, this suggests that more surface area is available for binding of more drug molecules for a monolayer adsorption process.

## 7.6 References:

1. Abeles, B. Optical-Properties of Films of Composite-Materials. *Journal of the Optical Society of America* 66, 163-163 (1976).
2. Larsen, D.C. Thermal-Conductivity of Boron-Epoxy, Graphite-Epoxy, Boron-Aluminum, and Borsic-Titanium Advanced Composite-Materials. *American Ceramic Society Bulletin* 53, 334-334 (1974).
3. Semko, L.S., Goncharyk, V.P., Revo, S.L. & Ivanenko, K.O. The study of the properties of the magnetic composite materials on the basis of thermoexfoliated graphite modified by ferrites. *European Magnetic Materials and Applications* 373-3, 761-764 (2001).
4. Siuzdak, D.A., Start, P.R. & Mauritz, K.A. Surlyn (R)/titanate hybrid materials via polymer in situ sol-gel chemistry. *Journal of Polymer Science Part B-Polymer Physics* 41, 11-22 (2003).
5. Siuzdak, D.A., Start, P.R. & Mauritz, K.A. Surlyn (R)/silicate hybrid materials. I. Polymer in situ sol-gel process and structure characterization. *Journal of Applied Polymer Science* 77, 2832-2844 (2000).
6. Poulakis, J.G. & Papaspyrides, C.D. A model process for the recycling of a Surlyn (R) ionomer. *Advances in Polymer Technology* 19, 203-209 (2000).